Mechanical Properties of High Density Polyethylene Sheets Exposed to Chlorinated Environment: Experimental Methods and Results

A THESIS
SUBMITTED TO THE FACULTY OF
UNIVERSITY OF MINNESOTA
BY

Evan Cosgriff

IN PARTIAL FULFILLMENT OF THE REQUIREMENTS
FOR THE DEGREE OF
MASTER OF SCIENCE

Susan Mantell, PhD
Mrinal Bhattacharya, PhD

August 2020

Acknowledgements

First, I'd like to thank my advisors Sue Mantell and Mrinal Bhattacharya for helping me at every step in my journey to completing this thesis. Without their support, I would not have known where to begin, let alone be able to find a place to conclude.

I'd also like to thank my fellow graduate students on this project Anu Tripathi and Kelly Majewski. Our discussions were instrumental in developing my understanding of the degradation processes which we were investigating. Anu's explanations of the parameters required to model the processes provided definition for what I would need to measure, and Kelly's detailed analysis of the underlying mechanisms clarified my understanding of the phenomena that were being measured.

Keddy Conocchioli deserves special praise, not only from me, but from our entire research group. Keddy assembled the initial waterbath apparatus from a collection of secondhand parts and proved that it could work. His contributions provided the basic equipment and methods for degrading specimens, which have been applied in the research for everyone who has followed him.

I would also like to thank all the undergraduate research assistants, including Amelia King, Danny Meyers, and Daniel Sellers, who helped to develop the methods required for producing the thin material specimens that we required. Their work included cleaning and updating lab spaces, repairing and upgrading industrial equipment, and tuning of the extrusion parameters to reliably produce our sheet materials. Without their efforts, we would not have had the thin specimens that allowed us to measure degradation in such a reasonable timeline.

I'd like to especially thank Al Khalil Al Riyami and Natalie Vig, undergraduate research assistants who performed tensile tests on *hundreds* of specimens to collect data for my project. Khalil worked tirelessly testing fracture specimens, which often left him working at unpredictable hours due to the long testing times required. Aside from performing many, many tensile tests, Natalie was also instrumental in developing the patterning methods which allowed us to collect DIC data.

Finally, I'd also like to thank Jörg Fischer. Jörg helped me to understand what changes in properties we should expect to find, what we should aim to measure, and what those measurements meant with respect to the underlying morphology of our materials. Jörg donated the fixturing for creating our notched fracture specimens and helped to develop our understanding of the essential work of fracture method when applied to those specimen's data. Jörg's work utilizing the waterbath apparatus in our lab also afforded us the opportunity to dial in its operation and increase its reliability.

Parts of this work were carried out in the Characterization Facility, University of Minnesota, which receives partial support from NSF through the MRSEC program. The author also gratefully acknowledge the support under grant CMMI-1462080 to the University of Minnesota from the U.S. National Science Foundation.

Dedication

To my wonderful and loving wife Virginia, whose unwavering support and encouragement have been instrumental in the pursuit of my graduate degree (and, really, whose patience deserves commendation for *all* my crazy endeavors).

Abstract

High density polyethylene is commonly used for plastic pipes because of its corrosion resistance and low cost compared with metals. In piping applications, disinfectants added to potable water supplies can lead to oxidation of the pipe materials. Longevity is critical; lifetimes in excess of 100 years are desirable. The interaction between stresses and environment, stress cracking, must be considered in predicting component lifetime.

Homopolymer HDPE was extruded from pellets into 70-100 micron thick sheet and heat treated to achieve two initial crystallinities. These samples were exposed for up to 1250 hours in a chlorinated water environment, at 5ppm @ 70 C with a pH of 6.5. The Oxidation Reduction Potential of the system was maintained at 825 mV. Changes in the morphology, specifically crystallinity and molecular weight, were evaluated as a function of exposure time. Crystallinity was evaluated through differential scanning calorimetry and molecular weight was evaluated through gel permeation chromatography. Similarly, changes in the mechanical performance, specifically tensile and fracture properties were also evaluated as a function of exposure time. Tensile properties were evaluated with ASTM 1708 dog-bone specimens at strain rates ranging between 0.1 and 0.002 sec^{-1}. Fracture properties were evaluated following the essential work of fracture method as applied to specimens at each exposure time.

The same trends in morphological and mechanical properties were observed regardless of the initial crystallinity. As-extruded sheets had an initial molecular weight of 230 kg/mol and crystallinities of either 75% or 83%. Molecular weight decreased to

less than 30% of the original after 1250 hours of exposure. The highest rate of decrease occurred between 250 and 750 hours exposure. At any exposure time, variation in molecular weight correlated with sample thickness, indicating correlation with a Fickian diffusion model. Crystallinities steadily increased with exposure time by approximately 13% over 1250 hours of exposure. Strain at break showed the most significant change of mechanical properties. Initial strain at break ranged between 4-10 mm/mm. Samples with higher initial crystallinities were completely embrittled after 750 hours, while those with lower initial crystallinities were embrittled after 1250 hours, both corresponding with approximately 90% crystallinity. The essential work of fracture required for the initiation and propagation of cracks during failure also indicated total embrittlement after 1000 hours exposure.

The combination of decrease in molecular weight, increase in crystallinity, and embrittlement with exposure provide insight into the mechanisms behind degradation and loss of mechanical performance. Given that the ductility of the material can be attributed to the amorphous region, the data support the hypothesis that chain scission occurs within the amorphous region and that these shortened chains may either migrate into crystalline regions or undergo chemicrystallization.

Table of Contents

List of Tables ..... **ix**

List of Figures ..... **xi**

Chapter 1: Introduction **1**

1.1 Background 1

1.2 Research Objective 2

Chapter 2: Literature Review **4**

2.1 Overview of HDPE 4

2.1.1 Structure of Semicrystalline Polymers 4

2.1.2 Mechanical Behavior of HDPE 8

2.1.3 Degradation and Embrittlement of HPDE 12

2.2 Studies of Polymer Degradation 15

2.3 Research Approach 19

Chapter 3: Materials and Equipment **21**

3.1 Preparation of Film Samples 21

3.2 Degradation of Samples 24

Chapter 4: Methods **31**

4.1 Tensile Characterization 31

4.1.1 Tensile Testing Method 32

4.1.2 Tensile Data Analysis 37

4.2 Fracture Characterization 47

4.2.1 Notch Testing Method 48

4.2.2 Notch Data Analysis 49

4.3 Morphological Characterization 57

4.3.1 Crystallinity Measurement 57

4.3.2 Molecular Weight Measurement 59

Chapter 5: Results and Discussion 61
5.1 Chemical Properties 61
5.2 Tensile Properties 68
5.3 Fracture Properties 76

Chapter 6: Conclusion 88
6.1 Summary of Methods 88
6.2 Findings and Observations 89
6.3 Recommendations and Future Work 92

Bibliography 97

Appendix A : Overview of Ncorr Algorithms 103
A.1 Ncorr Parameters 108
A.1.1 Subset Radius 108
A.1.2 Subset Spacing 110
A.1.3 Step Analysis 112
A.1.4 Strain Radius 113
A.2 Data Acquisition Considerations for DIC 115
A.2.1 DIC Pattern Considerations 117
A.2.2 Camera Setup Considerations 121

Appendix B : Tensile Test Breakpoint Data 125

Appendix C : Essential Work of Fracture Reports 129
C.1 Results for A Specimens 130
C.1.1 Unexposed A Specimens 131
C.1.2 500-hour A Specimens 133
C.1.3 750-hour A Specimens 135
C.1.4 1000-hour A Specimens 137
C.1.5 1250-hour A Specimens 139
C.2 Results for B Specimens 141

C.2.1 Unexposed B Specimens 142
C.2.2 500-hour B Specimens 144
C.2.3 750-hour B Specimens 146
C.2.4 1000-hour B Specimens 148
C.2.5 1250-hour B Specimens 150
C.3 Essential work of fracture surface regression comparison 152
C.3.1 Unexposed Results 153
C.3.2 250-hour Results 154
C.3.3 500-hour Results 155
C.3.4 750-hour Results 156
C.3.5 1000-hour Results 157

List of Tables

Table 2.1: Polymer nomenclature and shorthand 14

Table 2.2: Studies of polymer degradation 15

Table 3.1: Selected resin properties for ExxonMobil Paxon™ AD60-007 21

Table 3.2: Extrusion temperature setpoints 23

Table 3.3: Extrusion process parameters 23

Table 3.4: Material samples by starting crystallinity and hours of exposure 30

Table 4.1: Load frame parameters by test method 35

Table 4.2: Camera parameters by testing method 36

Table 5.1: Number of specimens, mean Mw, and Mw standard deviation for GPC tests 64

Table 5.2: Essential work of fracture regression results 77

Table 5.3: Regression results for essential work of fracture surface model 87

Table A.1: Subset spacing values and resulting computational requirements 111

Table A.2: DIC camera specifications for current study 122

Table A.3: DIC lens specifications for current study 123

Table C.1: Essential work of fracture testing conditions for all DENT specimens 129

Table C.2: Tensile test conditions and EWF stress criterion for A specimens 130

Table C.3: Essential work results for A specimens, by exposure time 130

Table C.4: Essential work of fracture data for unexposed A specimens 131

Table C.5: Essential work of fracture data for 500-hour A specimens 133

Table C.6: Essential work of fracture data for 750-hour A specimens 135

Table C.7: Essential work of fracture data for 1000-hour A specimens 137

Table C.8: Essential work of fracture data for 1250-hour A specimens 139

Table C.9: Tensile test conditions and EWF stress criterion for B specimens 141

Table C.10: Essential work results for B specimens, by exposure time 141

Table C.11: Essential work of fracture data for unexposed B specimens 142
Table C.12: Essential work of fracture data for 500-hour B specimens 144
Table C.13: Essential work of fracture data for 750-hour B specimens 146
Table C.14: Essential work of fracture data for 1000-hour B specimens 148
Table C.15: Essential work of fracture data for 1250-hour B specimens 150

List of Figures

Figure 1.1: Three stages of failure for polymers subjected to corrosive environments [1] 1

Figure 2.1: Molecular representation of polyethylene [2] 4

Figure 2.2: Variation in branching molecular structures of polymers [2] 5

Figure 2.3: Tetrahedral structure of the HDPE molecule's carbon backbone [2] 6

Figure 2.4: HDPE semicrystalline structure: (a) chain folding within lamellae, (b) spherulites [2]..... 7

Figure 2.5: Spherulite examples: (a) natural rubber, (b) polyethylene [2] 8

Figure 2.6: Characteristic engineering stress-strain plot for semicrystalline polymer [2].. 9

Figure 2.7: True stress-strain curves for polypropylene at constant strain rate and varied temperature [5]..... 10

Figure 2.8: Crystal structure reorientation [4] 11

Figure 2.9: Basic reactions in the initiation and propagation of HDPE oxidation [9]..... 13

Figure 3.1: Diagram of extrusion process..... 22

Figure 3.2: Material sample dimensions in mm..... 24

Figure 3.3: Concentration of chlorine species in solution as a function of pH [8,29]..... 25

Figure 3.4: General control scheme..... 26

Figure 3.5: Temperature control scheme 27

Figure 3.6: pH control scheme..... 28

Figure 3.7: Chlorine control scheme..... 29

Figure 4.1: ASTM D1708 microtensile specimen, dimensions in mm..... 32

Figure 4.2: Size comparison of ASTM specimens with (a) material sample, (b) ASTM D1708, (c) ASTM D638, and (d) ASTM D882, all dimensions in mm 33

Figure 4.3: Specimen preparation showing (a) die-cutting process, (b) inking method, and (c) final resulting specimen..... 34

Figure 4.4: Demonstration of load compensation as applied to specimen B0000-T2-02. 38

Figure 4.5: Toe compensation for specimen A0000-T4-02 with delayed strain due to take-up of specimen slack 39

Figure 4.6: Toe compensation for specimen B0000-T2-02 accounting for specimen pre-strain 39

Figure 4.7: Digital image correlation showing (a) applied speckle pattern, (b) resulting displacement field, and (c) resulting Eularian strain field 41

Figure 4.8: Method for calculating engineering strain from DIC results 42

Figure 4.9: DIC toe correction, specimen A0000-T2-01 42

Figure 4.10: Comparison between DIC and D1708 tensile data sets for four specimens 43

Figure 4.11: Comparison between DIC and D1708 tensile data to 60% strain 45

Figure 4.12: Property determination points for tensile test data 46

Figure 4.13: DENT specimen geometry, all dimensions in mm 47

Figure 4.14: DENT notch cutting jig 48

Figure 4.15: Load-displacement plots for A0000 DENT specimens 49

Figure 4.16: Compensated load-displacement plots for A0000 specimens 51

Figure 4.17: Example crazing zone for specimen A0000-F08-03 52

Figure 4.18: Example load curves and notch images for tests with and without yield-before-fracture conditions 53

Figure 4.19: Maximum stress versus ligament length for A0000 DENT specimens showing tensile yield strength comparison and standard mean ± 10% cutoff values 54

Figure 4.20: Maximum stress versus exposure time for all A samples demonstrating data cutoff at 60% mean maximum stress of undegraded samples 55

Figure 4.21: Linear regression for A0000 specimen data showing 95% confidence intervals for the regression and essential work results 57

Figure 4.22: Example DSC data for unexposed A specimens 58

Figure 4.23: Example GPC data and results for specimen A0000-16-G2 59

Figure 5.1: Mass percent crystallinity versus exposure time for A and B samples 61

Figure 5.2: Molecular weight distribution plots for A samples at each exposure level 62

Figure 5.3: Weight average molecular weight GPC results for all A and B Specimens .. 63

Figure 5.4: Weight average molecular weight for A specimens, shown versus exposure time and thickness-normalized time 66

Figure 5.5: Weight average molecular weight for B specimens, shown versus exposure time and thickness-normalized time 66

Figure 5.6: Number of mechanical tests performed with and without corresponding GPC data 67

Figure 5.7: Example tensile data for A and B specimens demonstrating (a) elastic, (b) yielding, and (c) strain-hardening regions of the stress-strain curve 68

Figure 5.8: Effect of increasing strain rate on tensile data for (a) A specimens and (b) B specimens 69

Figure 5.9: Typical engineering stress-strain response up to intial yielding of material for (a) unexposed A specimens and (b) unexposed B specimens..... 70

Figure 5.10: Comparison of yield strength versus strain rate at each exposure level for (a) A specimens and (b) B specimens 71

Figure 5.11: Specimen yield strength versus mass percent crystallinity 72

Figure 5.12: Break stress and strain point values for each exposure level and relation to unexposed stress-strain curve 74

Figure 5.13: Strain at break values versus exposure level for each tensile test method for (a) A specimens and (b) B specimens..... 75

Figure 5.14: Essential work of fracture regression lines for each exposure time 76

Figure 5.15: Total work of fracture versus exposure time for 8mm and 16mm ligament DENT A specimens 79

Figure 5.16: Total work of fracture versus molecular weight for 8mm and 16mm ligament DENT A specimens 80

Figure 5.17: Total work of fracture versus normalized time for 8mm and 16mm ligament DENT A specimens 82

Figure 5.18: Total work of fracture versus thickness normalized time with surface regression for (a) A specimens and (b) B specimens..... 85

Figure 5.19: Total work of fracture versus exposure time with surface regression for (a) A specimens and (b) B specimens 87

Figure A.1: Two DIC images from a tensile test showing (a) one subset from the reference image, and (b) two subsets from a current image 104

Figure A.2: Application of a simple cost function comparing the reference subset $\boldsymbol{f}$ to (a) the well matched current subset $\boldsymbol{ga}$ and (b) the poorly matched subset $\boldsymbol{gb}$. 105

Figure A.3: Schematic of the solution steps 106

Figure A.4: Example subsets with radii of (a) 10 pixels, (b) 20 pixels, and (c) 50 pixels 109

Figure A.5: Example subset positions for the specimen in (a) for spacing values of (b) 14 pixels, (c) 4 pixels, and (d) 2 pixels. 110

Figure A.6: Similarly sized strain regions for (a) an example specimen with radii settings of (b) 1, (c) 3, and (d) 5 114

Figure A.7: Example DIC parameter dependence on test setup 115

Figure A.8: Interdependence of DIC parameters 116

Figure A.9: Specimen inking tool 117

Figure A.10: Specimen images with ROI highlighted and histograms for intensities within ROI at 0% and 60% strain (engineering strain, by jaw separation)..... 119

Figure A.11: Example of a problematically directional speckle pattern 120

Figure A.12: DIC equipment layout 123

Figure B.1: Break points for A specimen tensile tests at 1E-1 sec^{-1} strain rate (method one) 125

Figure B.2: Break points for B specimen tensile tests at 1E-1 sec^{-1} strain rate (method one) 125

Figure B.3: Break points for A specimen tensile tests at 1E-2 sec^{-1} strain rate (method two) 126

Figure B.4: Break points for B specimen tensile tests at 1E-2 sec^{-1} strain rate (method two) 126

Figure B.5: Break points for A specimen tensile tests at 1E-3 sec^{-1} strain rate (method three) 127

Figure B.6: Break points for B specimen tensile tests at 1E-3 sec^{-1} strain rate (method three) 127

Figure B.7: Break points for A specimen tensile tests at 2E-4 sec^{-1} strain rate (method four)..... 128

Figure B.8: Break points for B specimen tensile tests at 2E-4 sec^{-1} strain rate (method four)..... 128

Figure C.1: Load-displacement curves for unexposed A specimens 131

Figure C.2: Maximum stress versus ligament length for unexposed A specimens 132

Figure C.3: Essential work of fracture regression results for unexposed A specimens.. 132

Figure C.4: Load-displacement curves for 500-hour A specimens 133

Figure C.5: Maximum stress versus ligament length for 500-hour A specimens..... 134

Figure C.6: Essential work of fracture regression results for 500-hour A specimens 134

Figure C.7: Load-displacement curves for 750-hour A specimens 135

Figure C.8: Maximum stress versus ligament length for 750-hour A specimens..... 136

Figure C.9: Essential work of fracture regression results for 750-hour A specimens 136

Figure C.10: Load-displacement curves for 1000-hour A specimens 137

Figure C.11: Maximum stress versus ligament length for 1000-hour A specimens..... 138

Figure C.12: Essential work of fracture regression results for 1000-hour A specimens 138

Figure C.13: Load-displacement curves for 1250-hour A specimens 139

Figure C.14: Maximum stress versus ligament length for 1250-hour A specimens..... 140

Figure C.15: Essential work of fracture regression results for 1250-hour A specimens 140

Figure C.16: Load-displacement curves for unexposed B specimens 142

Figure C.17: Maximum stress versus ligament length for unexposed B specimens 143

Figure C.18: Essential work of fracture regression results for unexposed B specimens 143

Figure C.19: Load-displacement curves for 500-hour B specimens..... 144

Figure C.20: Maximum stress versus ligament length for 500-hour B specimens..... 145

Figure C.21: Essential work of fracture regression results for 500-hour B specimens .. 145

Figure C.22: Load-displacement curves for 750-hour B specimens..... 146
Figure C.23: Maximum stress versus ligament length for 750-hour B specimens..... 147
Figure C.24: Essential work of fracture regression results for 750-hour B specimens .. 147
Figure C.25: Load-displacement curves for 1000-hour B specimens..... 148
Figure C.26: Maximum stress versus ligament length for 1000-hour B specimens..... 149
Figure C.27: Essential work of fracture regression results for 1000-hour B specimens 149
Figure C.28: Load-displacement curves for 1250-hour B specimens..... 150
Figure C.29: Maximum stress versus ligament length for 1250-hour B specimens..... 151
Figure C.30: Essential work of fracture regression results for 1250-hour B specimens 151
Figure C.31: Exposure time surface regression comparison for unexposed A specimens 153
Figure C.32: Exposure time surface regression comparison for unexposed B specimens 153
Figure C.33: Exposure time surface regression comparison for 250-hour A specimens 154
Figure C.34: Exposure time surface regression comparison for 250-hour B specimens 154
Figure C.35: Exposure time surface regression comparison for 500-hour A specimens 155
Figure C.36: Exposure time surface regression comparison for 500-hour B specimens 155
Figure C.37: Exposure time surface regression comparison for 750-hour A specimens 156
Figure C.38: Exposure time surface regression comparison for 750-hour B specimens 156
Figure C.39: Exposure time surface regression comparison for 1000-hour A specimens 157
Figure C.40: Exposure time surface regression comparison for 1000-hour B specimens 157

Chapter 1: Introduction

1.1 Background

Stress corrosion cracking (SCC) is a phenomenon in which cracks develop in materials subjected to corrosive environments. These cracks are of interest because they can lead to brittle failure of the materials when subjected to stress. Many applications of plastics expose the materials to corrosive environments and are at risk for SCC, including potable water distribution systems (where disinfectants can lead to polymer degradation), landfill geomembranes, and nuclear wastewater systems. As shown in Figure 1.1, three stages can be observed for SCC failures in polymers, distinguished by the predominant mechanisms and lifetime [1]. In the first stage, materials fail due to long-term ductile (creep) deformations. These failures are easily avoidable by ensuring that design stresses are well below material yield stress. Stage three failures occur when high rates of degradation lead to failure under very little load due to SCC and material embrittlement. In this stage, lifetime is determined by the aggressiveness of the corrosive environment.

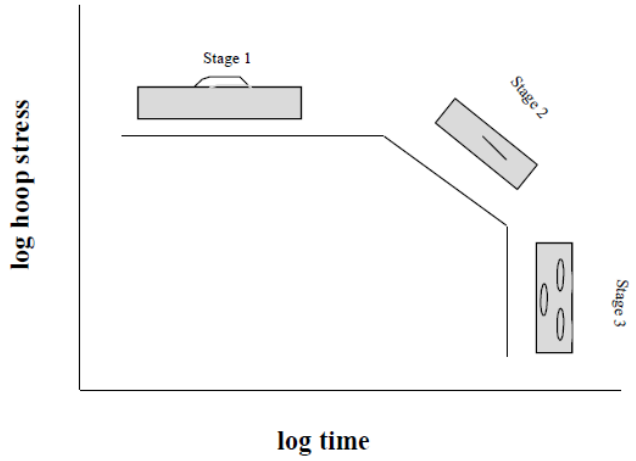

Figure 1.1: Three stages of failure for polymers subjected to corrosive environments [1]

Between these extremes, slow crack growth is predominant in stage two failures. In these cases, long-term crack development ultimately leads to brittle failure. As these cracks develop, more material is exposed to the corrosive environment; this hastens degradation at the crack tip, which in turn hastens the growth of the crack. To predict lifetimes for this stage, it is necessary to understand the mechanical properties of the material and how they degrade during exposure to the corrosive environment. Collection of this data is complicated by the timescales necessary to degrade specimens; plastic pipes are designed for many years of service without exhibiting signs of stage two or three failures.

1.2 Research Objective

Given the challenges of piping applications it is critical that we establish a relationship between degradation and mechanical performance. Equally important is developing the capability of predicting lifetime in harsh environments. The test data that are gathered in this work will provide the basis for numerical modeling of the complex mechanical behavior of polymers during stress corrosion cracking and thereby enable prediction of lifetime.

The specific objectives of this study are to collect morphological data representing the extent of degradation; collect mechanical data representing the progress towards embrittlement; and examine the relationships between the morphological and mechanical data. The material to be investigated will be homopolymer HDPE; this material is selected because it is a model system for exploring degradation mechanisms

and has similar properties to existing pipe materials. Degradation will be achieved through exposure to a chlorinated water environment which is representative of oxidative conditions existing for potable water.

Chapter 2: Literature Review

2.1 Overview of HDPE

Before describing the mechanical behavior and the chemical degradation of polyethylene, it will be helpful to review the basic chemistry and structure of the material. The following sections examine the structure of PE at the molecular and crystalline levels, the mechanical response of the semicrystalline material to loading, and finally the basic processes by which it degrades.

2.1.1 Structure of Semicrystalline Polymers

At the molecular level, polyethylene is a simple hydrocarbon chain. A backbone is formed by carbon atoms sharing single covalent bonds. Hydrogen atoms share the remaining side bonds, as represented in Figure 2.1. Other polymers share this backbone structure but with the side bonds occupied by atoms other than hydrogen or even by molecular groups. To distinguish between these variations, it is helpful to define polymers by the smallest repeating unit of their chain, or the mer, which is also highlighted for PE in Figure 2.1. The total length of these polymer molecules can become very long, with up to millions of repeated mer units [2].

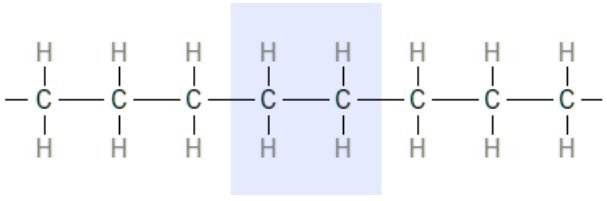

Figure 2.1: Molecular representation of polyethylene [2]

Materials like HDPE in which the carbon backbone forms a long single chain are linear polymers. This is shown schematically in Figure 2.2 (a), where each circle

represents one of the repeating mer units. If the side bonds of the carbon backbone are shared by other chains of carbon atoms, branched polymers or crosslinked polymers can also form as shown in Figure 2.2 (b) and (c) respectively. An example of a branched polymer is LDPE, which owes its lower density to the branches that prevent the molecules from packing as efficiently [2]. Crosslinked polyethylene, commonly referred to as PEX, gains rigidity and strength due to the crosslinks tying together the otherwise flexible chains [3].

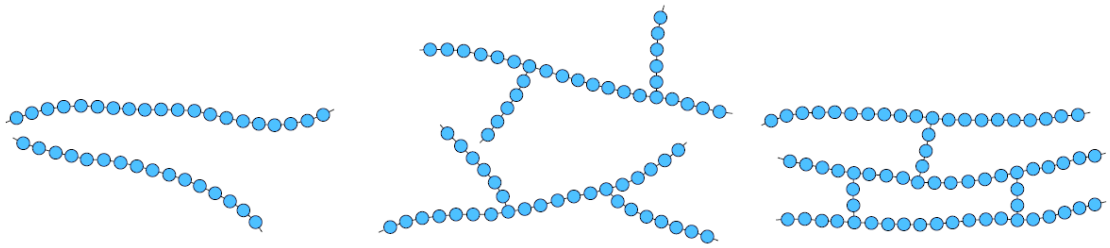

Figure 2.2: Variation in branching molecular structures of polymers [2]

The structures illustrated in Figure 2.1 and Figure 2.2 have been simplified and do not represent the three-dimensional structure of the molecules. In hydrocarbon molecules, the covalent bonds surrounding each carbon atom spread out to form a tetrahedron-like shape, as shown for the methane molecule in Figure 2.3 (a). The bonds in polymers follow the same structure, causing their carbon backbone to follow a zig-zagging pattern along its length. Figure 2.3 (c) illustrates this structure for a short length of linear polyethylene. The angle between each carbon bond in the chain is approximately 109°. The carbon atoms are not required to organize into a straight zig-zag; they may occupy any position which maintains 109° relative to the previous bond. As shown in Figure 2.3, this allows the molecule to twist and bend at any of the carbon bonds.

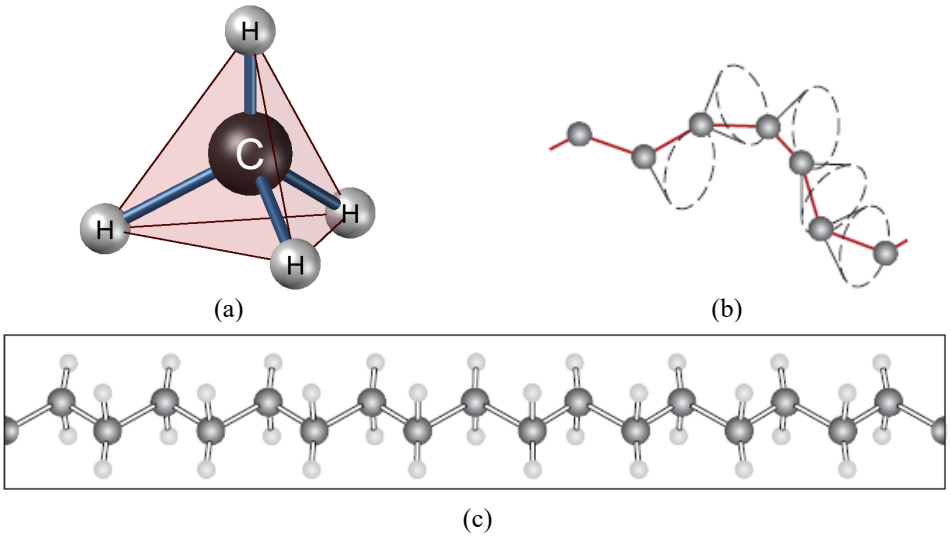

Figure 2.3: Tetrahedral structure of the HDPE molecule's carbon backbone [2]

In some polymers, such as polyethylene, these flexible molecules can organize into crystalline structures. These structures differ from the crystals found in other materials whose identical molecules can organize into very regular arrays. For polymer materials, this regularity can be difficult due to variations in chain length, complex mer structures, branching, and crosslinking. Polymers are semi-crystalline, containing both crystalline (ordered) and amorphous (disordered) regions. Crystalline regions generally develop as a polymer solidifies. A higher crystallinity will result from allowing the material to cool slowly, which gives the chains more time to organize into crystalline regions.

Polymer chains organize by folding back on themselves as shown in Figure 2.4 (a) to form thin ribbon-like structures which are called lamellae. These structures begin to form at nucleation sites as the polymer cools from a melt. As the lamellae grows outwards, branching occurs and causes the whole structure to become roughly spherical in shape. This structure, shown in Figure 2.4 (b), is known as a spherulite.

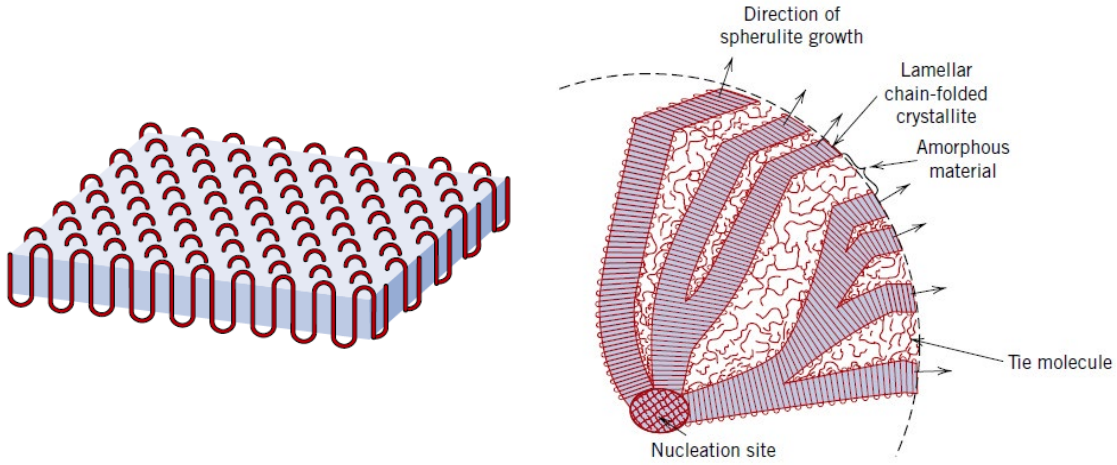

(a) (b)

Figure 2.4: HDPE semicrystalline structure: (a) chain folding within lamellae, (b) spherulites [2]

Figure 2.5 (a) shows a transmission electron micrograph of a spherulite in natural rubber where the lamellae and characteristic spherical shape can easily be seen. For this low crystallinity material, the large region surrounding the spherulite is amorphous material. If the degree of crystallization is high, as in the transmission photomicrograph of polyethylene shown in Figure 2.5 (b), the spherulites may abut against each other to form planar boundaries. In both cases, amorphous regions remain between the crystalline lamellae within the spherulite as shown in Figure 2.4 (b). Polymer chains within the lamellae may have ends which extend into this amorphous region, or which extend into and tie together neighboring lamellae.

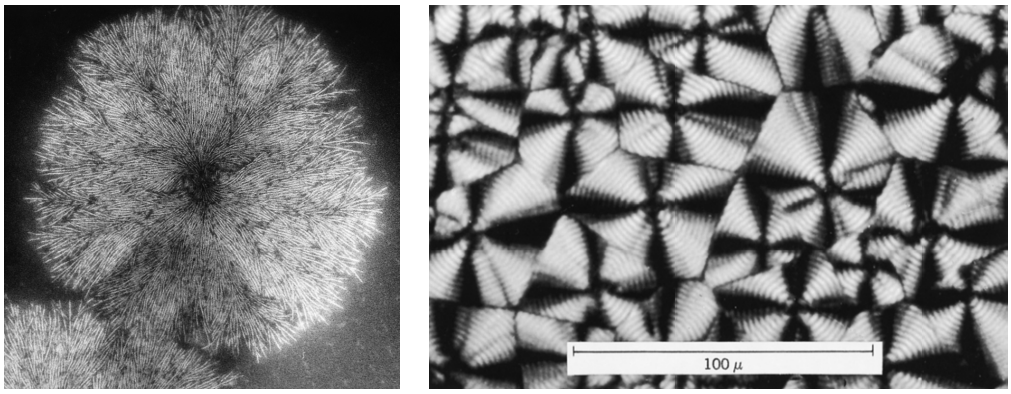

(a) **(b)**

Figure 2.5: Spherulite examples: (a) natural rubber, (b) polyethylene [2]

2.1.2 Mechanical Behavior of HDPE

To describe the mechanical behavior of semicrystalline polymers like polyethylene, it is helpful to examine the material's response at both a bulk and molecular level. In this section, the deformation and engineering stress-strain responses of a specimen to tensile loads are described. The relationship between bulk deformations and changes in the crystalline structure are then presented. Failure mechanisms in brittle semicrystalline polymers are also reviewed.

There are three primary stages to the loading curve of a semicrystalline polymer, as shown in the example engineering stress versus strain plot in Figure 2.6. As a specimen is first subjected to a displacement, the force required for that displacement will increase proportionately. The full gauge length of the specimen is stretched equally and under a uniform strain. The slope in this linear region is the modulus of elasticity for the material. There is no permanent deformation in this elastic stage; the specimen will return to its original configuration if the load is removed.

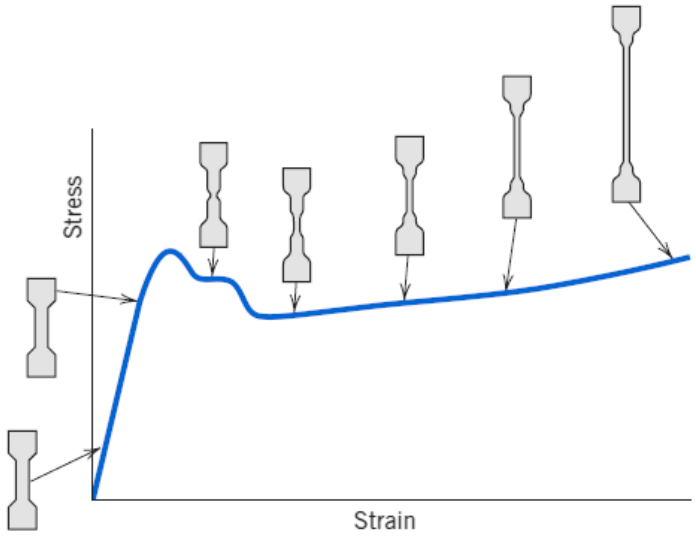

Figure 2.6: Characteristic engineering stress-strain plot for semicrystalline polymer [2]

The following stage is defined by localized yielding of the specimen. Following a maximum stress value reached at the end of the linear elastic region, a second "bump" is often seen in the stress response corresponding with the initiation of a necking region on the specimen. This is known as double-yielding, and the local maxima are referred to as the first and second yield points [4]. Deformations during this stage are permanent and are often accompanied by a decrease in the measured load. The material at the site of this necking is strengthened and has an increased resistance to further deformation. In the third stage of the loading curve, strain hardening, the necked region proceeds along the specimen as the applied displacement is increased.

The true stress and strain measured at specific points along the length of the specimen vary during testing. When the neck initially forms during yielding, the strain is high within that region while the stain along the rest of the sample remains low. During

the strain hardening portion of the test, neighboring areas transition to become part of the lengthening neck and a corresponding transition to high true strain values is observed.

The true stress and strain response (Figure 2.7) illustrates the mechanisms that occur within the polymer at the material level [5]. The elastic, yielding, and strain-hardening regions correspond with those previously defined for Figure 2.6. In the yielding zone, the stress is nearly constant over a large range of strain. Large deformation occurs locally after the onset of yielding and is the source of the necked region. Subsequently, there is a sharp stress increase in the strain-hardening region. When the necked region reaches this hardening strain, more energy is required to continue deformation. Other regions of the specimen which have not yet undergone necking, will still be at the flat yielding portion of the curve and will require less load to deform. Less energy is required for the necked region to expand, and it will continue to do so until the full gauge length reaches the strain hardening region.

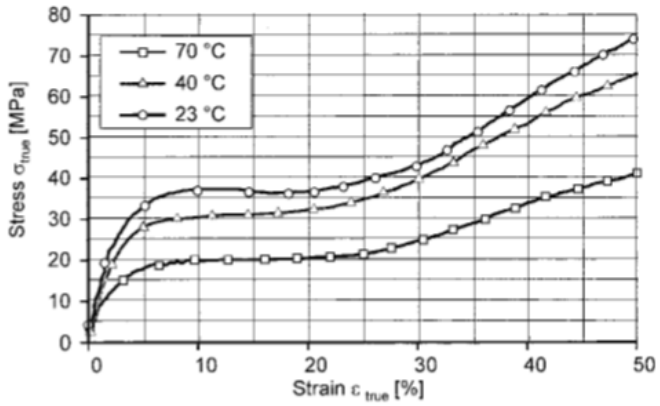

Figure 2.7: True stress-strain curves for polypropylene at constant strain rate and varied temperature [5]

The mechanisms by which polymers deform can be understood by examining changes in the crystalline structure as strain is applied to the material. Chains within

amorphous regions of the material have much more freedom to move as compared to the ordered crystalline regions. Within the spherulites, however, the crystalline lamellae limit the mobility of amorphous chains. In polymers like polyethylene where the spherulites compose most of the material, the interaction between these regions defines the material response to loading. Figure 2.8 demonstrates how the spherulites react under strain, with the regions corresponding to those from the true strain plot in Figure 2.7.

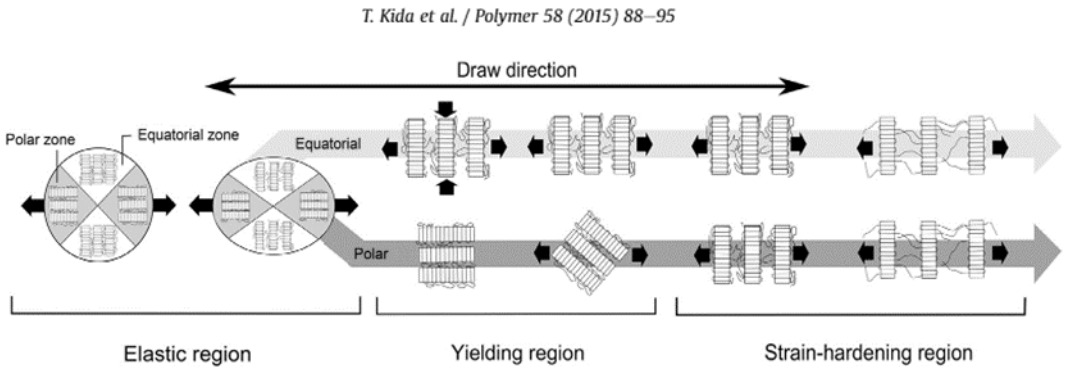

Figure 2.8: Crystal structure reorientation [4]

Within the elastic region, the spherulite elongates with deformation of the amorphous regions preferred but limited by the lamellae. The intra-lamellar regions constrict at the poles of the sphere (in the direction of loading) and stretch along the equatorial regions. The overall structure of the spherulite remains unchanged and can return to its original shape upon removal of the applied load [4,6,7].

When the material is stretched beyond the elastic region, yielding is experienced as the crystalline regions within the spherulite reorient. This change results in permanent deformation to the material. The chains of a polymer can best carry loads when the carbon backbone is aligned with the loading direction; much like a string, they are

strongest in tension. In the equatorial regions of the spherulite, the crystalline chains are aligned with the load and very little re-orientation is necessary. In the polar regions, however, the lamellae break into crystalline blocks which rotate to align the molecules with the loading direction.

After yielding has completed and the crystalline blocks are aligned, the material continues to deform in the strain-hardening stage. The chains in amorphous regions can move and stretch between the rigid crystalline blocks. The stretching of these amorphous change is the primary mechanism of deformation in this final stage [2,4].

2.1.3 Degradation and Embrittlement of HPDE

Polyethylene degrades by oxidation leading to breaks in the carbon chain (known as chain scission) and subsequent changes in the crystalline structure. Oxidation involves the introduction of oxygen into the hydrocarbon molecules and degradation of the polymer chain. Although many species can be produced through this process, only those which are related to the perpetuation of the oxidation reactions and to chain scissions are discussed here. The evolution of the crystalline structure due to these shorter chains is also explored, along with the expected response of the mechanical properties corresponding with these chemical changes.

A simplified representation of the relevant chemical reactions for polyethylene oxidation is represented in Figure 2.9. Table 2.1 summarizes the nomenclature and shorthand annotations for the reactive species. These reactions represent the initiation and propagation stages from the kinetic model presented by [8], with the remaining stages

and species omitted from this discussion for clarity. The process begins with the creation of an alkyl radical (P•) along the carbon chain, which can initially be accomplished through several mechanisms. In thermo-oxidation or photo-oxidation, the radical is formed after the absorption of heat or light energy, respectively. Free radicals introduced through diffusion into the polymer matrix can also act to abstract (remove) hydrogen atoms and form the alkyl radicals. In the present study, an oxidative environment was created by immersing polymer samples in a water bath that included dissolved sodium hypochlorite. In this environment, both Cl• and HO• radicals are present to form HCl and H_2O respectively. The remaining alkyl radical bonds with oxygen to form an alkyl peroxy radical (POO•). This radical then abstracts a further hydrogen to form a hydroperoxide group (POOH) along with a new alkyl radical (P•).

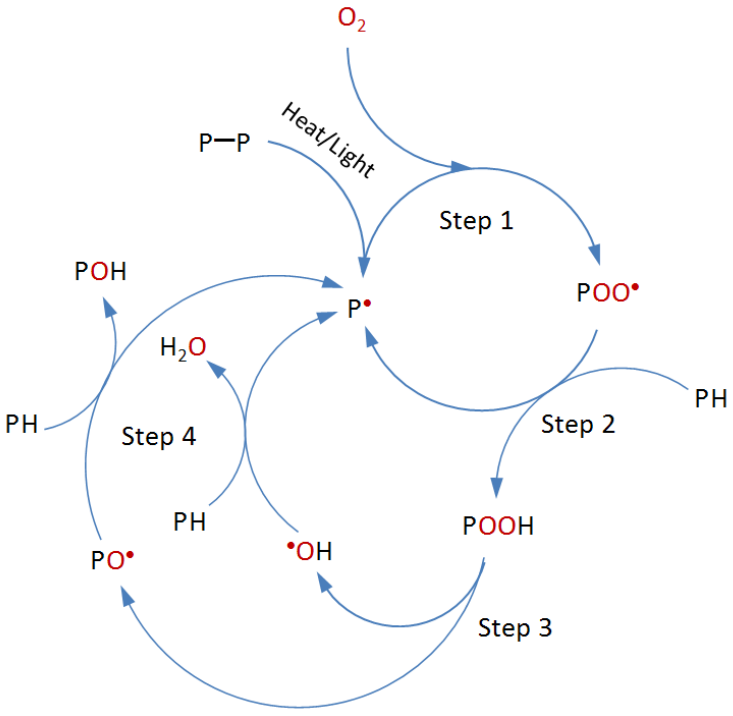

Figure 2.9: Basic reactions in the initiation and propagation of HDPE oxidation [9]

Table 2.1: Polymer nomenclature and shorthand

Chemical Name	Shorthand
Polymer chain	P
Alkyl radical	P•
Alkyl peroxy radical	POO•
Hydroperoxide group	POOH
Alcohol	POH
Carbonyl groups	P=O

The hydroperoxide group will then undergo degradation through several mechanisms, the notable products of which are also shown in Figure 2.9. Both P• and POO• radicals can be formed which can perpetuate the main oxidation cycle. Additionally, carbonyl groups can be produced by the hydroperoxide degradation. These groups are of significant interest because their formation can be accompanied by chain scissions. Note, there are additional species and reactions involved in the oxidation reactions of polyethylene. Although the concentration of these species and rates of all the reactions are important to the kinetics of the system, the portions presented here are sufficient to understand the processes that lead to the eventual degradation of mechanical properties.

Consideration of the above reactions highlights the importance of the availability of free radicals for initiation. The radicals, or a species which will decompose into the radicals, must diffuse into the polymer before the reactions can take place. Due to the high reactivity of the radicals and their relatively slow diffusion rates, oxidation will only occur at a thin surface layer. Mikdam et al. noted radical reactions occurred within about 50-100 μm of the surface [8]. Beyond this depth, the concentration of free radicals available to the bulk material is very low and very little oxidation will be initiated.

Antioxidants are also included in most commercial polymer blends to inhibit the oxidative degradation of the material. Antioxidants may be classified into two categories based on their primary mechanisms for blocking the oxidation cycle. Primary antioxidants react with free radicals to prevent their participation in the oxidation chain reactions. Secondary antioxidants function by decomposing hydroperoxide groups (ROOH) to into stable alcohol groups (ROH) and preventing the production of the free radicals shown in Figure 2.9 [10]. When observing the degradation of these commercial blends, initial oxidation rates will be slower until the antioxidant concentrations are depleted.

2.2 Studies of Polymer Degradation

Table 2.2 enumerates a representative selection of previous studies concerning the degradation of polymers. The material examined for each study is listed, along with a simple description of the physical format of the material samples; thicknesses are listed for studies with relatively thin specimens. Degradation methods are also listed along with environmental parameters for studies focusing on thermal and chlorinated water. Finally, testing methods employed to characterize the mechanical and morphological properties of specimens are listed for each study.

Table 2.2: Studies of polymer degradation

Author	Polymer	Environment	Mechanical	Morphology
Andrady (1993) [11]	LDPE films with pro-oxidants (30-420 μm)	Photo-thermal weathering (natural & accelerated)	Tensile	FTIR, Mw
Castillo Montes (2012) [12]	PE-RT pipes	Bleach (NaOCl) (0-100 ppm, 70 °C)	None	FTIR, OIT
Choi (2005) [13]	PB pipes	Photo (UV accelerated aging)	Tensile, fracture toughness	Mw, density

Colin (2009) [14,15]	PE pipes and films (100 μm)	Chlorine dioxide (ClO_2) (1-100 ppm, 20-40 °C, 2-6 pH)	Tensile (films only)	FTIR, OIT, Mw, s, x
Deveci (2018) [16]	HDPE pipes with AO & CB	None (focuses on CB effects)	Tensile	CB profiles, MFI, SEM, Density
Dongyuan (1987) [3]	HDPE sheet (3 mm)	Radiation crosslinking	Tensile	MFI, Xc, Gel Frac.
Fayolle (2008) [17]	Review: PE, PP, POM	Photo, thermal, hydrolysis	ultimate strain, draw ratio	Mw, Xc
Fayolle (2007) [18]	HDPE film (70 μm)	Thermal (Air, 80-90 °C)	Tensile	FTIR, Mw, Xc
Formela (2016) [19]	Crosslinked PE foam	Thermo-mechanical (processed in batch mixer)	Tensile (no embrittlement)	FTIR, DSC, Gel Frac, SEM
François-Heude (2015) [20]	Isotactic PP film (80-135 μm)	Photo, thermal	None	FTIR, Mw, Xc
Ge (2012) [21]	MDPE film (300 μm)	Bleach (NaOCl) (8 ppm, 80 °C, 6.8 pH)	Creep, EWF	FTIR
Gill (1998) [1]	PEX pipes	Chlorinated water (0-5 ppm, 90-120 °C, 8.0-8.4 pH)	None	OIT, SEM
Gulmine (2006) [22]	LDPE disks, no AO, varied crosslinking	Photo-thermal (accelerated aging)	Tensile, DMA	XRD, SEM, Gel Frac.
Hinsken (1991) [23]	HDPE and PP extrusions	Thermal, during extrusion (240-260 °C)	None	FTIR, MFI, Mw
Hsuan (1998) [10]	HDPE geomembrane (1.5 mm)	Thermal (landfill simulation)	Tensile	Mw, OIT, Xc, MFI
Langlois (1993) [24]	Crosslinked PE film (200 μm)	Thermal aging (110-170 °C)	Tensile	FTIR, Mc, Xc, Gel Frac.
Matsumoto (1983) [25]	LDPE films (155-750 μm)	Thermal (70-150 °C)	None	AO Conc., OIT
Mikdam (2017) [8]	PE film (150-350 μm)	Bleach (NaOCl) (100 ppm, 60 °C, 4-7 pH)	None	FTIR, Mw
Mitroka (2013) [26]	HDPE pipe and film (580 μm)	Bleach (NaOCl) (50-500 ppm, 37 °C, 6.5 pH)	None	FTIR, OIT
Yu (2012) [27]	MDPE plaques & film (500 μm), squalane	Chlorinated water (Cl_2, ClO_2) (10 ppm, 30-70 °C, 6.8 pH)	None	FTIR, OIT
Yu (2011) [28]	PE pipe, squalane	Chlorinated water (Cl_2, ClO_2) (4.0 ppm, 90 °C, 6.8 pH)	None	FTIR, Mw, OIT, Xc, SEM

* See nomenclature for acronyms

The studies included in Table 2.2 focus on the degradation of PE and other semicrystalline polymers such as PP. The mechanics of degradation for these materials follow similar processes, including oxidation reactions, chain scissions, and the ability for chains to migrate into crystalline regions. The primary methods employed to degrade specimens were photo-degradation, thermal degradation, and exposure to chlorinated water. A wide range of parameters were used for chlorinated water environments in the studies; free chlorine values ranged from 0-100 ppm, temperatures from 20-120 °C, and ph from 4-8. Sources of chlorine for the studies included chlorine gas (Cl_2), chlorine dioxide (ClO_2), and bleach (NaOCl or $Ca(ClO)_2$). While some studies measured and corrected chlorine concentrations rates up to once per second [21], other studies allowed the chlorine concentration to decay naturally [1]. Ultimately, the rates at which polymers degraded were dependent on the specific parameters of the study.

All the degradation studies listed in Table 2.2 included morphological measurements, but few measured mechanical properties. The use of FTIR measurements is prevalent and allows the examination of functional groups created during the oxidation reactions such as carbonyl groups. Other common morphological measurements included molecular weight (distribution, number average, or weight average), percent crystallinity, and oxidation-induction time (OIT). About half of the studies included mechanical testing of specimens. Mechanical properties were nearly exclusively determined from constant strain-rate tensile tests. Ultimate strain values are most commonly reported for these tests; these values decrease as specimens degrade and have been used as an indicator of embrittlement [3,10,11,14,16,18,19,21,22]. Studies with further mechanical properties included Gulmine, which used dynamic mechanical testing to determine viscoelastic

properties [22], and Ge, which used single-edged-notch specimens to examine creep and determine essential work of fracture values [21]. Choi also examined fracture properties using fracture toughness values calculated from standard tensile tests [13]. Overall, changes in morphology have been well established for polymer degradation while tensile property data are more limited and fracture properties are sparse.

Mechanical and morphological properties for the studies in Table 2.2 have generally been reported against exposure time to examine changes as degradation proceeds. A flaw with this method, as previously discussed, is that exposure times are not consistent between studies unless exposure methods and environmental parameters match. Langlois suggested that FTIR measurements (e.g. the carbonyl products from chain scission events) may be a useful predictor for changes in mechanical properties [24]. Fayolle later provided justification for the use of molecular weight as a parameter to characterize degradation processes governed by chain scission; in this study, specimen draw ratio was related to molecular weight [17]. As an indicator of embrittlement, strain at break values have been related to both carbonyl index [11,21] and molecular weight [11,18]. Relationships between failure energy and degradation parameters were explored by both Choi, who examined tensile test fracture toughness with respect to a parameter derived from number average molecular weight [13], and Ge, who examined the total work of fracture for notched specimens with respect to carbonyl index [21].

There are few studies which attempt to predict the mechanical properties of degraded polymer samples based on morphological measurements [11,13,17,18,21]. Of these studies, only Ge contains materials and degradation methods relevant to the

application of polyethylene pipes exposed to chlorinated water, but this study is lacking data for molecular weight and the essential work of fracture [21].

2.3 Research Approach

In order to predict the behavior of polymers as they degrade, it is necessary to measure changes in the mechanical properties in relation to changes in the underlying morphology of the material. In this study, polyethylene samples will be degraded in a chlorinated water environment and the relationships between morphological and mechanical properties will be explored.

Polyethylene material and chlorine exposure have been selected to mirror the use of polymer pipes in transporting chlorine-sanitized water supplies, in order to induce similar degradation mechanisms in the samples. Thin film samples will be prepared for exposure to expedite the aging process, which will continue until embrittlement of the material. Samples will be examined at a series of exposure times in order to measure the progression of both morphological and mechanical properties.

Morphological and mechanical properties will be examined which are indicators of the degradation process. Molecular weight distributions, which reflect chain scission events, will be measured by gel permeation chromatography (GPC). Crystallinity will be examined by differential scanning calorimetry to characterize the extent that shortened polymer chains (produced by the chain scissions) undergo chemi-crystallization. Degraded samples will be subject to a series of mechanical tests including constant strain rate tensile tests and double-edged notch tensile (DENT) tests. The strain-rate dependence of the material will be examined by performing standard tensile tests at a

variety of strain rates; this will provide data to calculate many mechanical properties including elastic modulus, yield stress, and strain-at-break. For DENT tests, notch depths will be varied to produce samples with varying ligament lengths. Data from this testing will allow the application of the essential work of fracture method to determine fracture characteristics of the material.

Finally, the relationships between mechanical and morphological properties will be examined. Mechanical indicators of degradation, such as strain-at-break and the essential work of fracture will be examined in terms of morphological indicators such as the molecular weight. The relationship between these values is not dependent on exposure times which vary for each application and experiment and will allow the characterization of material degradation (which may take years in field applications) through short-term laboratory experiments.

Chapter 3: Materials and Equipment

3.1 Preparation of Film Samples

To characterize the chemical and mechanical properties of HDPE at various states of degradation, thin material samples were required. These thin samples were extruded from a commercial grade PE. This film was cut to produce rectangular samples, sized to allow for mechanical testing geometries. The samples were then separated into two groups to examine the effects of crystallinity. Samples from the first group were degraded and tested directly, while the second group was heat treated prior to degradation and testing.

The HDPE resin selected for the current study was Paxon™ AD60-007 from ExxonMobil which is marketed for thermoforming and food packaging applications. Table 3.1 lists resin properties advertised by ExxonMobil along with measured values for Molecular Weight. These measured values were determined using GPC analysis, as discussed further in section 4.3.2.

Table 3.1: Selected resin properties for ExxonMobil Paxon™ AD60-007

Property	Value	Test Method
Density	0.963 g/cm³	ASTM D4883
Melt Flow Index	0.73 g/10 min	ASTM D1238 (190°C, 2.16kg)
Molecular Weight (Mw)	230 kg/mol	GPC
Polydispersity Index (Mw/Mn)	6.3	GPC

The HDPE pellets were then extruded into a film using a C.W. Brabender (CWB) type 3023 single screw extruder and Cloren 254 mm (10 in) Masterflex 2050 coat hanger die as illustrated in Figure 3.1. The screw had a diameter of 19 mm (0.75 in), a length to diameter ratio of 30:1, and a compression ratio of 3:1. Power was supplied to the screw

via a CWB D-3002 Prep-Center drive unit and temperatures were controlled by a CWB type 2003 Temperature Control Center (TCC). Extruded film was collected by a CWB Univex take-off unit (type 05-92-0000 SE) with rollers cooled by circulating water from a Neslab RTE-220 chiller.

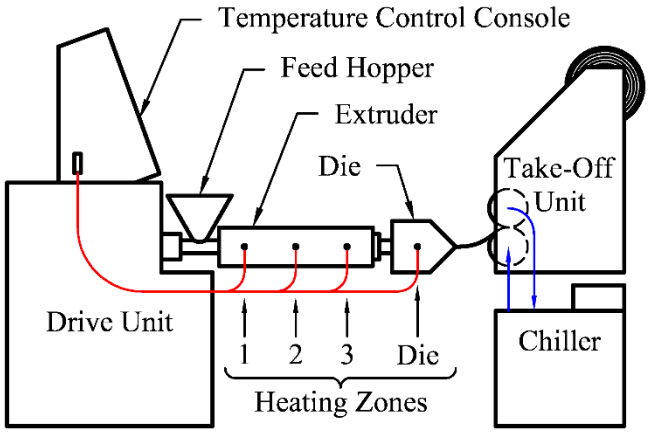

Figure 3.1: Diagram of extrusion process

The three heating zones for the extruder were controlled with the existing TCC, and a fourth PID controller was added to the TCC panel to enable heating of the die. The temperature setpoints ranged from 190 °C in zone one to 215 °C at the die, and the chiller roll temperature was 50 °C (see Table 3.2). No zone-specific cooling was applied; some external airflow was present, however, due to an exhaust fan placed over the extruder used to remove fumes from the room. Water temperature for cooling the take-off rollers was set directly on the chiller unit. The chiller unit was mounted on the mobile base of the take-off unit to prevent strain on coolant hoses during any movement of the equipment.

Table 3.2: Extrusion temperature setpoints

	Screw			Die	Chiller
Zone Number	1	2	3	4	-
Temperature	190 °C	195 °C	205 °C	215 °C	50 °C

The quality and consistency of film produced by the extrusion process depends on the speed of the screw, the lip gap set on the coat hanger die, and the speed of the take-off unit. Table 3.3 lists the final settings for each of these parameters to produce material samples in this study. The extrusion and take-off speeds were set with the Prep-Center and take-off units respectively, while the die gap was adjusted to 1.0 mm prior to extrusion with the aid of feeler gauges. The 3023 extruder also includes a vent port which was opened during processing to prevent air bubbles from being trapped in the film.

Table 3.3: Extrusion process parameters

Die Gap	Screw Speed	Film Stand Speed
1.0 mm	80 RPM	60 RPM

After extrusion, 100 x 30 mm rectangular samples were cut from the film roll (Figure 3.2). These dimensions were selected to allow for samples to later be cut into either individual notched specimens or multiple dogbone specimens for mechanical property testing as described in Chapter 4:. Each material sample was cut so that the longer dimension was aligned with the extrusion direction. The small size of the rectangular samples also helped to increase the number of samples which could be placed into the waterbath for degradation.

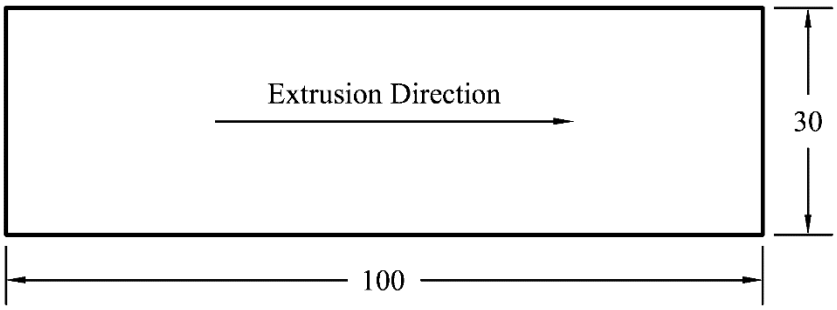

Figure 3.2: Material sample dimensions in mm

Finally, a series of these cut samples were subjected to a controlled heating cycle before being placed into the waterbath. Samples were placed into an oven at 120 °C for 60 minutes followed by disabling the oven and allowing it to cool, closed, overnight. By holding the material at an elevated temperature and then cooling it very slowly, the polymer chains are allowed more mobility and can reorder into a more crystalline arrangement. The series of untreated samples have been designated as “A samples” and are denoted with an “A” throughout the experiment. Similarly, the treated samples have been designated “B samples” and will be denoted with a “B.” After the heat treatment of series B, all samples were then ready to be placed into the waterbath for degradation.

3.2 Degradation of Samples

After extrusion, sizing, and heat treatment, material samples degraded in a bath apparatus containing a chlorinated water solution. The apparatus to control the oxidative environment meets two critical requirements. First, a control system is implemented to maintain the operational parameters within the system including the concentration of free chlorine, the pH, and the temperature. Second, the apparatus is designed to contain the oxidative fluid without (the apparatus) degrading over time.

The oxidative fluid is a solution of RO water and chlorine. The chlorinated environment was created by adding a concentrated sodium hypochlorite (NaClO) solution to a bath of reverse osmosis (RO) water. This form of chlorine is a light-yellow liquid and is commonly known as household liquid bleach. It was selected due to its relative ease of use and safety as compared to the other principle methods of chlorination: poisonous chlorine gas or calcium hypochlorite ($Ca(ClO)_2$). Calcium hypochlorite, or powdered bleach, has greater availability of chlorine, but it is difficult to dissolve into water and requires ventilation equipment which is not required for sodium hypochlorite. Once in solution, three species of chlorine may exist: hypochlorite ions (OCl^-), hypochlorous acid (HOCl), or molecular chlorine (Cl_2). The concentrations of these species are dependent on the pH of the solution as shown in Figure 3.3.

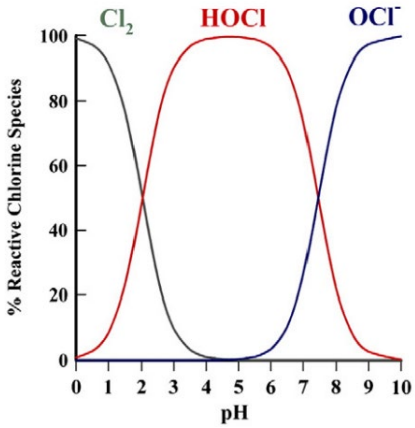

Figure 3.3: Concentration of chlorine species in solution as a function of pH [8,29]

Due to this dependence, the pH of the waterbath must be controlled to maintain a consistent concentration of the chlorine species. A high concentration of HOCl is desired, as it is the most reactive of the three species and is the most likely to degrade material specimens. The species equilibrium is temperature dependent as well; a constant

temperature must be maintained for consistent concentration levels, and elevated temperatures are desired to encourage an increased rate of oxidative reactions.

The oxidative characteristics of the water bath are quantified by the oxidation reduction potential (ORP), where a typical ORP for household water ranges from 300-400 mV. An ORP of 825 mV is considered a highly oxidative environment and can be achieved by controlling the water temperature to 60-65°C, free chlorine to 5.2 +/- 0.5 ppm, and pH to 6.3 +0.5/-0.1.

All three control schemes may be simplified to contain four generalized elements as shown in Figure 3.4: (i) the container/bath for the chlorinated hot water; (ii) the sensor to measure operational parameters; (iii) the control method to affect a change in the environment; and (iv) the analyzer system to read the sensor, log parameter values, make control decisions, and signal the control method. A unique Labview program was developed to control and monitor the overall bath conditions (pH, free chlorine, temperature, water level), provide a visual display of the conditions, record data, and provide status alerts.

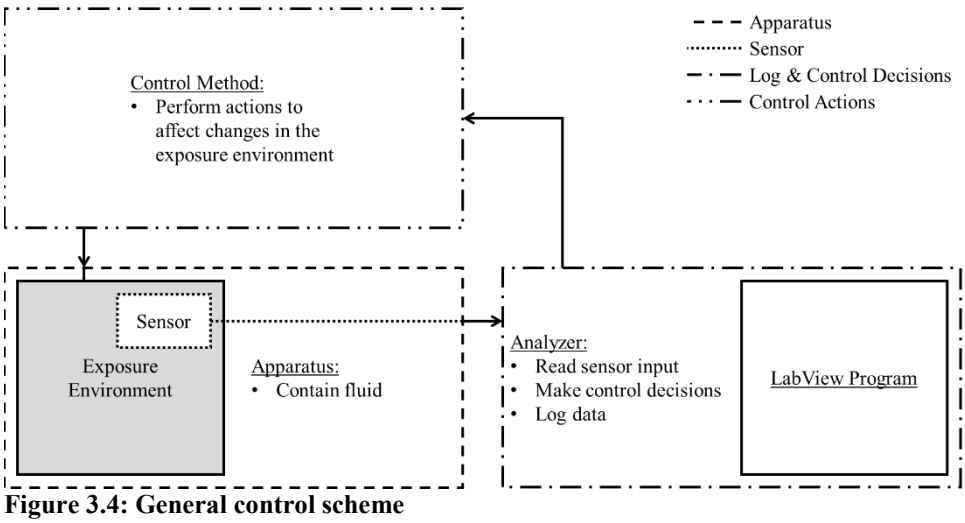

Figure 3.4: General control scheme

A standard PID controller (Figure 3.5) controls the temperature of the water within the bath. The fluid temperature is sensed by a set of thermocouples, and heat energy is supplied to the system through a thin, flexible, resistive heater applied to the outer surface of the bath. Three devices read the thermocouples: the PID controller, a limit switch, and a data acquisition card (DAQ) connected to a PC. The first two of these devices handle the control decisions and signaling, with the limit switch implemented for safety. The redundancy of the temperature measurements using the PC assures accuracy and allows the data to be logged.

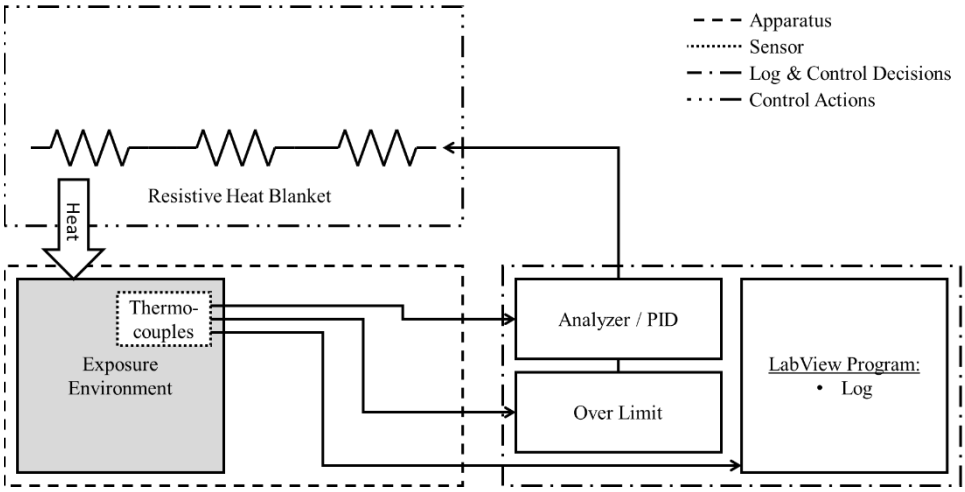

Figure 3.5: Temperature control scheme

The heater arrangement is notable and critical because the heating elements are placed on the exterior of the bath: a heater that is immersed in the bath would corrode quickly due to the oxidative environment. The bath is contained within an 18.5 L, 30 cm diameter glass jar. An 1800 W resistant heater blanket is wrapped around the bath and a 12 mm thick layer of foam is placed over the heating element to insulate the heater/bath assembly.

The pH control system is similar to the temperature control system (Figure 3.6). A commercial pH probe is held stationary within the environment and is connected to an analyzer that outputs 4-20mA to the DAQ. The Labview program includes control logic for pH. The program switches power to a solenoid valve which allows a controlled release of sodium bicarbonate ($NaHCO_3$) solution into the apparatus. A single set point is used by the program with the delivery rate for the sodium bicarbonate at either zero or a user-defined value. The ability to modify the delivery rates can accommodate changes in solution concentration.

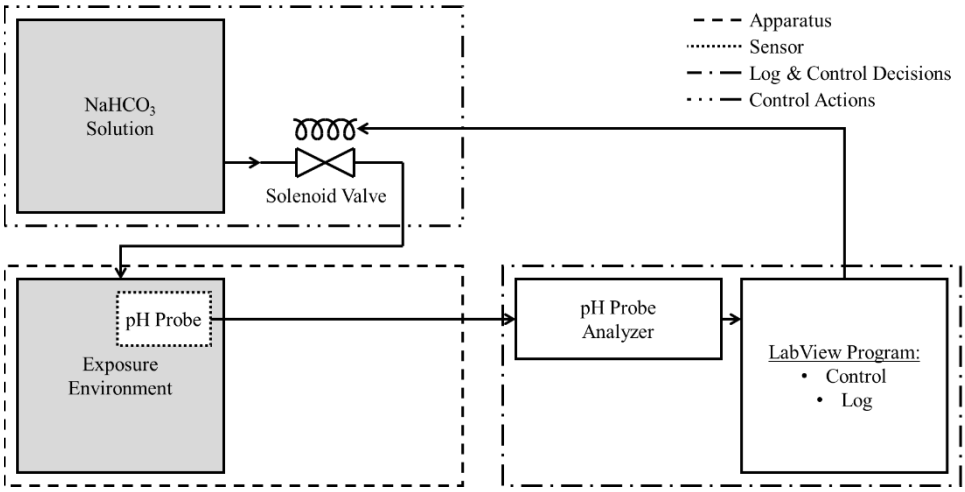

Figure 3.6: pH control scheme

The concentration of free chlorine in the bath is also controlled to a user specified range. This measurement is much more dynamic (than pH) because the chlorine within the bath can exist in as several chemical species, evaporate, decompose, or oxidize materials within the fluid. An amperometric sensor is used, which has specific requirements for flow rate, pressure, and temperature. A constant flow rate and pressure head are achieved by pumping the chlorinated water through a fluid flow cell. Because the bath temperature (60-65°C) exceeds the sensor temperature limit of 50°C, the

chlorinated water from the bath is routed through a heat exchanger prior to the sensor (Figure 3.7). The sensor signal is interpretted by an analyzer which outputs a ppm free chlorine reading to the Labview program. The control scheme is otherwise the same as for the pH control: The program switches power to a solenoid valve to deliver a sodium hypochlorite (NaClO) solution. The control program for chlorine has two set points, depending on the chlorine concentration in the bath, and two user-defined delivery rates for the solution of NaClO.

All components of the apparatus which have the potential to contact the chlorinated water were selected from materials that will not degrade extensively during sample exposure. The fluid container is a glass vessel. The pump head and liner are ceramic. In addition, even though the open surface of the bath is covered to reduce evaporation, the evaporating fluid can cause oxidation of sensors, actuators and mounting fixtures. Mounting fixtures are fabricated from polymers and inspected regularly. The solenoid valves are selected so that the fluid does not come into direct contact with the valve.

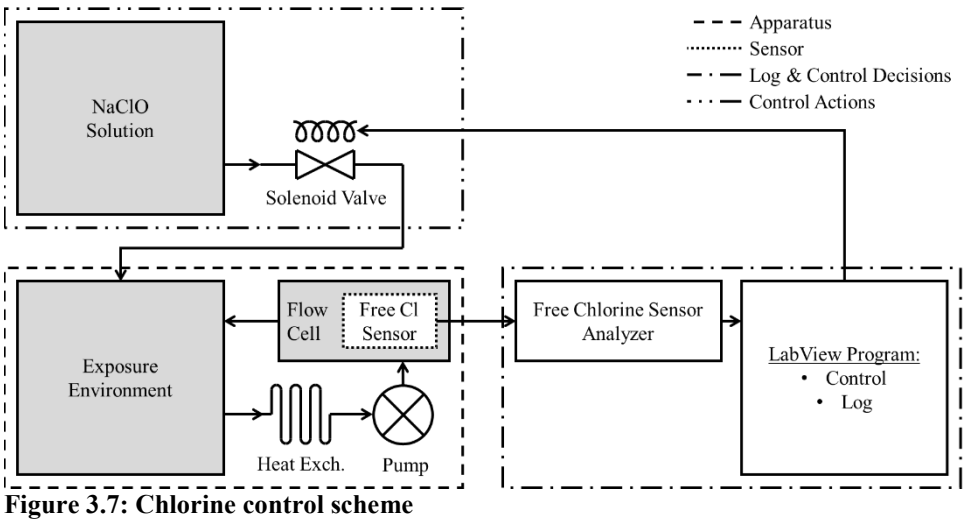

Figure 3.7: Chlorine control scheme

The layout of all equipment includes features to assure safety and with anticipation that failure might result in a leak. Two electronic float valves continuously monitor the fluid level in the bath. The low fluid level valve directly controls a solenoid valve to release RO water into the bath. The Labview program monitors the high level valve. If the water level is high, then the entire system is shut down and an alarm email is distributed to the water bath user group. There is secondary containment for the main fluid bath and all fluid line connections. Electrical devices and connections are routed outside of the fluid environment to prevent premature failure due to oxidation.

Material samples placed in the bath were exposed to the oxidative environment for up to 1250 hours (about 52 days) before being removed. Table 3.4 shows the final number of A and B series samples produced at each level of exposure.

Table 3.4: Material samples by starting crystallinity and hours of exposure

Exposure [hours]:	**0**	**250**	**500**	**750**	**1000**	**1250**
Crystalline Series "A"	17	4	15	19	16	15
Crystalline Series "B"	15	-	15	15	16	15

Chapter 4: Methods

After material samples were prepared, mechanical tests were performed to determine tensile and fracture properties for each combination of crystallinity and exposure time. Tensile characterization was performed using dog bone shaped microtensile specimens while fracture properties were determined by testing double edged notch specimens. Changes in the morphology of the materials were also characterized using gel permeation chromatography (GPC) and differential scanning calorimetry (DSC).

4.1 Tensile Characterization

To obtain tensile loading curves for the materials, dog bone specimens were tested in a load frame at several programmed strain rates. ASTM D1708 [30] microtensile specimens were selected for testing, with dimensions as shown in Figure 4.1. Specimens were fixed into the load frame by clamping the full-width area, shown hatched in Figure 4.1, at each end of the specimen with screw-tightening vice-style grips. Time, force, and displacement data were collected for each test. Additionally, images of each test were captured to be used for digital image correlation (DIC). Stress and strain curves were calculated from this data and allowed the determination of material tensile properties such as the elastic modulus, yield strength, break strength, and strain-at-break.

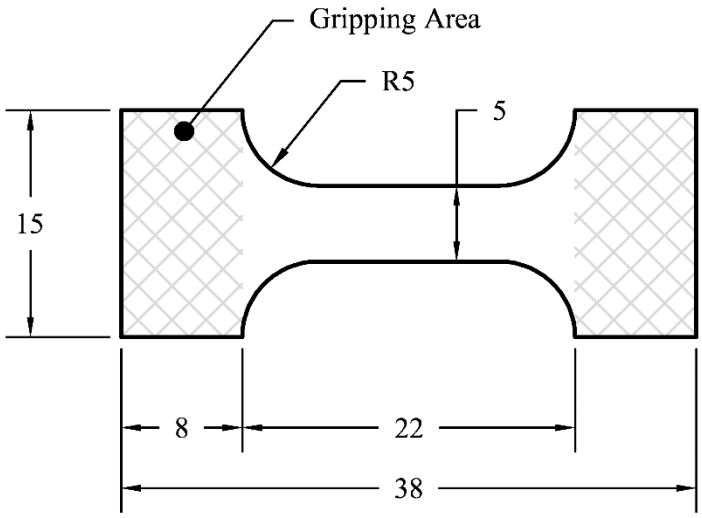

Figure 4.1: ASTM D1708 microtensile specimen, dimensions in mm

4.1.1 Tensile Testing Method

Material properties for the present work may all be derived from the engineering stress and engineering strain resulting from tensile testing methods such as ASTM D1708. For future work, however, the true stress and strain values will be required to define the constitutive behavior of the material. These values may be derived from local displacements calculated from DIC analysis of image data collected during tensile tests.

Two test methods were considered in addition to ASTM D1708 to collect tensile data for the present study: ASTM D882 [31] and D638 [32] (specifically Type V specimens). Although the ASTM documentation for D1708 lists it as being superseded "in general" by the latter two tests, it was the most appropriate for this study due to its size. The specimen shapes used for each of these tests are shown in Figure 4.2 along with the size of the material samples which were exposed in the water bath.

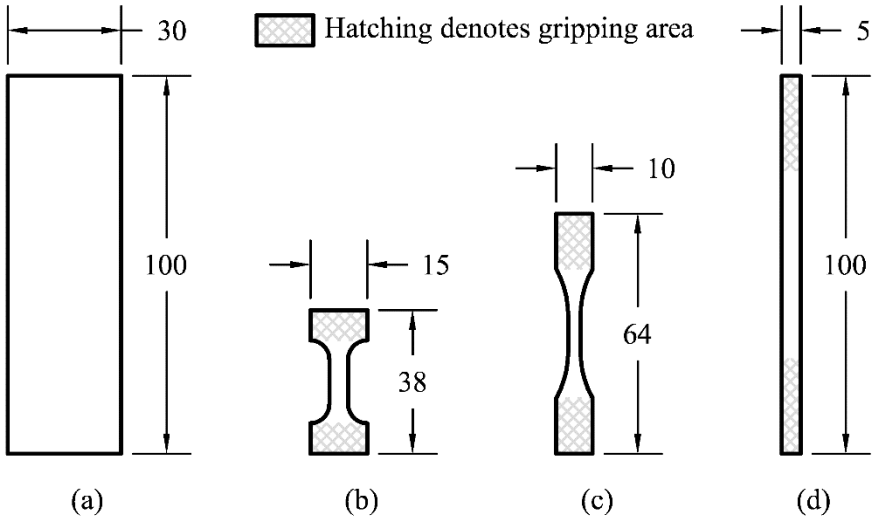

Figure 4.2: Size comparison of ASTM specimens with (a) material sample, (b) ASTM D1708, (c) ASTM D638, and (d) ASTM D882, all dimensions in mm

The D638 specimen could only allow three tensile specimens to be cut from each of the exposed samples, while up to four D1708 specimens can be cut from each material sample. The use of D882 "strip" specimens was also considered but imaging the strip specimens proved difficult. The necking region, where the most useful high strain data were sought, could easily move out of the camera field of view. This was exacerbated by tendency of the strips to fail at the point they were gripped; regions near the moving jaw were the first to extend beyond the image field of view. The short gauge length and "dogbone" shape of the D1708 specimens allowed for the necking region to remain within the field of view.

Although the D1708 microtensile geometry provides more specimens and better imaging, it does not specify the use of an extensometer for testing. Instead, engineering strain is calculated using the displacement of the load frame crosshead and the initial jaw separation as a gauge length. By measuring strain at the jaws, some error is introduced

due to the non-constant cross section through the gauge length. The lack of an extensometer is beneficial for DIC, however, as the extensometer would interfere with the field of view for the specimen.

Prior to testing, specimens were prepared by die cutting to shape and applying an appropriate speckle pattern for DIC analysis. Specimens were cut to shape using a D1708 microtensile die from Pioneer-Dietecs. All specimens were cut so the long axis was aligned with the lengthwise direction of the exposed sample and thus with the original extrusion direction. Cutting pressure was applied to the die with an arbor press as shown in Figure 4.3. A sacrificial layer of cardboard was placed under the material to avoid damage to the cutting edges of the die. The cut specimen was then taped to a sheet of paper and a random speckle pattern was produced by stamping the specimen with ink using a foam "ink blending" tool shown in Figure 4.3. The paper backing held the specimen flat for inking and provided a means for handling specimens without smearing the ink. Further considerations on the suitability of patterns are discussed in Appendix A.

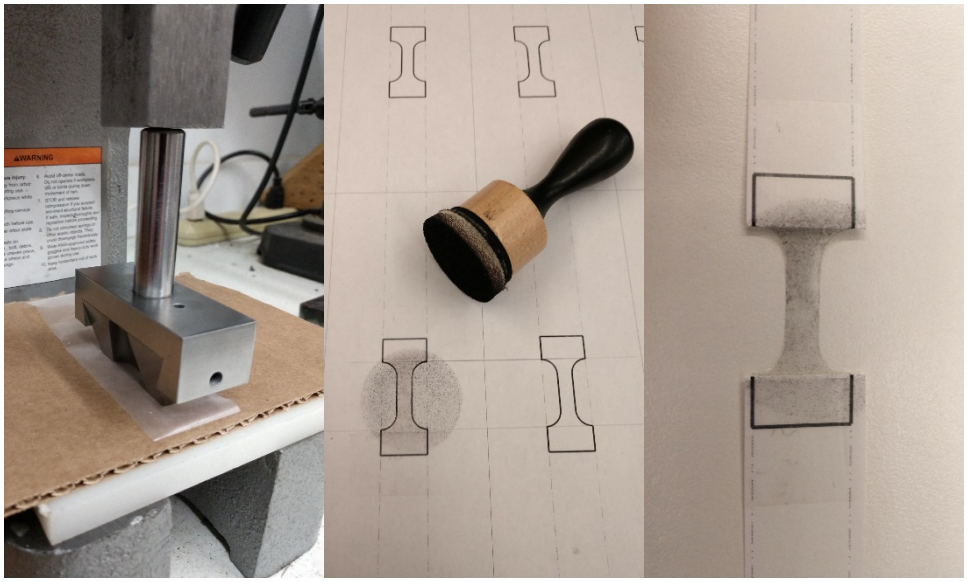

Figure 4.3: Specimen preparation showing (a) die-cutting process, (b) inking method, and (c) final resulting specimen

Tensile testing was completed using an Instron 4202 load frame outfitted with an Interface load cell (model number SM-25) and an ADMET digital controller (model eP2). The SM-25 load cell, which is rated for up to 111 N (25 lbf) of load, was selected for this study because its capacity is well matched for loads expected from the small samples. Care must be taken when using this loadcell, however, to avoid exceeding the load rating.

Load frame control and data logging were accomplished using the eP2. Four test methods were created which each controlled the cross-head velocity at a different speed, corresponding to a separate strain rate for each test. The data logging rate also varied between test methods to ensure that the eP2 could capture the entire test and that a similar quantity of data were collected for each test. Table 4.1 lists the crosshead velocity and data logging settings for each test method, along with the resulting strain rate and maximum strain recordable by the settings. Finally, test data were retrieved from the eP2 controller using GaugeSafe software from ADMET.

Table 4.1: Load frame parameters by test method

Method:	Crosshead Velocity [mm/min]	Strain Rate [sec^{-1}]	Data Logging Rate [samples /min]	Maximum Test Time [min]	Maximum Strain
1	125	1E-1	6000	1	570%
2	12.5	1E-2	600	10	570%
3	1.25	1E-3	60	125	710%
4	0.25	2E-4	10	500	570%

Images were also acquired during each test to permit DIC analysis. A FLIR Chameleon3 monochromatic camera was used with an Edmund Optics TECHSPEC® C Series 25mm fixed focal length lens. Using a working distance (between the specimen and camera) of approximately 350 mm, this permitted a 120 mm vertical field of view

which allowed the specimen to stay entirely within the imaging frame for up to 450% strain. A custom LabView program was created to control the camera and its settings including the framerate, exposure, and gain. These settings are listed in Table 4.2 for each of the four test methods. Further details on the LabView program may be found in Appendix A.

Table 4.2: Camera parameters by testing method

Method:	Frame Rate [FPS]	Exposure [µs]	Gain [dB]
1	41.67	23,000	0
2	5.0	28,000	0
3	0.5	28,000	0
4	0.1	28,000	0

The framerate setting defined the frequency for image collection, measured in frames per second (FPS). The exposure setting determined the amount of time in microseconds used by the camera image sensor to collect light. After gathering these data, the value collected for each pixel was then scaled by the gain setting in decibels. This amplification can be useful for brightening short exposure images to improve contrast, but care must be taken as any noise in the data is also increased. For this reason, a gain value of zero decibels was desired for all tests to avoid amplification and image brightness was controlled using the specimen lighting. The LabView program was also responsible for gathering image timing data necessary for correlating DIC results to the data logged by the eP2 controller. Further details concerning the selection of imaging equipment and its relation to the DIC analysis can be found in Appendix A.

4.1.2 Tensile Data Analysis

As previously discussed, a drawback of the D1708 method is that error is introduced into the strain measurement because the cross section is not constant. DIC analysis may avoid this source of error by observing displacements within the gauge section. Several specimens have been analyzed using an open source DIC program written in MATLAB (Ncorr 1.2) [33] to verify that the images are suitable for the DIC algorithms and to compare with the strain results obtained from the D1708 method. Prior to this, appropriate corrections must be made to account for any pre-loading applied to the specimens. Finally, material properties are calculated from the test data.

Figure 4.4 shows an example load-displacement plot demonstrating data collected from one D1708 test. Note that the measured load value was not equal to zero at the end of the test, despite failure of the sample. Although the load transducer was zeroed prior to each test, many of the specimens were under a small amount of tension to pull the material flat when clamping it into the test fixture. Without this tension, the specimens curled which interfered with DIC results. This pre-load was corrected by adding a compensation value to load measurements so that post-failure values were equal to zero. Load compensation values had a mean value of +1.10 N for all tensile specimens (curve shifted up to adjust for pre-tension), with a standard deviation of 0.51 N.

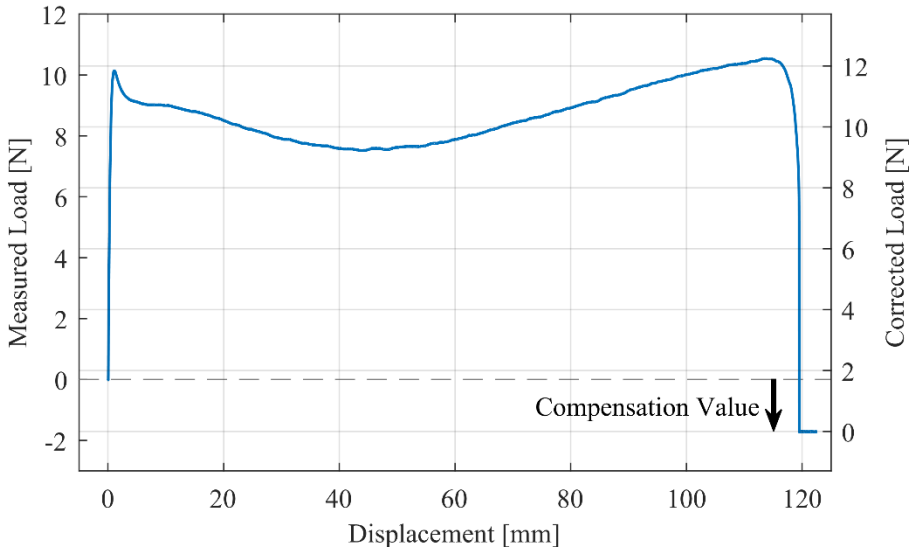

Figure 4.4: Demonstration of load compensation as applied to specimen B0000-T2-02

After the load data were corrected, a strain compensation was also applied. Figures 4.5 and 4.6 demonstrate the primary motivations for applying this correction. The first example demonstrates a specimen which was not under tension at the start of the test, requiring some displacement before this slack was removed. This "toe" region at the start of the test does not represent the response of the material. A specimen with significant pre-load is shown in the second example (the same specimen as the load correction example in Figure 4.4). Due to the applied load at the start of the test, the specimen also exhibited pre-strain.

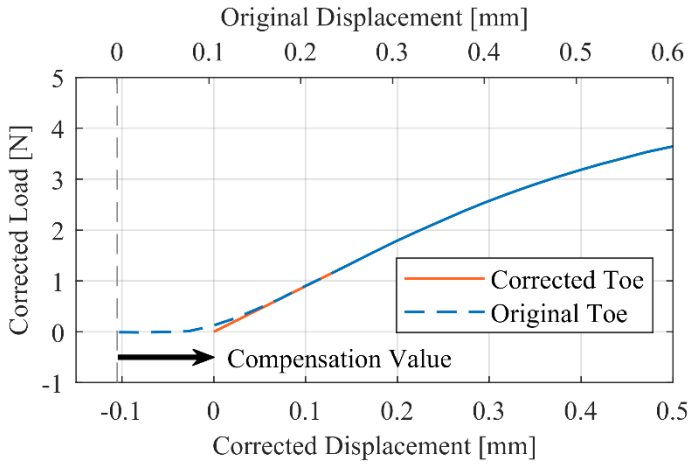

Figure 4.5: Toe compensation for specimen A0000-T4-02 with delayed strain due to take-up of specimen slack

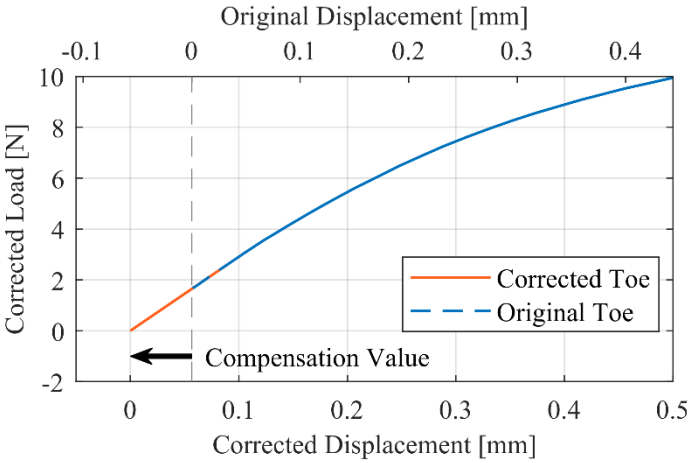

Figure 4.6: Toe compensation for specimen B0000-T2-02 accounting for specimen pre-strain

To correct for both types of error, toe compensation was applied as described in ASTM D638-14 [32]. Following this method, a tangent line is constructed through the point of maximum slope on the load-curve. This line is then extended to intercept with the displacement axis and that intersection point may be taken as zero-strain. A MATLAB script was written to locate the point of maximum slope, based on a moving mean of five data points to reduce the derivative's sensitivity to data noise. The script then calculated the zero-intersection based on this slope and the necessary offset for toe

compensation. Toe compensation values had a mean of +0.05 mm (to account for pre-strain) for all tensile specimens, with a standard deviation of 0.10 mm.

With the load and toe corrections applied, stress and strain could then be calculated for the D1708 method following the standard definitions for engineering stress (σ_{eng}) and engineering strain (ε_{eng}):

$$\sigma_{eng} = \frac{P}{t \cdot w} \tag{4.1}$$

$$\varepsilon_{eng} = \frac{\delta_{CH}}{l_{jaw}} \tag{4.2}$$

For stress calculations, all widths (w) were 5.0 mm in accordance with the dimensions of the D1708 specimen cutting die. Prior to application of a speckle pattern, four thicknesses were measured across the gauge length of each specimen using a micrometer, and the mean value was taken as the specimen thickness (t). For strain calculations, displacement was measured at the load frame crosshead (δ_{CH}). The initial jaw separation (l_{jaw}) was used as the gauge length and was set at 22 mm for all tests.

Strain values were also examined for several specimens using DIC analysis to verify that the images were suitable for analysis with Ncorr and provide strain values for comparison with the D1708 results. Four low crystallinity samples with 1E-2 (sec^{-1}) strain rates (crystallinity "A" and test method two, respectively) were selected and analyzed with Ncorr. Figure 4.7 demonstrates the DIC data obtained for one specimen and includes the original patterned image and the displacement field resulting from the DIC analysis. As can be seen, there are localized results across the entire gauge length of the specimen, which may be used to calculate a variety of strain values. Ncorr provides

the ability to calculate Eulerian and Lagrangian strain fields from the displacement data, as demonstrated in the last panel of Figure 4.7.

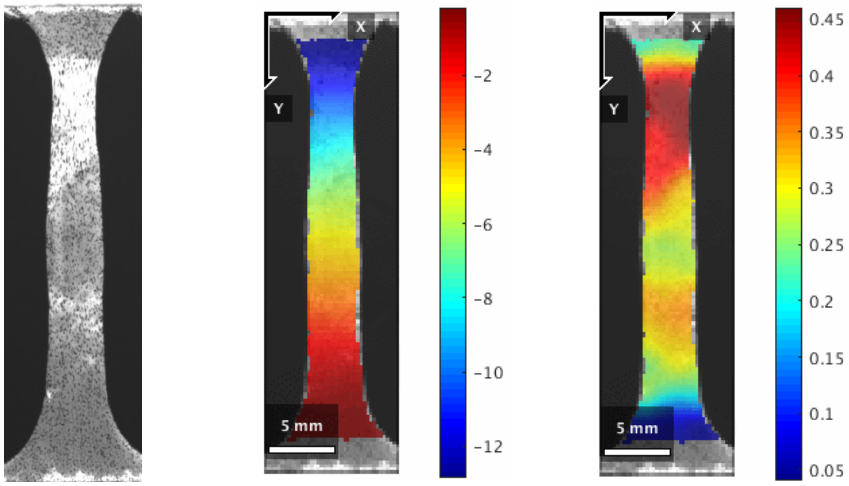

(a) **(b)** **(c)**

Figure 4.7: Digital image correlation showing (a) applied speckle pattern, (b) resulting displacement field, and (c) resulting Eularian strain field

For comparison with the D1708 data, engineering strain values must be found from the DIC data. This may be accomplished using displacement values (δ_1 and δ_2) from each end of the specimen gauge length to calculate the engineering strain:

$$\varepsilon_{eng} = \frac{\delta_2 - \delta_1}{l_0} \tag{4.3}$$

The gauge length l_0 is taken as the original distance between the observed points. Calculations using displacements from individual DIC data points proved to be susceptible to image noise, so an averaging approach was employed to reduce this error. A "virtual extensometer" method was devised, where displacement values were taken as the mean of multiple points. As shown in Figure 4.8, points were selected which were aligned across the specimen, similar to an extensometer fixed to the material.

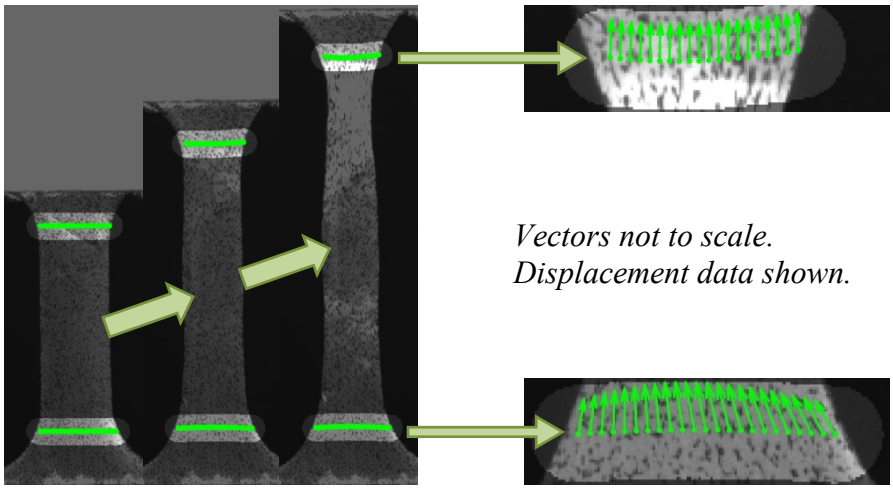

Figure 4.8: Method for calculating engineering strain from DIC results

A toe correction was also applied to the DIC strain results to account for any pre-strain or slack in the specimen. The derivative-based method described for D1708 was not used to find the toe correction values for the DIC data; the lower sampling rate for images precluded the use of the moving-mean methods employed for load frame data. Instead, it was assumed that the offset in strain values was identical for both series of tests. Figure 4.9 shows the results of this offset for one specimen and compares the resulting engineering stress-strain curves for both D1708 and DIC tests. As can be seen, the offset data is in close agreement and is suitable for comparing the two data sets.

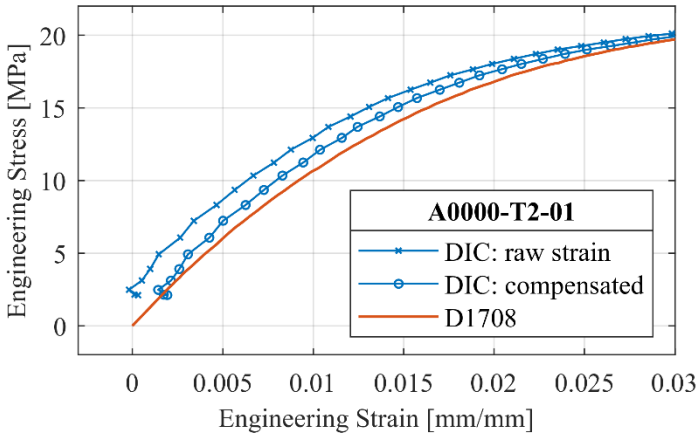

Figure 4.9: DIC toe correction, specimen A0000-T2-01

With all data corrections in place, the strain measurements for the two methods can be compared. DIC analysis was performed on four unexposed crystallinity "A" samples with similar strain rates (each used method two with 1E-2 1/sec strain rates). Images were used from the beginning of the test up to approximately 1.32mm of crosshead displacement, corresponding with 6% engineering strain for the D1708 tests. DIC displacement points were selected along two lines approximately 10mm apart and centered on the gauge length of the specimen. Figure 4.10 shows the engineering stress-strain results from both DIC analysis and D1708 testing for each of the four tests. In each these figures, stress values appear to converge as the specimen yields because both DIC and D1708 curves use the same force data collected from the load frame to calculate the engineering stress. D1708 data have been truncated at 6% engineering strain, corresponding with the final DIC image data analyzed.

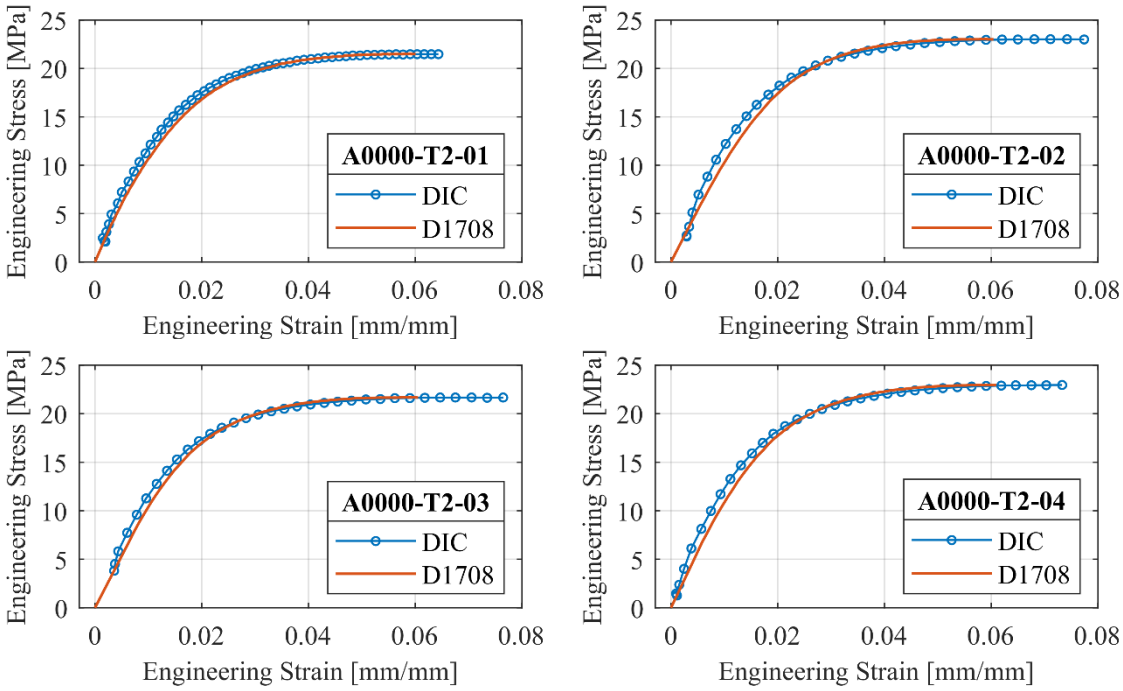

Figure 4.10: Comparison between DIC and D1708 tensile data sets for four specimens

Examining these plots, the strain values resulting from D1708 displacements (at the load-frame jaws) differ only slightly from the values calculated from DIC displacements (taken within the constant section of the gauge length). The DIC results show a steeper slope at the onset of the curve, representing a slightly larger modulus. The D1708 standard specifies that the test method should not be used for the determination of modulus of elasticity, and instead recommends test options which measure displacement over a gauge length with a constant cross section. Because the D1708 cross section varies at the radiused shoulders, it should not be expected that modulus or strain results will be fully comparable to those obtained from tests which use a constant cross section such as D882 strip specimens, D638 tests, or the DIC data discussed here. The data from the D1708 tests remain self-consistent, however, due to the consistency in testing procedure, and allows for comparisons to be made between the test specimens of this study.

To further compare the two strain measurement methods, one specimen was selected for DIC analysis over a wider range of displacement as shown in Figure 4.11. Specimen A0000-T2-01 was selected and images were analyzed up to approximately 13.2mm of crosshead displacement, corresponding with 60% engineering strain for the D1708 test. The D1708 curve in this figure has again been truncated at this value to correspond with the images analyzed for the DIC curve. This specimen was selected in part because it was used for the previous comparison, but more importantly because a faster frame rate had been utilized when capturing DIC images for the specimen. This resulted in smaller displacements between consecutive images, allowing the DIC algorithms to solve for higher displacements.

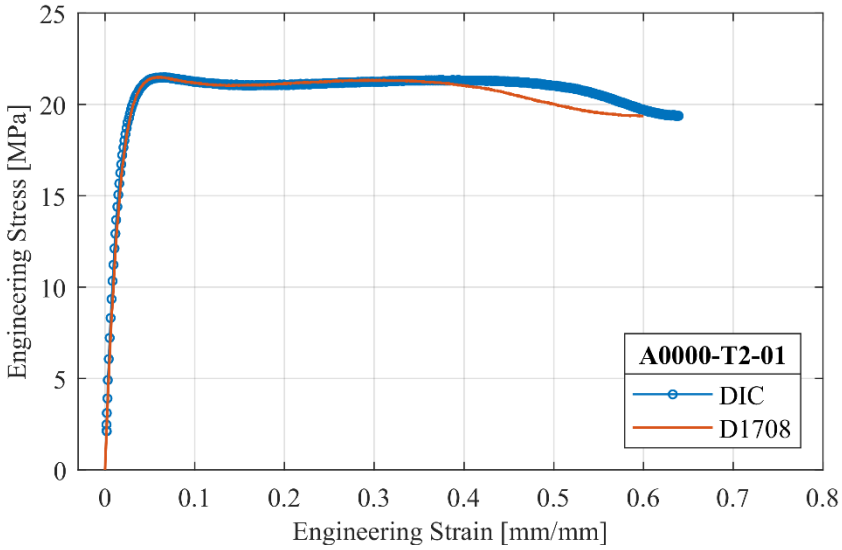

Figure 4.11: Comparison between DIC and D1708 tensile data to 60% strain

The stress-strain curve resulting from this DIC analysis is shown in Figure 4.11, along with the D1708 results over the same strain range. Examining this figure, the two strain measurements produce similar results up to the yield point of the material. Beyond the yield point, the shape of the two curves remain similar, with strain values diverging slightly. This is due to the differences in shape of the gauge section used for strain calculations. Once the specimen began yield, the deformation region comprised more of the 10 mm DIC gauge length, leading to a larger calculated strain than from the D1708 calculation which considered the entire 22 mm length between the load frame grips including the wider (and thus stiffer) radiused sections.

Strain values for the D1708 test are comparable within this study because the testing methods used for gathering data and the gauge lengths used in calculations are consistent. Similarly, trends in the material response due to degradation are comparable for data within this study. The DIC image data collected also provide a foundation for future study to examine true stress and true strain characteristics.

Several material properties for each specimen are derived from the engineering stress-strain data for the D1708 tests. The modulus corresponds to the steepest slope for the curve leading up to the yield point of the material. This point is coincident with the steepest load-displacement point, which is determined in Matlab for the toe-compensation calculations. The modulus is calculated using the stress and strain values at this same point. The yield strength is the stress value at the first peak of the stress-strain curve, as demonstrated in Figure 4.12. Using Matlab, this point is located by searching for the first data point where stress does not increase from the previous point (i.e. the first point with zero slope).

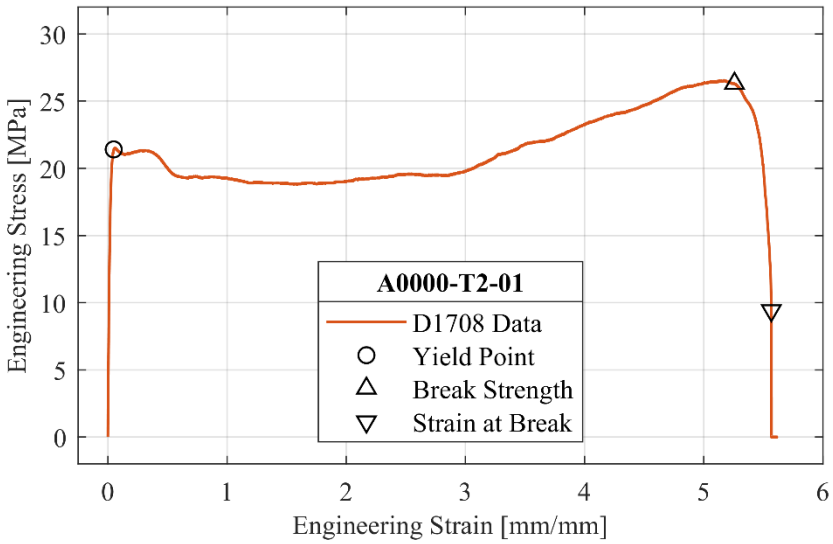

Figure 4.12: Property determination points for tensile test data

The break strength and strain at break are also calculated from the D1708 data. As can be seen from the example in Figure 4.12, many specimens did not break instantaneously. The strain at break corresponds to the strain at total failure; Matlab is used to locate the strain value immediately preceding the largest drop in load at the end of the test. The break strength is defined as the stress at the onset of failure. Matlab is again

used to locate this point by finding the last point on the curve with zero slope (preceding the total failure point from strain at break).

4.2 Fracture Characterization

The fracture characteristics of the materials are determined by the essential work of fracture (EWF) method, according to procedures recommended in *Essential Work of Fracture* [34]. While originally developed for the analysis of ductile sheet metals [35], this method is commonly applied to determine plane stress toughness response for ductile polymers such as HDPE [36]. Tests were performed on double edge notch tensile (DENT) specimens, with geometry as shown in Figure 4.13. Specimens were fixed into the load frame by clamping at each end of the specimen with screw-tightening vice-style grips to leave a 50 mm gauge length as shown by the hatched areas in Figure 4.13. Load and displacement data were collected for each test and examined for compliance with recommended criteria to ensure that the test series met the requirements for EWF anaylsis before the essential work of fracture was calculated.

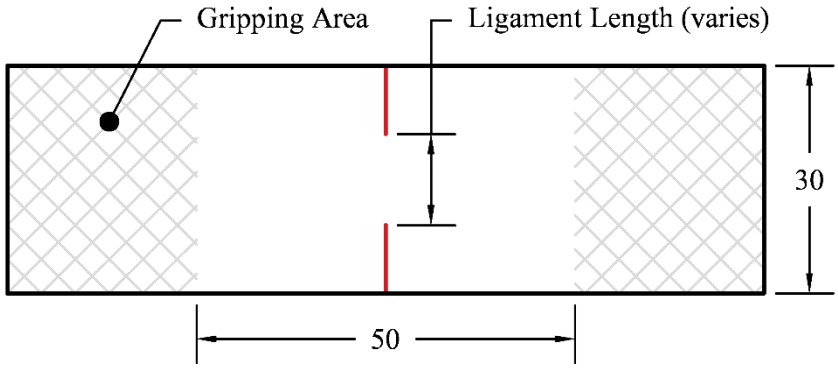

Figure 4.13: DENT specimen geometry, all dimensions in mm

4.2.1 Notch Testing Method

The overall dimensions of the DENT specimens matched the width and length of the exposed samples, 30mm wide and 100 mm long. These dimensions were selected to avoid extra cutting and handling of the specimens. Four ligament lengths were selected to cover the recommended range for the essential work method: 6mm, 8mm, 12mm, and 16mm. Notches were created by pushing a razor blade into the sample using the jig shown in Figure 4.14 to control the alignment and depth of the cut. A minimum of twelve specimens were prepared for each combination of crystallinity and exposure, with three specimens cut at each ligament length.

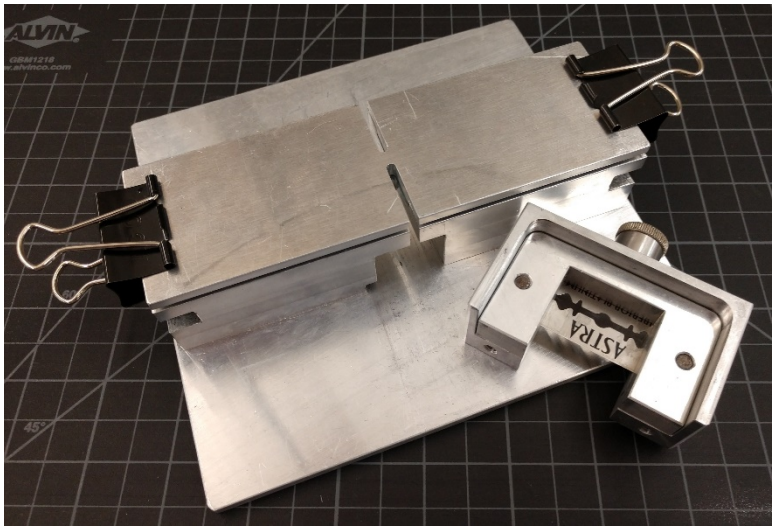

Figure 4.14: DENT notch cutting jig

Once the specimens were prepared, they were tensile tested at a constant displacement rate using the Instron 4202 load frame and ADMET eP2 controller described previously for tensile testing. For all DENT tests, the grip spacing was 50 mm and the load frame crosshead velocity was set to 10 mm/min. The eP2 controller provided time, crosshead displacement, and load data. The image acquisition system was again

used to record the tests; no speckling patterns were applied to the specimens for later DIC analysis, however. Image were collected at rates between 10 and 20 frames per second, with the camera set to automatically adjust exposure and gain settings. The same LabView program was used to control the camera and collect image timing data. Figure 4.15 shows the raw data load-displacement curves for the twelve A0000 specimens tested.

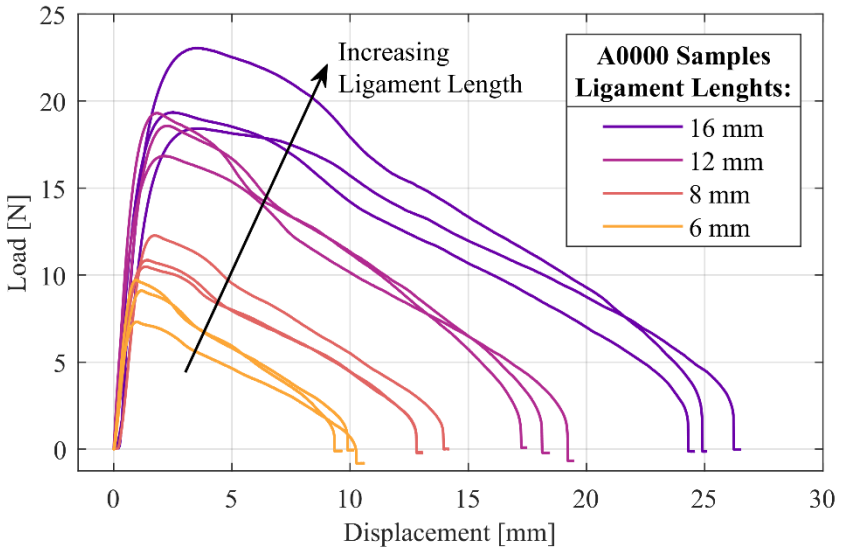

Figure 4.15: Load-displacement plots for A0000 DENT specimens

4.2.2 Notch Data Analysis

Before applying the essential work of fracture method, several conditions should be verified. First, the method assumes that data come from specimens of the same material with equal thicknesses; the resulting load-displacement curves should demonstrate self-similarity. Specimens should also exhibit yielding before fracture occurs. A stress criterion is also suggested in *Essential Work of Fracture* to ensure that data represent a consistent plane stress state [34].

Each crystallinity-exposure combination exhibits unique characteristic curves as can be seen in Appendix C and can be treated as a unique material when performing analysis with the essential work of fracture method. It should be noted that *Essential Work of Fracture* recommends a minimum of 25 specimens to ensure enough data are available for the regression analysis [34]; in the present study, a minimum of only 12 specimens have been used for each crystallinity-exposure combination. Although this provides fewer data points for individual regressions, the results will ultimately be compared across exposure levels, providing a minimum of 60 specimens for each crystallinity. The self-similarity of one crystallinity-exposure combination can be examined in Figure 4.15. Although the shapes of these curves are quite similar, some of the smaller ligament specimens demonstrate higher loads than specimens with longer ligaments; this is due to inconsistencies in the material thickness.

To better compare data between specimens, three compensations are applied. First, two compensations account for any pre-load and pre-strain in the specimens; these are applied following the same load and toe correction procedure described previously for tensile testing. Load compensation values had a mean value of +0.12 N for all tensile specimens (positive to account for pre-tension), with a standard deviation of 0.51 N. Toe compensation values had a mean of -0.14 mm (negative to account for toe region from remaining slack) for all tensile specimens, with a standard deviation of 0.12 mm. Next, load data are normalized by material thickness according to the following formula:

$$P_{norm} = \frac{\bar{t}}{t_{test}} P_{test} \tag{4.4}$$

Where P_{test} and t_{test} are the measured loads and thicknesses for each specimen, and $\bar{t}$ is an average specimen thickness. Specimen thicknesses are calculated as the mean of four micrometer measurements. The average thickness is the mean of all specimen thicknesses. This normalization is useful when comparing data plots to remove the effects of variation in material thickness. After normalization, the curves for each ligament length reach similar maximum load values, as can be seen in Figure 4.16. As ligament lengths increase, the maximum load, and displacement also increase.

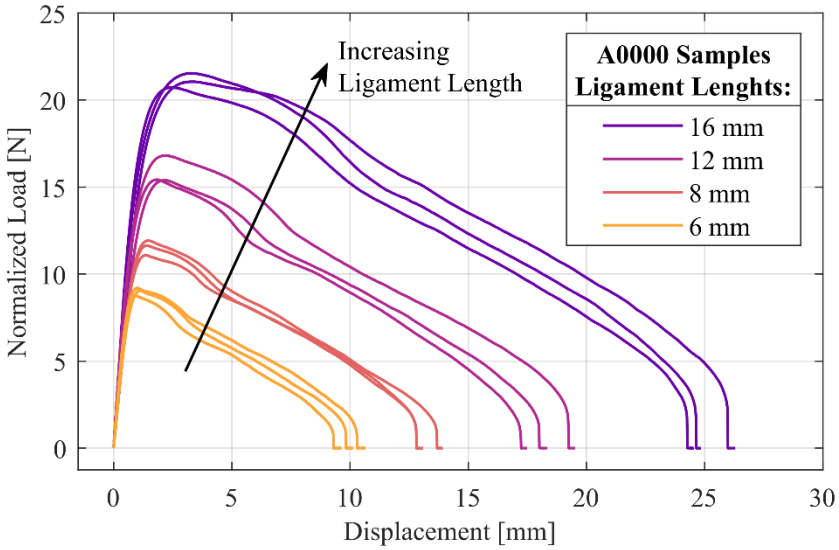

Figure 4.16: Compensated load-displacement plots for A0000 specimens

An additional characteristic desired for EWF tests is that the specimen should yield before the onset of crack growth. This "yield-before-fracture" criterion was achieved in multiple ways; first, the gauge length ($h = 50\ mm$), and crosshead velocity $\left(V = 10\ \frac{mm}{min}\right)$, were selected to satisfy the equation:

$$V = 0.2\left[\frac{1}{min}\right] * h \tag{4.5}$$

as recommended in *Essential Work of Fracture* [34]. Additionally, undegraded samples were tested and crazing zones were visually examined to ensure the testing method produced yielding. Figure 4.17 shows specimen A0000-F08-03 where the crazing zone is apparent as the white opaque area in the image and demonstrates yielding of the sample.

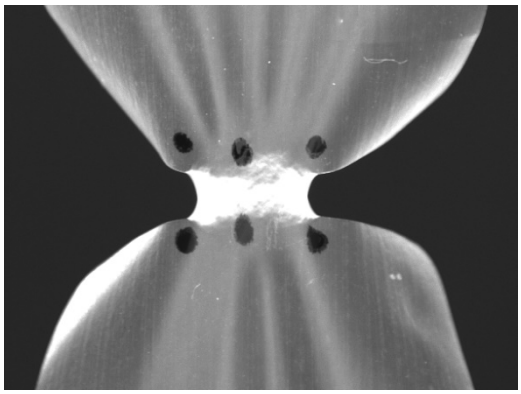

Figure 4.17: Example crazing zone for specimen A0000-F08-03

Degraded samples exhibit increasingly brittle behavior. Yielding zones were generally smaller and changes occurred rapidly making visual determination of the yielding criteria difficult. For these samples, the data were evaluated to determine if the specimen yielded before sudden crack growth. Figure 4.18 shows two example tests from brittle samples which were exposed for 1000 hours. The load curves are shown for each (without toe compensation) along with images of the crack tip shortly before fracture occurred. For the first specimen, B1000-F08-02, yielding is apparent as a narrow crazing region in the image. Corresponding to this, the data plot shows yielding as the stress smoothly passes a maximum value. In the second specimen, B1000-F12-01, this curve is replaced with a sharp point as the specimen breaks before the stress can pass a maximum; A crazing zone is also not apparent at the crack tip in the image. Specimens were

determined to yield first if their loading curve remained continuous until it passed a maximum yield stress.

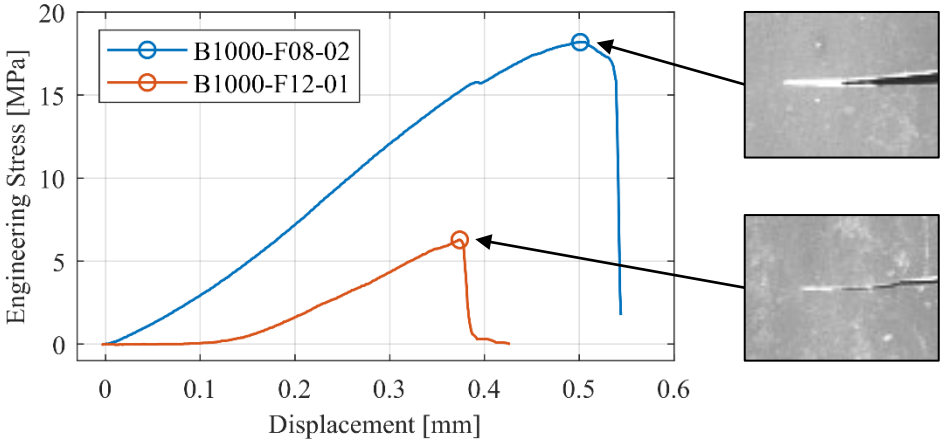

Figure 4.18: Example load curves and notch images for tests with and without yield-before-fracture conditions

The maximum stress was examined for each specimen as demonstrated for unexposed A specimens in Figure 4.19. As suggested in *Essential Work of Fracture* [34], the theoretical maximum ligament stress is also shown as a check. This value is calculated as $1.15\sigma_y$ using the tensile yield strength and should be of the same order as the data; this value is derived from the theoretical maximum stress for a long specimen symmetrically notched and in plane stress conditions [36,37]. Method two tensile specimens were selected for this comparison as their time-to-yield was most comparable.

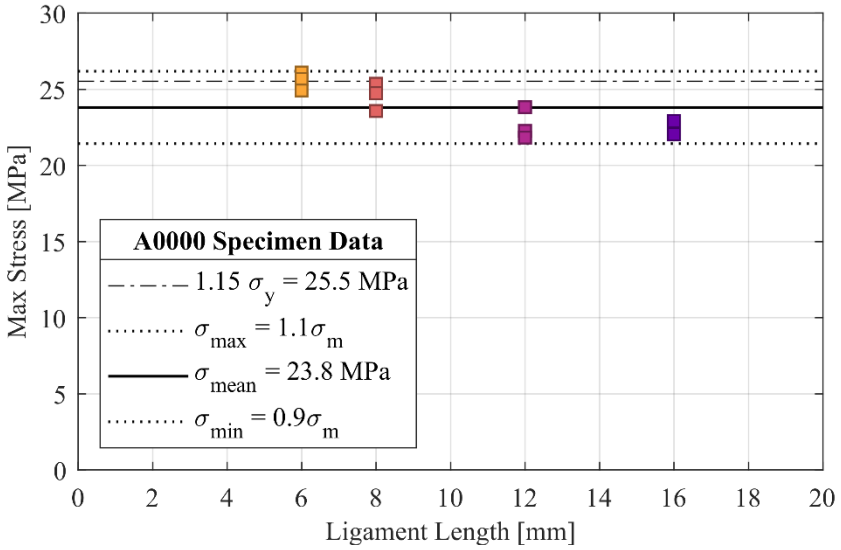

Figure 4.19: Maximum stress versus ligament length for A0000 DENT specimens showing tensile yield strength comparison and standard mean ± 10% cutoff values

In addition to this check, Figure 4.19 also demonstrates a stress criterion suggested by *Essential Work of Fracture* [34]. For this criterion, the mean maximum stress value is calculated (σ_{mean}), and data are rejected for any specimens with maximum stresses deviating beyond an arbitrary 10% of this mean. The upper limit of this criterion ensures that data are collected under plane stress conditions, while the lower limit is intended to remove specimens exhibiting premature crack growth. As this criterion is intended for use with a single material, application to the current study would require separate cutoff values for each crystallinity-exposure set. However, due to the variation in maximum stress values of degraded specimens visible in Figure 4.20, the suggested 10% cutoff values would result in the elimination of more data than desired.

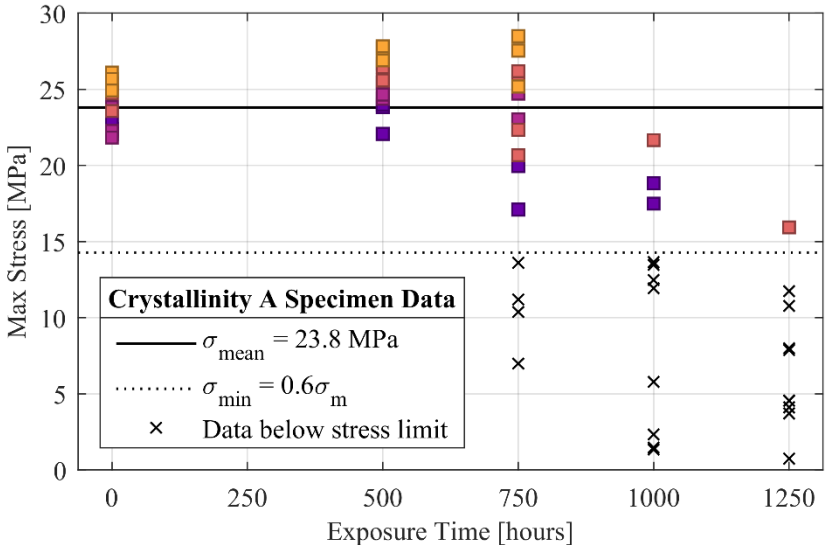

Figure 4.20: Maximum stress versus exposure time for all A samples demonstrating data cutoff at 60% mean maximum stress of undegraded samples

To retain data from the exposed specimens in the present study, a modified stress criterion has been applied; data were rejected only for specimens with maximum stress less than 60% of the mean value from unexposed specimens. This cutoff is illustrated in Figure 4.20, along with the mean of unexposed maximum stress values. Following this modified criterion, a single cutoff value was used for each crystallinity series (A and B) and was applied across all exposure levels. This cutoff was set at 60% based on observation of the specimen load-displacement curves. Most specimens which displayed poor self-similarity or premature brittle failure fell below this cutoff, minimizing the need to manually reject specimen data which did not meet the conditions for the EWF method.

Following the EWF method, the total work of fracture W_f is calculated for each specimen by finding the area under the load-displacement curve. It is then assumed that this total work can be broken into two terms:

$$W_f = W_e + W_p \tag{4.6}$$

The first term, W_e, is the essential work required to create and propagate a crack during failure. The second term, W_p, is the non-essential or plastic work, which accounts for all other energy dissipated during the fracture. This second term primarily describes the work required for plastic deformation in the outer plastic zone surrounding the crack. Assuming that the essential work is proportional to the ligament cross-sectional area and the plastic work is proportional to the volume of the outer plastic zone, equation 4.6 may be re-written:

$$W_e = w_e l t \tag{4.7}$$

$$W_p = w_p \beta l^2 t \tag{4.8}$$

$$W_f = w_e l t + w_p \beta l^2 t \tag{4.9}$$

Here, l represents the ligament length, and t is the specimen thickness. A shape factor, β, is also introduced in the volume term to account the geometry of the plastic region. Finally, equation 4.9 is normalized by the ligament area lt to arrive at the equation for the specific total work:

$$w_f \left(= W_f / lt \right) = w_e + \beta w_p l \tag{4.10}$$

Noting that the terms w_e, the specific essential work, and βw_p are considered fracture parameters and constant for a given material, equation 4.10 demonstrates that a linear relationship is expected between the specific total work and ligament length values. Figure 4.21 shows the specific total work values calculated for the twelve A0000 specimens tested, along with a linear regression for the data. The fracture properties w_e and βw_p are determined as the intercept and the slope, respectively, of this regression.

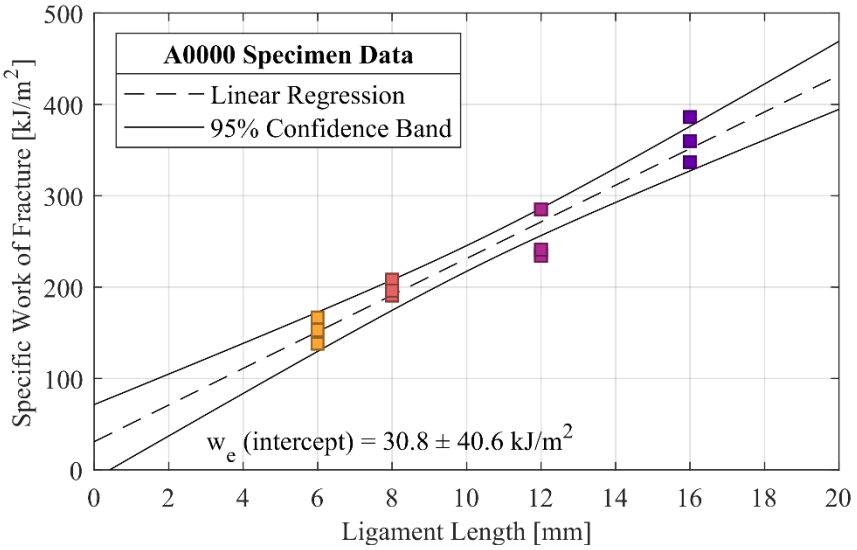

Figure 4.21: Linear regression for A0000 specimen data showing 95% confidence intervals for the regression and essential work results

4.3 Morphological Characterization

To examine morphological changes resulting from degradation, crystallinity and molecular weight were examined. Differential scanning calorimetry (DSC) tests were performed to measure the mass percent crystallinity. The number average molecular weight (M_n) and weight average molecular weight (M_w) were determined through gel permeation chromatography (GPC) tests.

4.3.1 Crystallinity Measurement

DSC testing was performed on a TA Instruments Q2000 controlled by TA Instrument Explorer software. Specimens were held in standard aluminum sample pans (DSC Consumables Incorporated #84003), which allowed a crimped seal to be formed over specimens cut with a standard 5mm diameter hole punch. Three to four material samples were stacked together and hole-punched simultaneously to form each specimen.

By punching through multiple samples, the layers held together in a 'puck' which was easier to handle than thin disks cut from individual sheets (which tended to curl and push out from the pans). Specimen weights ranged between 5.6 mg and 8.0 mg. During testing, the instrument recorded heat flow data while specimen temperatures were ramped from 0°C to 175°C at a rate of 10°C per minute, as shown in Figure 4.22.

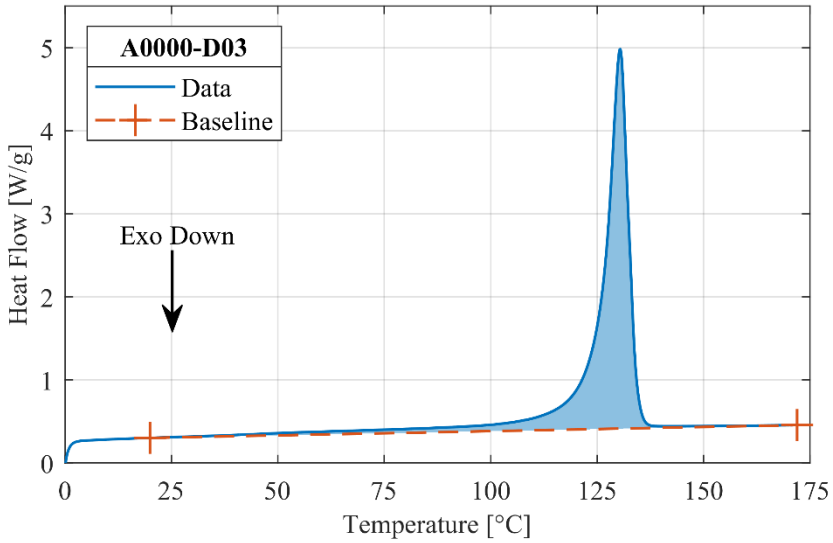

Figure 4.22: Example DSC data for unexposed A specimens

The heat of melting (H_m) for the specimen was then calculated as the area under the heat flow curve between 20°C and 175°C, as represented by the shaded area in Figure 4.22. The mass percent crystallinity was then calculated by comparing this enthalpy to the heat of melting for 100% crystalline material (H_m^*) according to the equation:

$$\%\ Crystallinity = \frac{H_m - H_c}{H_m^*} \tag{4.11}$$

For polyethylene, the reference value of H_m^* is equal to 293.6 J/g. The heat of cold crystallization (H_c) was equal to zero for all tests as no crystallization peaks were present. Calculations were performed within TA Instruments Universal Analysis 2000 software, which also provided melt onset temperatures and peak melt temperatures.

4.3.2 Molecular Weight Measurement

GPC testing was performed on an Agilent PL-GPC 220 System controlled by Cirrus GPC software. Two Agilent PLgel 10 µm MIXED-B columns were installed in the system with a column set length of 600mm. Between 1.5-2.0 mg of sample material was cut and weighed for each specimen before dissolving in trichlorobenzene (TCB) at a concentration of 1.5 mg of sample material per 1.0 mL of TCB. Specimen solutions were then hermetically sealed in glass vials and placed into the autosampler. Testing was performed at a set temperature of 135°C and a flow rate of 1.0 mL/min for 40 minutes per specimen. Refractive index sensor data in millivolts were recorded by the software at a rate of once per second. Within the software, a baseline was drawn for each specimen by selecting data points before and after the peak measured for the specimen. Figure 4.23 demonstrates millivolt response measurements versus retention time for one specimen after the subtraction of this baseline.

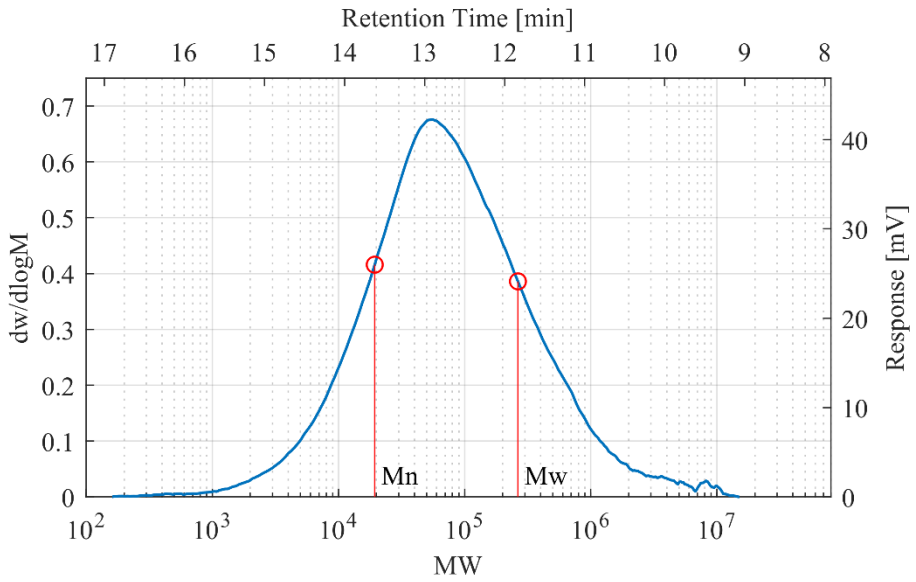

Figure 4.23: Example GPC data and results for specimen A0000-16-G2

This retention time is related to the length of polymer molecules exiting the column (shorter chains take a longer due to passing through more pores). Molecular weight values may be calculated for each time step based on the calibration of the GPC system and Mark-Houwink parameters for the calibration material (polystyrene, K=30.1, α=0.75) and specimen material (polyethylene, K=30.1, α=0.75). The resulting molecular weight scale is shown in Figure 4.23. Additionally, the weight fraction per log molecular weight increment (dw/dlogM) is shown. These values were calculated from the refractive index response, which is proportional to concentration. The number average and weight average molecular weight values (M_n and M_w respectively) for the test specimens were then calculated based on the equations:

$$M_n = \frac{\sum(dw/dlogM)}{\sum[(dw/dlogM)/MW]} \quad \textbf{(4.12)}$$

$$M_w = \frac{\sum[(dw/dlogM)*MW]}{\sum(dw/dlogM)} \quad \textbf{(4.13)}$$

where Mn and Mw are the number average and weight average molecular weights, respectively. All calculations were performed within Cirrus GPC software which also provided polydispersity (M_w/M_n) values.

Chapter 5: Results and Discussion

5.1 Chemical Properties

Resulting mass percent crystallinity values are shown in Figure 5.1 versus the material exposure time for each DSC specimen with point series representing A samples and B samples. These data demonstrate that the crystallinities of B samples were higher than that of A samples throughout the range of exposure times. Further, the crystallinities of both A and B samples increased with increasing exposure times.

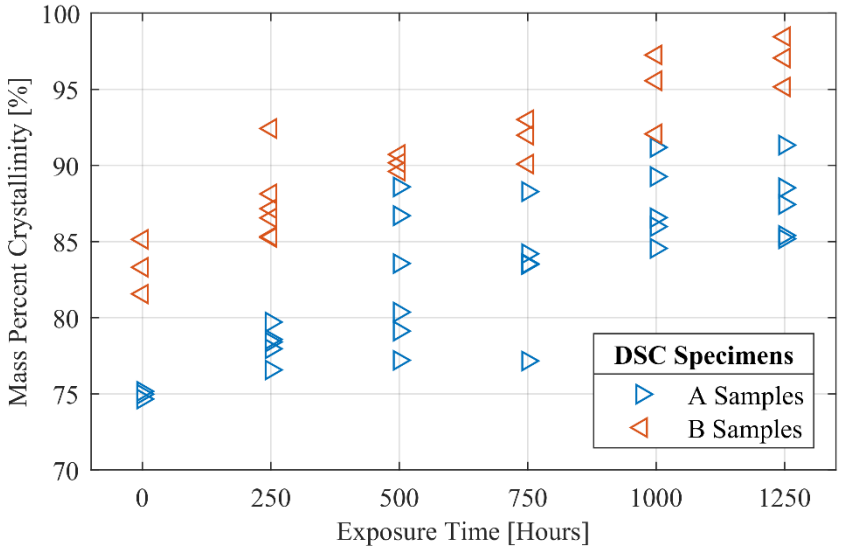

Figure 5.1: Mass percent crystallinity versus exposure time for A and B samples

At zero hours, mean percent crystallinities of 75% and 83% were measured for A and B samples respectively. This indicates that the heat-treatment method was effective and generated an increase of approximately 8% in the mass crystallinity. This was the expected outcome of holding the samples at the elevated temperature, which created greater chain mobility within the material and allowed more chains to become aligned with the crystalline region.

The conditions within the bath again held material samples at elevated temperatures, also resulting in increased chain mobility. Degradation within the waterbath produced chain scissions; the resulting shorter chains would also be more mobile and could more easily align with the crystalline region. The increase in crystallinity over time shown in Figure 5.1 can be explained by the combined results of these thermal and chemical crystallization processes.

A series of molecular weight distribution plots is demonstrated in Figure 5.2 for select A samples at each exposure time. A decrease in molecular weight is apparent by observing the peak of these distributions, which shifts towards lower molecular weight values as exposure time increases. This demonstrates that the combination of thin samples in the water bath apparatus was effective at degrading the polymer.

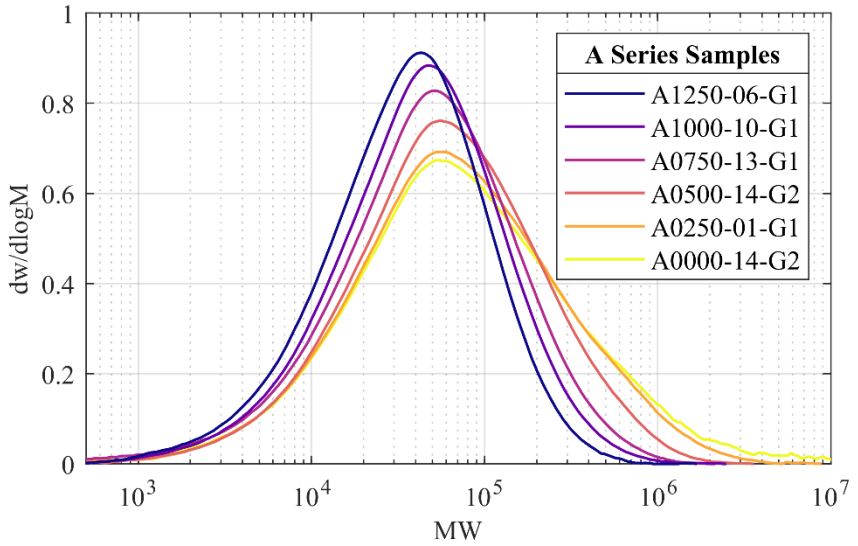

Figure 5.2: Molecular weight distribution plots for A samples at each exposure level

This figure illustrates a loss in weight fraction at higher molecular weights and corresponding increase at lower weights. This increase at lower weights demonstrates the occurrence of chain scission which generates short chains by dividing existing chains.

The greater loss of weight fraction at higher molecular weights is likely due to preferential chain scission. Scissions are more likely to occur in amorphous regions where free radicals can more easily diffuse to initiate degradation reactions. Because the amorphous regions contain a high fraction of long polymer chains, scission events are more likely to affect the chains with larger molecular weights [14].

Weight average molecular weight data are shown in Figure 5.3 versus exposure time. Data are shown for each GPC specimen with added markers to differentiate between A specimens and B specimens. Consistent with the results from Figure 5.2, degradation is evident as a decrease in molecular weight values as exposure time increases. For higher exposure times, the rate of degradation appears to slow and the molecular weight levels off. Recalling that crystallinity increased with exposure time, the decrease in degradation speed can be explained by the reduction of amorphous regions where the chain scissions are most likely to occur.

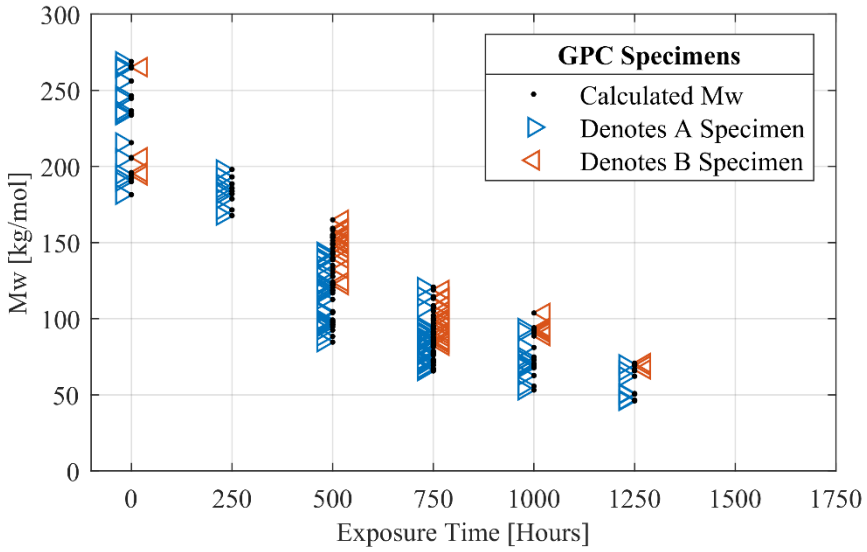

Figure 5.3: Weight average molecular weight GPC results for all A and B Specimens

Table 5.1 lists mean molecular weight values for A and B samples for each exposure time, along with the standard deviation from each set. From this table and the previous figure, it is evident that B specimens experienced a smaller decrease in molecular weight over the range of degradation times. The higher crystallinities of the B samples can once again explain the lower rate of chain scissions.

Table 5.1: Number of specimens, mean Mw, and Mw standard deviation for GPC tests

	A Samples		B Samples	
Exposure Time [hours]	**Specimen Count**	**Mean Mw ± σ [kg/mol]**	**Specimen Count**	**Mean Mw ± σ [kg/mol]**
0	18	233 ± 30	4	215 ± 34
250	9	183 ± 10	0	—
500	30	115 ± 18	20	148 ± 11
750	34	82 ± 13	18	99 ± 11
1000	13	72 ± 12	6	94 ± 5
1250	7	56 ± 10	3	69 ± 2

The standard deviations shown in the table also trend towards smaller values for increased exposure times. Sources for variance in molecular weight values can be attributed to the combination of measurement accuracy and experimental variation. When considering measurement accuracy, recall that the retention time for GPC measurements is inversely related to the logarithm of molecular weight; equal errors in time measurement result in larger variances for high molecular weights than for low weights. Variation in degradation rates is also expected between material samples due to differences in thicknesses or placement within the waterbath, leading to increased spread in molecular weight data as exposure proceeds. At high exposure times, molecular weight values begin to converge as the increasing crystallinity prevents further degradation.

The primary mechanism by which thickness affects degradation rate is through diffusion; a longer time is necessary for radicals to penetrate thick samples and initiate

oxidation reactions. To examine these effects, a normalized time was calculated for each GPC specimen based on equivalent diffusion concentration profiles within the samples. This was developed by examining the solution to Fick's second law, which relates concentration (C) to time (t) and position (x) [38]. The specimens may be represented by the domain $0 < x < l$ (where l is the specimen thickness) and $t > 0$ with an initial concentration of zero ($C(x, 0) = 0$) and prescribed boundary concentrations ($C(0, t) = C(l, t) = C_\infty$). Under these conditions, the diffusion equation yields the solution

$$C(\hat{x}, \hat{t}) = C_\infty + C_\infty \sum_{n=1}^{\infty} \frac{2}{n\pi} (\cos(n\pi) - 1) \sin(n\pi\hat{x})\, \mathrm{e}^{-\hat{t}(\mathrm{n}\pi)^2} \quad \textbf{(5.1)}$$

$$for: \qquad \hat{t} = \frac{tD}{l^2} \qquad \hat{x} = \frac{x}{l} \quad \textbf{(5.2)}$$

From this solution, it is evident that concentration profiles will be equal for specimens with differing thicknesses when their time parameters ($\hat{t}$) are equal. Normalized times were calculated for each specimen by equating their time parameters with that of an average-thickness specimen:

$$\hat{t} = \frac{t_n D}{l_n^2} = \frac{t_{norm} D}{l_{mean}^2} \qquad \xrightarrow{gives} \qquad t_{norm} = \left(\frac{l_{mean}}{l_n}\right)^2 t_n \quad \textbf{(5.3)}$$

Figure 5.4 and Figure 5.5 demonstrate these normalized time values versus molecular weight for A and B specimens respectively. Many samples demonstrate the expected relationship, with thicker specimens (lower normalized times) exhibiting higher molecular weights; examples include the 250 and 500 hour A specimens. This correlation does not appear to be strong, indicating that normalized time does not provide a major accuracy increase for predicting material degradation. The general shape and variation of the data, however, is consistent with the data plotted using exposure time.

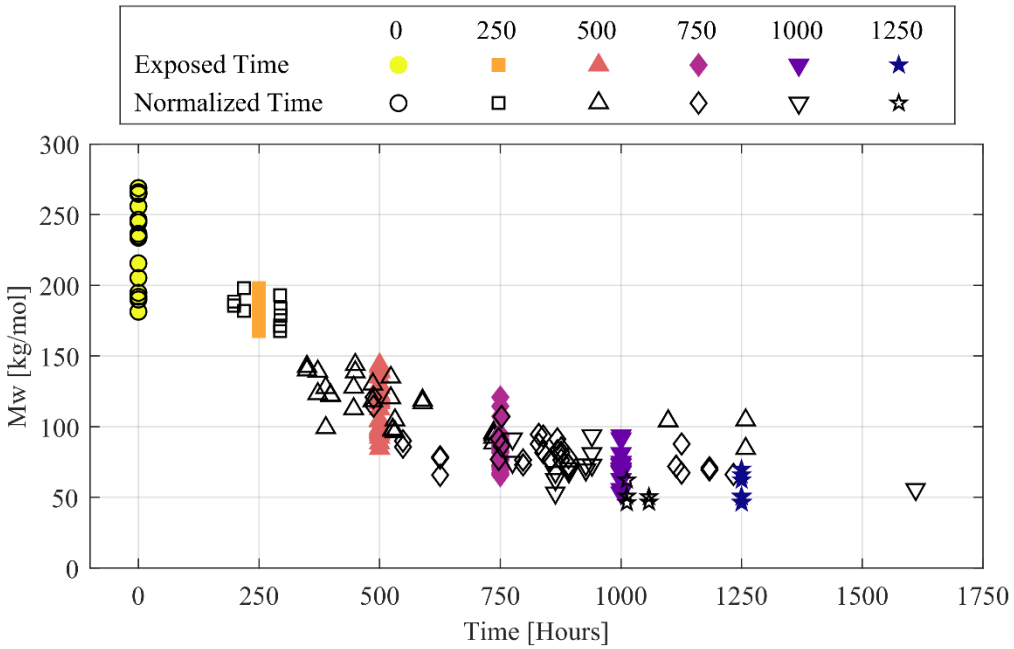

Figure 5.4: Weight average molecular weight for A specimens, shown versus exposure time and thickness-normalized time

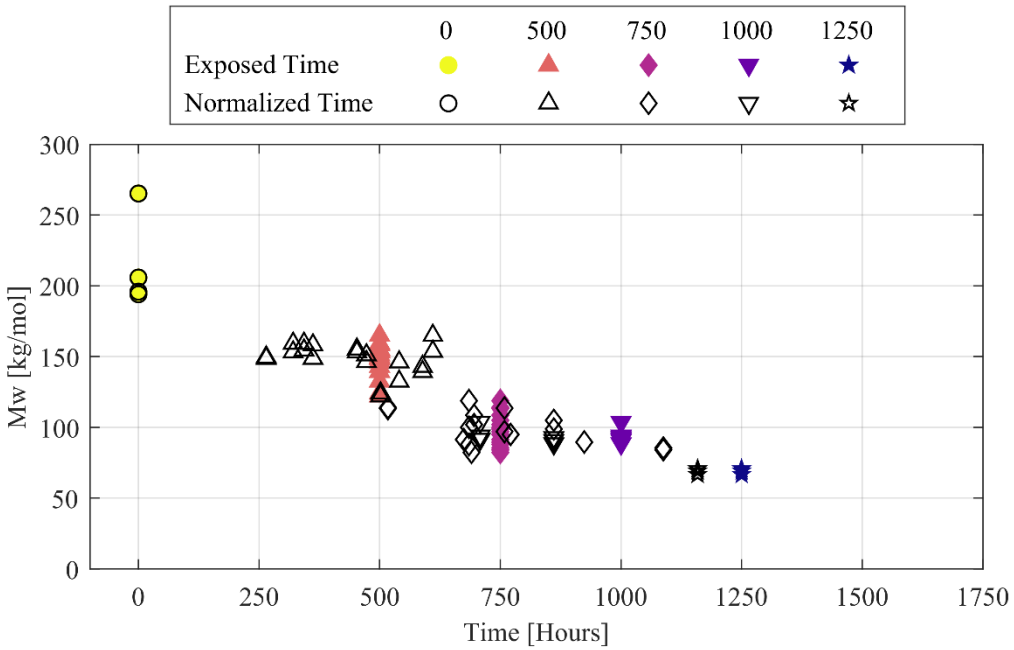

Figure 5.5: Weight average molecular weight for B specimens, shown versus exposure time and thickness-normalized time

The extent of sample degradation may be quantified by any of molecular weight measurements, recorded exposure times, or calculated normalized times. Of these values, molecular weights are preferred where available because they represent a direct measurement of morphology changes within the samples. GPC test data are not available for each of the mechanical specimens tested, however, as shown in Figure 5.6. Exposure times and normalized times both appear to be similarly well correlated to molecular weight measurements as seen in Figure 5.4 and Figure 5.5, and both values are available for every mechanical test performed. Because the normalized times do not appear to improve the correlation accuracy, exposure times will be the preferred representation of degradation. Normalized time will be reserved for cases where a continuous measure of degradation is desired.

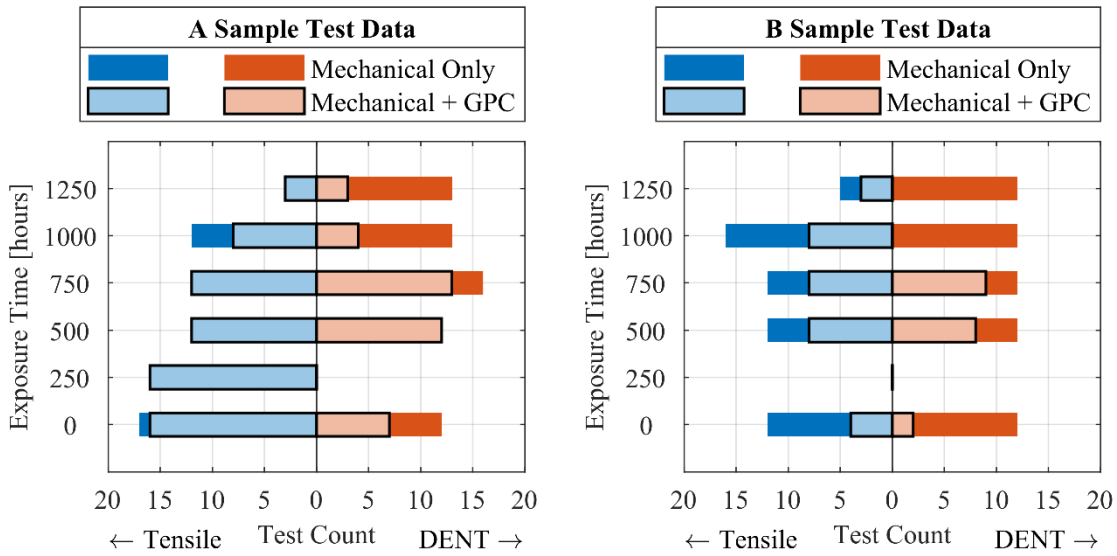

Figure 5.6: Number of mechanical tests performed with and without corresponding GPC data

5.2 Tensile Properties

Engineering stress-strain results are shown in Figure 5.7 for two example tests representing unexposed A specimens and B specimens. Elastic, yielding, and strain-hardening regions of deformation are labeled for reference. Values calculated from the load curves of each specimen are labeled, including the yield strength, the stress at the onset of failure, and the strain at failure.

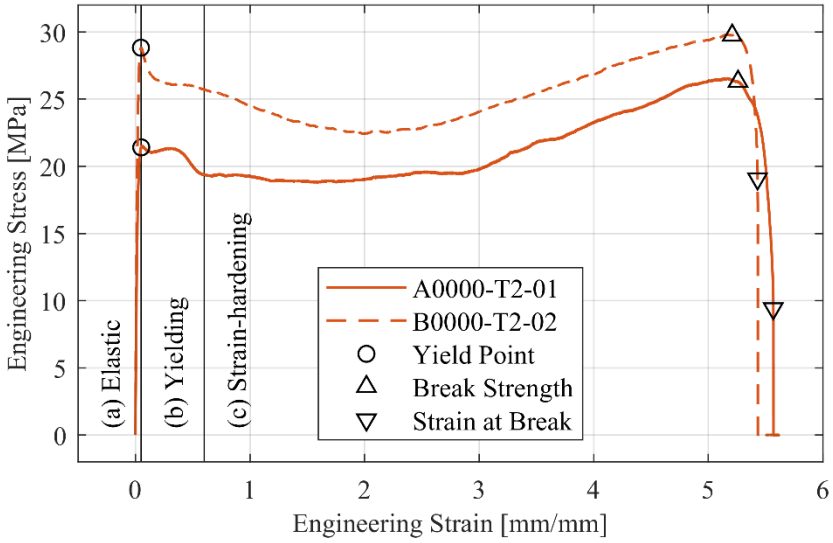

Figure 5.7: Example tensile data for A and B specimens demonstrating (a) elastic, (b) yielding, and (c) strain-hardening regions of the stress-strain curve

The initial elastic region is narrow and spans strain values up to the yield point; yield points were found at a maximum of 8% engineering strain, while some specimens exceeded 1000% engineering strain before failure. The yielding region spans strain values from the yield point up to between 60% and 80% engineering strain. Within this region, larger crystalline structures begin to break apart and to rotate towards alignment with the loading direction leading to the appearance of double-yield points [4] (e.g. the A specimen in Figure 5.7). The double-yield shape was more prevalent in A specimens

than B specimens, indicating differences in the crystalline reorientation required. This is likely due to changes in mean-crystalline orientation arising from the heat-treating process used to increase crystallinity in B specimens. The final strain-hardening region spans the remainder of the load-curve, ending at the point of failure.

The effect of strain rate on the engineering stress-strain response is demonstrated in Figure 5.8. In this figure, one example specimen is shown for each of the four strain rates applied during tensile testing. For both A and B specimens, faster strain rates correspond to larger increases in engineering stress within the strain-hardening region of the test. This indicates an increase in strain hardening as the strain rate increases.

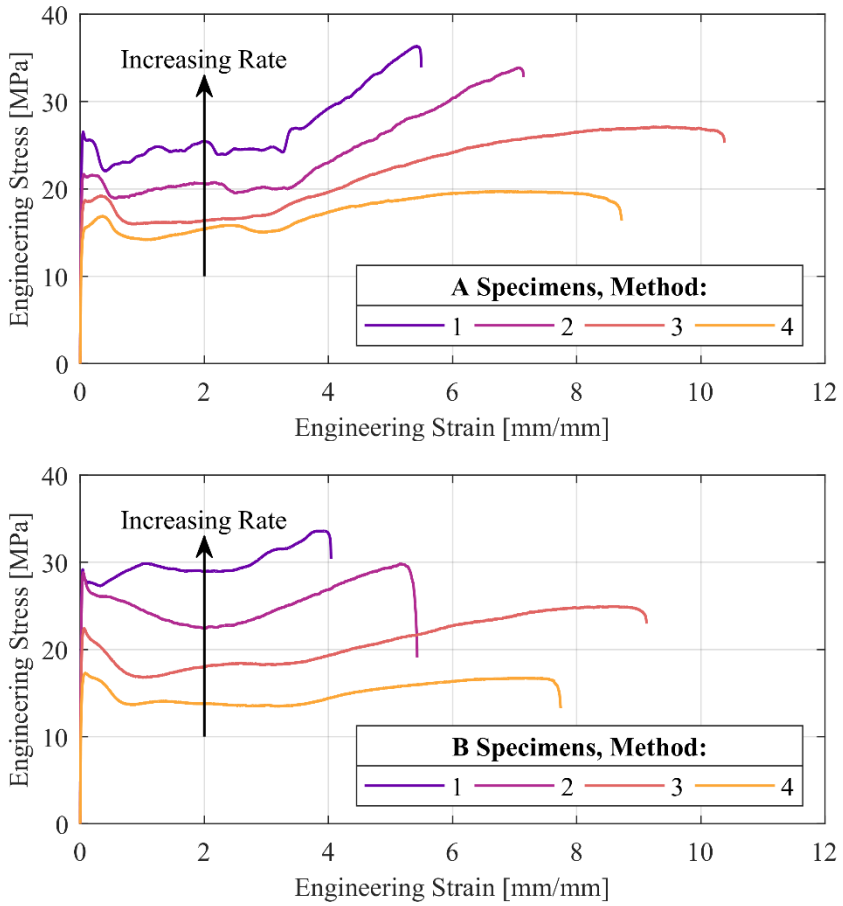

Figure 5.8: Effect of increasing strain rate on tensile data for (a) A specimens and (b) B specimens

Elastic regions for all unexposed tensile specimen load curves are shown in Figure 5.9. Observing the initial slope of these plots, the higher-crystalline B samples are stiffer than the A samples. The elastic modulus also increases with strain rate for both A and B specimens. The yield stress can be observed to increase with both strain rate and crystallinity. These trends in elasticity, yielding, and strain-hardening align with the typical expected response of semi-crystalline polymers [39,40].

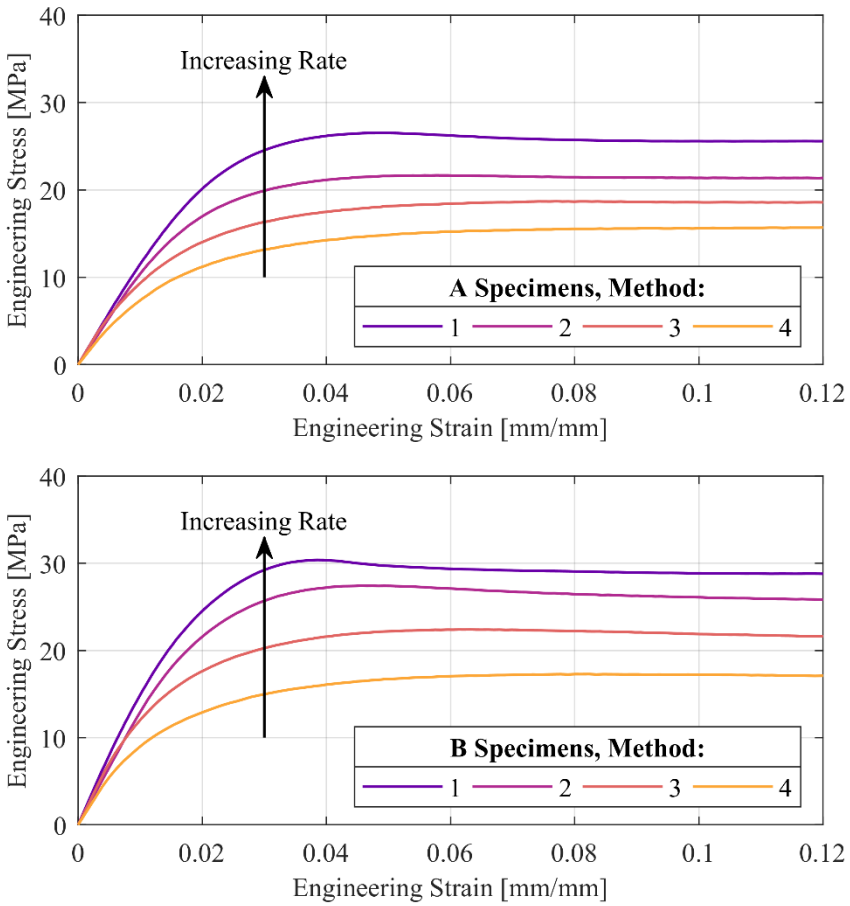

Figure 5.9: Typical engineering stress-strain response up to intial yielding of material for (a) unexposed A specimens and (b) unexposed B specimens

The effect of specimen degradation on yield strength is demonstrated in Figure 5.10, which shows values yield strength plotted against exposure time for both A and B

specimens. In this plot, each point represents the mean yield strength for all A or B specimens at a specified strain rate, with error bars representing the maximum and minimum yield strength values. The influence of strain rate remains consistent for all exposure times with faster strain rates corresponding to larger yield stress values.

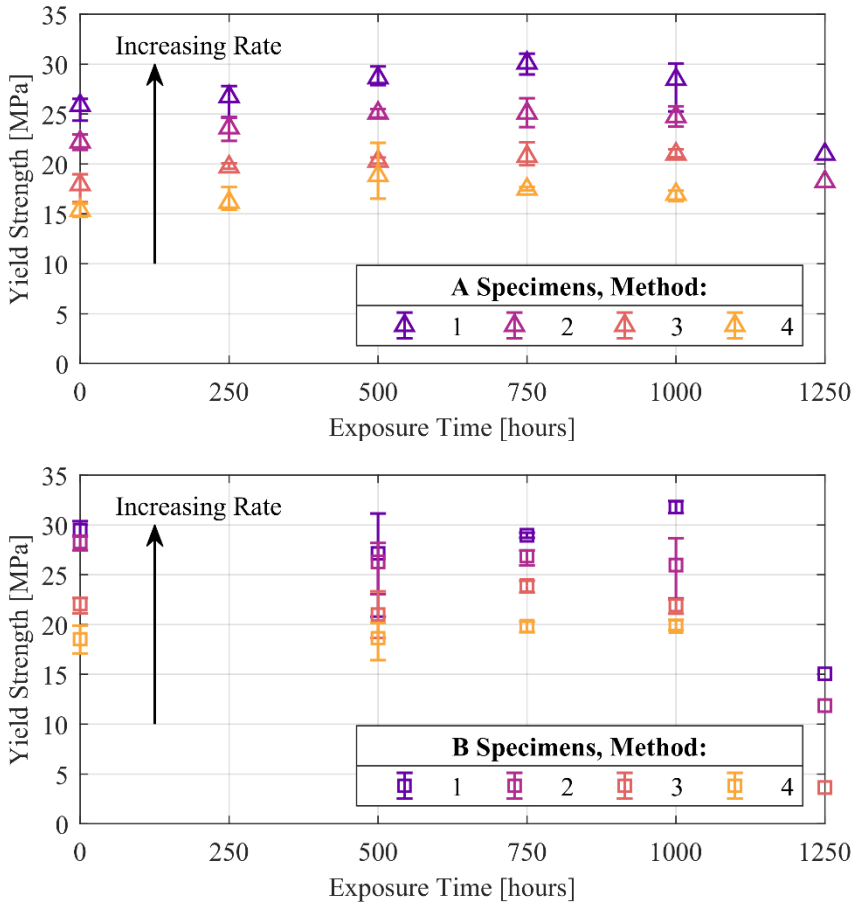

Figure 5.10: Comparison of yield strength versus strain rate at each exposure level for (a) A specimens and (b) B specimens

The yield strength generally shows a slight increase with exposure time in Figure 5.10, although the effect is less consistent than for increasing strain rates. As the exposure time increases, the crystallinity also increases for both A and B samples (see Figure 5.1). The relationship between yield strength and crystallinity is shown in Figure 5.11, where

the yield strength data of both A and B samples is plotted together against crystallinity for specimens exposed up to 1000 hours. Crystallinity points represent average values for each strain rate and exposure time, while error bars represent standard deviations. Crystallinity values are identical between strain rates because multiple specimens were cut from each material sample and these specimens were tested at separate strain rates.

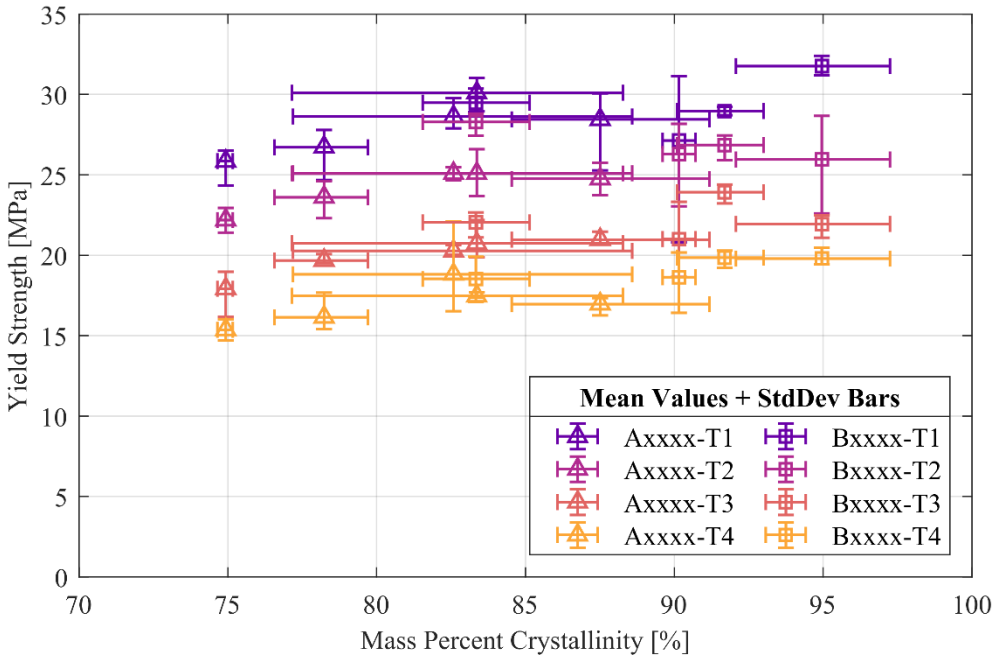

Figure 5.11: Specimen yield strength versus mass percent crystallinity

Yield strength values show an increase as the mass percent crystallinity increases in Figure 5.11. Similar yield strength values are seen from both A and B samples in the overlapping 83% to 88% crystallinity range, which represents high exposure (750-1000 hour) for A samples and low exposure (0-500 hour) for B samples. This indicates that the increase in yield strength is due to the change in crystallinity rather than degradation.

Higher percent crystallinity values indicate that more of the material is in the stiffer crystalline phase; this increased stiffness results in a higher stress before yielding

occurs and the crystalline regions begin to break and rotate [4]. Degradation results in chain scissions in the amorphous phase, but this shortening of chains has little effect prior to yield because the spherulite structures remain intact. The molecules in amorphous regions are constrained by the crystalline regions; amorphous regions maintain a similar stiffness regardless of chain length because the loosely tangled molecules cannot move enough for the shorter chain lengths to matter [41].

Failure points, represented by the strain at break and stress at break onset, are shown in Figure 5.12 for all method two specimens (with 1E-2 s^{-1} strain rate), plotted over an example engineering stress-strain curve from and unexposed sample. As exposure time increases, strain at break values decrease and break stress values roughly follow the unexposed stress-strain curve. Similar trends are shown for tests at each strain rate, with break stress values reflecting the varying strain-hardening (see Figure 5.8).

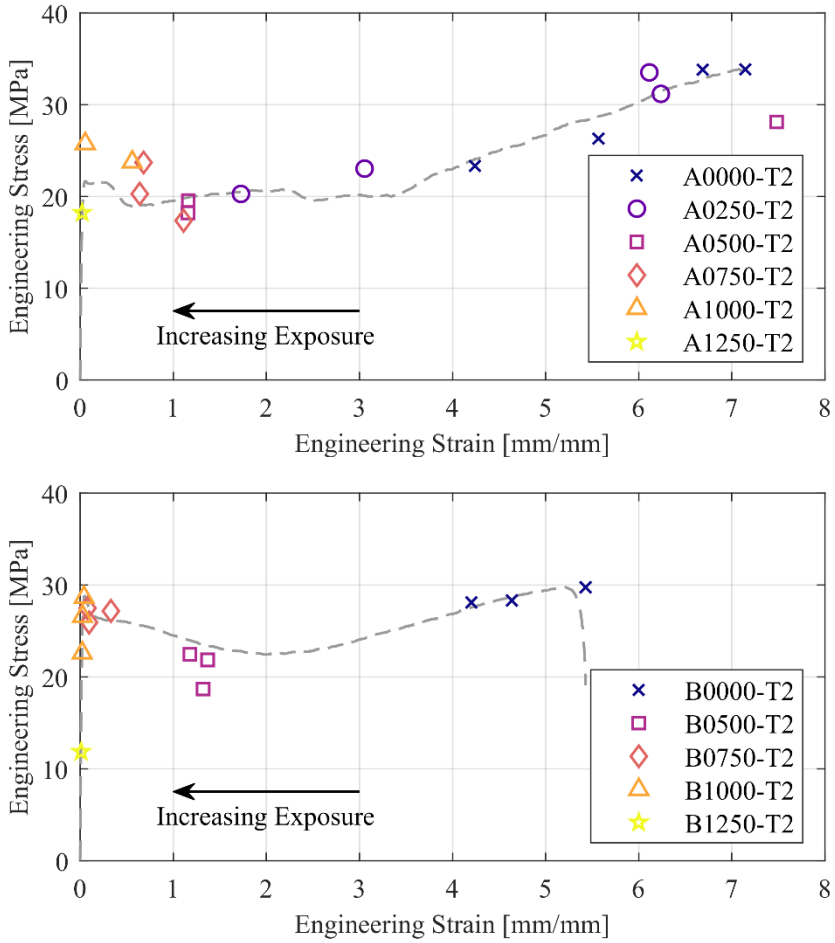

Figure 5.12: Break stress and strain point values for each exposure level and relation to unexposed stress-strain curve

Most failures occur past the yield point, after crystalline regions break apart and are held together by tie chains in the amorphous regions. As testing progresses, these amorphous regions are stretched out until the tie chains are no longer able to hold the material together [2,6]. Degradation introduces chain scissions in the amorphous regions, lowering the molecular weight (Figure 5.3) and creating fewer and shorter tie chains to hold the material together. Failure points generally follow the undegraded stress-strain curve because the deformation mechanisms remain the same, but the material fails at

lower strain values because the shorter tie chains in the amorphous regions are not able to stretch as far.

The trends shown in Figure 5.12 and ensuing discussion refer to data from method two specimens; similar results are also present for methods one, three, and four. Figure 5.13 demonstrates that strain at break values decrease with exposure time for all test methods and for both A and B specimens. Additional data for methods one, three, and four are in Appendix B.

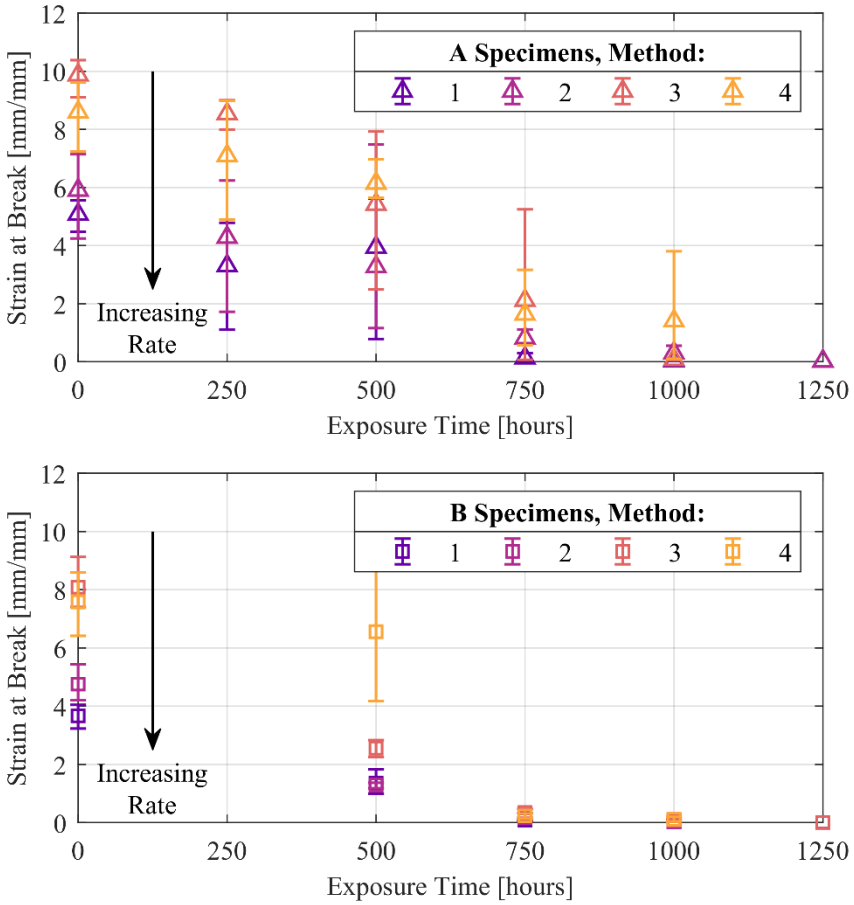

Figure 5.13: Strain at break values versus exposure level for each tensile test method for (a) A specimens and (b) B specimens

5.3 Fracture Properties

Linear regression results for the essential work of fracture method are shown in Figure 5.14 for each set of exposed samples. The terms of interest from these regressions are the slope (βw_p) and the intercept (w_e). The intercept values, known as the specific essential work, represent the energy required per unit area for the formation and propagation of a crack through the ligament cross section. The slopes of the regression lines represent the plastic work dissipated per unit volume of the plastic region (w_p) along with a factor (β) to account for the shape of the plastic region.

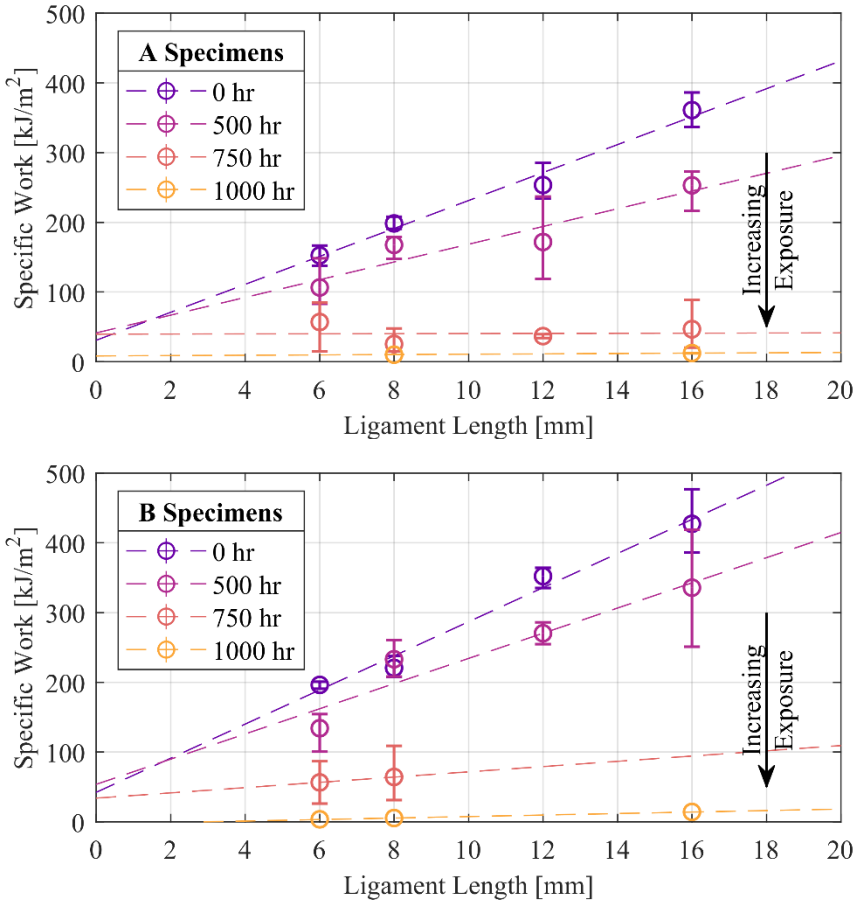

Figure 5.14: Essential work of fracture regression lines for each exposure time

Table 5.2 shows w_e and βw_p values for A and B specimens at each exposure level. An overall decrease is seen for both regression values as degradation proceeds, corresponding with specimens becoming increasingly brittle. The plastic work (slope) decreases with increasing exposure time until reaching an approximate horizontal line around 750 hours; the essential work of fracture (intercept) remains nearly constant for these exposures. Beyond 750 hours, the essential work of fracture drops toward zero, while the slope remains horizontal.

Table 5.2: Essential work of fracture regression results

	A Samples			B Samples		
Exposure [hr]	w_e **[kJ/m²]**	βw_p **[kJ/m]**	**R²**	w_e **[kJ/m²]**	βw_p **[kJ/m]**	**R²**
0	30.8 ± 40.6	20.0 ± 3.63	0.94	42.3 ± 50.1	24.5 ± 4.49	0.94
500	41.2 ± 75.8	12.7 ± 6.78	0.64	53.5 ± 91.2	18.1 ± 8.16	0.71
750	39.7 ± 51.4	0.09 ± 4.73	0.00	34.0 ± 432	3.76 ± 59.6	0.01
1000	8.52 ± 4.14	0.24 ± 0.30	0.99	-3.16 ±4.22	1.08 ± 0.39	1.00

Because βw_p corresponds primarily with plastic work, it is analogous to the portion of the stress-strain curve (Figure 5.7) beyond the yield point. As degradation proceeds, chain scission leads to fewer and shorter tie chains resulting in failure at lower strain values as seen in Figure 5.12. For DENT tests, the failure similarly occurs at lower displacement values as the exposure level is increased. While βw_p begins to decrease between 0 and 500 hours of exposure, a much larger drop is seen between 500 and 750 hours. This corresponds well with molecular weight (Figure 5.3), which also sees the largest decrease in value between 250 and 750 hours due to chain scissions.

The essential work, which corresponds with the energy required to create and propagate cracks, is more closely related with the elastic portion of the stress-strain curve

[42]. Within the elastic region, degradation and resulting chain scissions in the amorphous region have little effect (Figure 5.10); instead, the material response is dominated by the crystallinity (Figure 5.11). For DENT tests, w_e is similarly unaffected by degradation for low exposure times and sees a slight increase as crystallinity increases. The essential work remains nearly constant until the material is unable to sustain plastic deformation (as βw_p approaches zero), after which point the drop in w_e value corresponds with embrittlement of the material.

These trends in w_e can be seen in Figure 5.15, where the intercept values have been plotted for reference alongside the specific total work values for A specimens with 8mm and 16mm ligaments. These data are a subset of that in Figure 5.14 and Table 5.2, plotted against exposure time to demonstrate the effects of degradation on the total work of fracture. In all three cases, the data appear to follow a characteristic "S" shape with an initial plateau followed by a sharp decline in value before finally leveling off at an approximately zero value. The drop in total work values for 8mm and 16mm specimens appear to occur at similar times, while the decrease in intercept values shows a delay consistent with Figure 5.14. All three data sets appear to converge with one another near 750 hours, consistent with the slope term βw_p approaching zero.

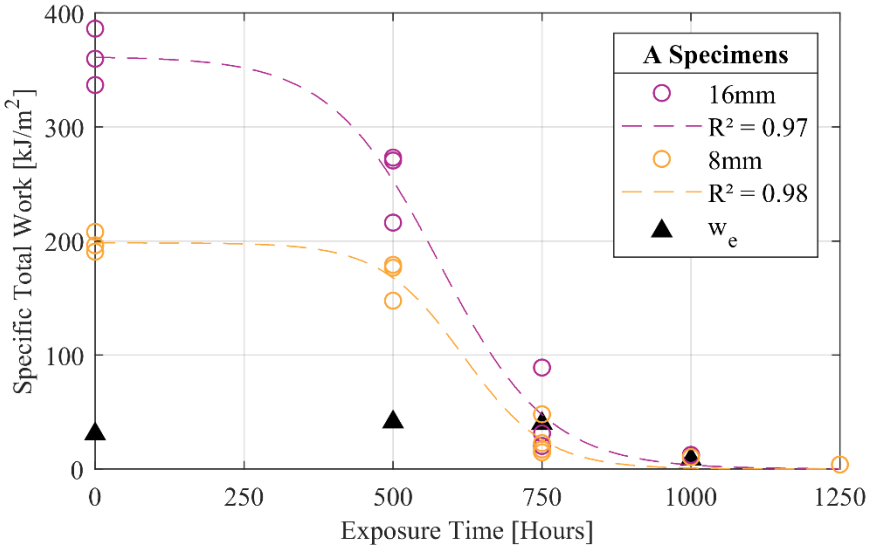

Figure 5.15: Total work of fracture versus exposure time for 8mm and 16mm ligament DENT A specimens

A modified logistic formula has been fit to the specimen data in Figure 5.15 with the form:

$$w_f(t) = \frac{w_{f,i}}{1+e^{k(t-t_c)}} \quad \textbf{(5.4)}$$

where $w_{f,i}$ represents and initial value of the work term, k is a slope term representing how quickly the work values drop, and t_c represents the inflection point at which time the values have dropped half way to zero. Although these curves have been provided primarily as a visual aid, they also appear to represent the data well as shown by their R^2 values as listed in the figure.

Exposure time is a convenient measure because it is available for every sample in this study, but it does not account for the morphological changes which lead to the increased brittleness of the specimens. A large spread in total work values is seen for 500 and 750 hours of exposure, similar to the spread in molecular weight values in Figure 5.3. This is again likely to variation in the density of chain scissions between samples, with

more degradation occurring in thinner samples. A preferred approach is to examine the total work as a function of the molecular weight, as shown in Figure 5.16. Molecular weight values decrease with chain scissions, and thus reflect changes in morphology. Regressions have been fit to the data using equation 5.4; R^2 values are lower than those in Figure 5.15 due to variation of molecular weight values.

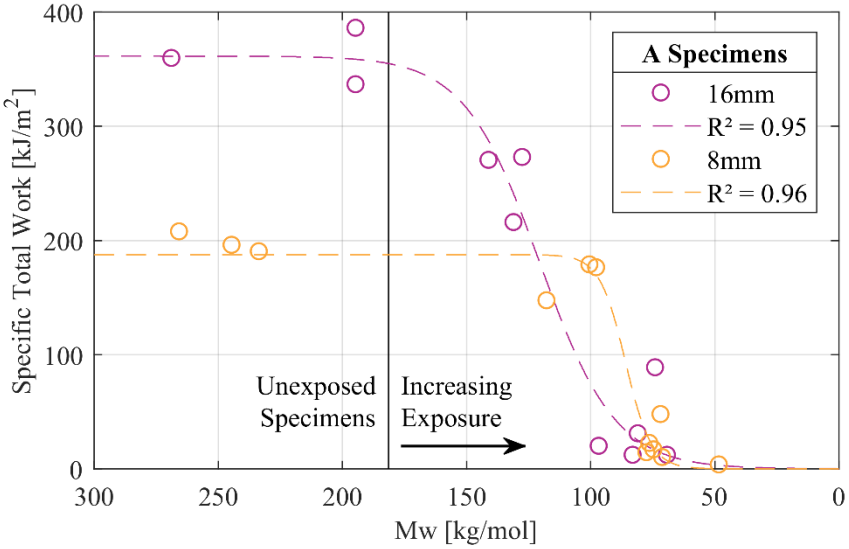

Figure 5.16: Total work of fracture versus molecular weight for 8mm and 16mm ligament DENT A specimens

An initial plateau is seen in Figure 5.16, where the total work value remains high before dropping after some threshold value of molecular weight. Recall from Figure 5.3 that the molecular weight measured for unexposed A specimens ranges between approximately 180-270 kg/mol; the minimum of these values is marked in Figure 5.16. While the delay in Figure 5.15 can be explained by the time required for diffusion and depletion of antioxidants, these factors are not reflected in the molecular weight measurement. For exposed samples (i.e. Mw<180 kg/mol), decreases in molecular weight are due to chain scission events, which may occur along any of the chains within the

amorphous region. At the onset of degradation, this includes shorter and less entangled chains which do not contribute significantly to the overall strength of the material. As degradation proceeds, the shortest chains form or move to crystalline regions [43,44]; further chain scissions become increasingly likely to affect the longer tie chains and a sharp decline in the total work to failure is seen.

Comparing total work to molecular weight requires each DENT specimen to have corresponding GPC data. The 8mm and 16mm A specimens in Figure 5.16 have been selected to represent the effects of decreasing molecular weight because GPC data are available for each of the specimens. Due to the stress and yielding criteria of the essential work method and incomplete molecular weight data (Figure 5.6), fewer data points are available for performing regression analysis on most other ligament lengths.

A compromise approach is shown in Figure 5.17, where the total work is plotted against the normalized exposure time from equation 5.3. The inclusion of the specimen thickness in this normalized time reflects the effects of diffusion time on specimen degradation but does not reflect time taken to deplete antioxidants nor the molecular weight threshold (Figure 5.16). Data once again shows a characteristic S-shape with values converging as degradation proceeds. Fitting to the sigmoid function (equation 5.4), R^2 values are lower than for exposure time and comparable to molecular weight. This indicates that diffusion is a comparable predictor of degradation to molecular weight. A further advantage of normalized time is that it may be calculated for every DENT test, providing more data points for regression analysis than molecular weight.

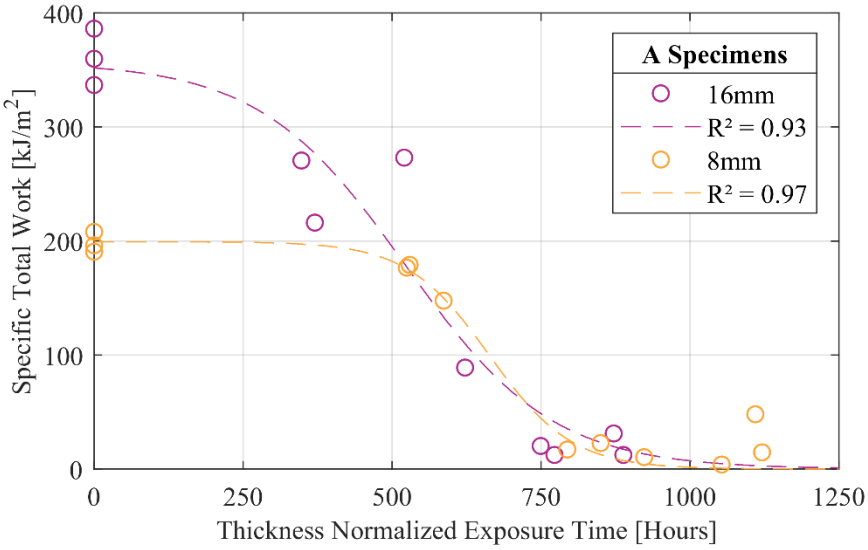

Figure 5.17: Total work of fracture versus normalized time for 8mm and 16mm ligament DENT A specimens

Several differences may be noted when comparing the total work plots for the three prediction variables: exposure time, molecular weight, and normalized time. Of these options, molecular weight is the preferred measure for predicting the material degradation, as it provides a direct relation to morphological changes in the material. Regression analysis using molecular weight is limited, however, due to incomplete GPC data. Normalized time allows data for every DENT test but reflects only the diffusion portion of the degradation processes. Exposure time does not represent morphology changes in the material but provides data for every test and the highest R^2 values of the three predictors.

Regression results from each of the three prediction variables demonstrate that the sigmoid function of equation 5.4 adequately describes changes in the total work as the specimens degrade. The results are valid only for data sets sharing constant ligament lengths, however, and do not reflect the w_e or βw_p material properties from the essential

work method. The essential work method is similarly limited, requiring data sets which share a constant prediction variable. The method is easily applied to exposure time, where linear regression can be performed on data at each discrete time value (0, 500, 750, ect. hours). Molecular weight and normalized time values are unique to each specimen; data cannot be "binned" for linear regression in the same way as for exposure time.

A new model is desired which can accommodate this continuous data and combine the benefits of both the sigmoid and essential work models. This is accomplished by performing a non-linear regression using a combined model:

$$w_{EWF}(l) = w_e + \beta w_p l \tag{5.5}$$

$$w_{sig}(t) = \left(1 + e^{k(t-t_c)}\right)^{-1} \tag{5.6}$$

$$w_f(l,t) = w_{EWF}(l) * w_{sig}(t) = \left(w_{e,i} + \beta w_{p,i} l\right) * \left(1 + e^{k(t-t_c)}\right)^{-1} \tag{5.7}$$

where the term $w_{EWF}(l)$ is linear in terms of ligament length, l, and follows the form of the essential work method. The term $w_{sig}(t)$ mirrors the sigmoidal function of equation 5.4 with respect to t, which may represent any prediction variable including the exposure time, normalized time, or molecular weight. The terms $w_{e,i}$, $\beta w_{p,i}$, k, and t_c are determined by regression and represent similar values to the original models. Because this model is dependent on both the ligament length and the prediction variable, all data may be used for regression analysis without the requirement for binning. This allows for continuous data (e.g. molecular weight) to be fit and a larger number of data points than if the data were binned by individual ligament lengths or exposure times.

Time-based predictor values, which begin with an initial predictor value of $t_i = 0$ and increase with exposure, produce positive k values. This results in sigmoid functions

which drop as t increases. For a given molecular weight, t_i is large and decreases with exposure; this produces a negative k value and a sigmoid which drops as t decreases. For both cases, the sigmoid functions drop as degradation proceeds. Further, initial values of the predictor variable (t_i) result in the term $w_{sig}(t_i) \cong 1$ for all predictor variables, which results in:

$$w_f(l, t_i) \cong w_{EWF}(l) = w_{e,i} + \beta w_{p,i} l \quad \textbf{(5.8)}$$

This demonstrates that $w_{e,i}$ and $\beta w_{p,i}$ are analogous to the essential work and plastic work terms from the essential work method, as applied to the unexposed specimens. The material properties may also be determined as a function of the predictor variable by rearranging equation 5.7:

$$w_e(t) = w_{e,i} * \left(1 + e^{k(t-t_c)}\right)^{-1} \quad \textbf{(5.9)}$$

$$\beta w_p(t) = \beta w_{p,i} * \left(1 + e^{k(t-t_c)}\right)^{-1} \quad \textbf{(5.10)}$$

Figure 5.18 demonstrates the results of applying this model to the normalized time data for both A and B specimens. Non-linear regression was performed on the data in MATLAB, resulting in the surface fit and R^2 values shown. Although the R^2 values are low (recall from Figure 5.16 and Figure 5.17 that this results from variation in the predictor values), the figure demonstrates important qualities of this new model.

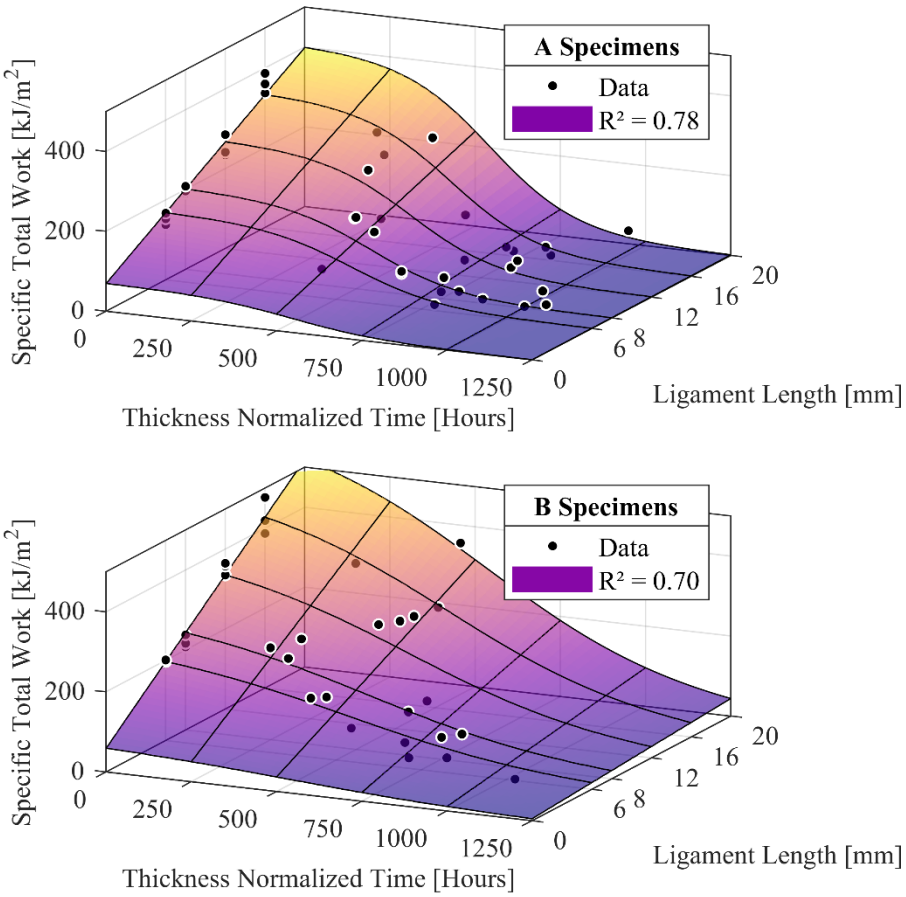

Figure 5.18: Total work of fracture versus thickness normalized time with surface regression for (a) A specimens and (b) B specimens

In Figure 5.18, the surface grid is laid out with lines at each ligament length and exposure time used in this study. For each constant-ligament length line, the model produces a sigmoid curve which drops as degradation proceeds. Additionally, a linear response can be seen for each constant-time line, consistent with the assumptions of the essential work of fracture method. This linear response demonstrates the chief advantage of this new model: the model may be applied to data with unique ("un-binned") predictor values. In this dataset, the traditional essential work of fracture method could only be applied to the unexposed samples, where $t_{norm} = 0$. Because t_{norm} values are unique for

each exposed data point, there are no other shared normalized time values which would allow for a linear regression to be applied. The surface model allows a fit to be performed on all data without requiring that datapoints share t_{norm} values. Similarly, the model will allow for morphological measurements such as molecular weight to be used as predictor values, which will be unique to each specimen.

The model from equation 5.7 was also applied to A and B specimen DENT data using the exposure time as a predictor value, with the resulting surface fits and R^2 values shown in Figure 5.19. The R^2 values, both 0.93, show a reasonable fit to the exposure time data and are greatly improved as compared to the normalized time data. Once again, linear results are found for each constant-time line in the figure. These results are analogous to those seen in Figure 5.14, with the major difference being that the surface fit model considers data from all exposure times. This is advantageous for series with limited data; one such example can be seen for the 750-hour B specimens, which did not include data for 12- or 16-mm ligaments length specimens due to the yield-before-fracture criterion. The surface fit provides an improved estimate of the w_e and βw_p properties compared to the linear regression results obtained from only the 6- and 8-mm ligament length specimens. A further benefit of the surface model is that it estimates material properties without measured specimens (e.g. for 250 hours). Comparison plots between the exposure-time surface fit results and linear regression results of the standard EWF method are available in Appendix section C.3. Resulting model parameters for each surface regression in Figure 5.18 and Figure 5.19 are summarized in Table 5.3.

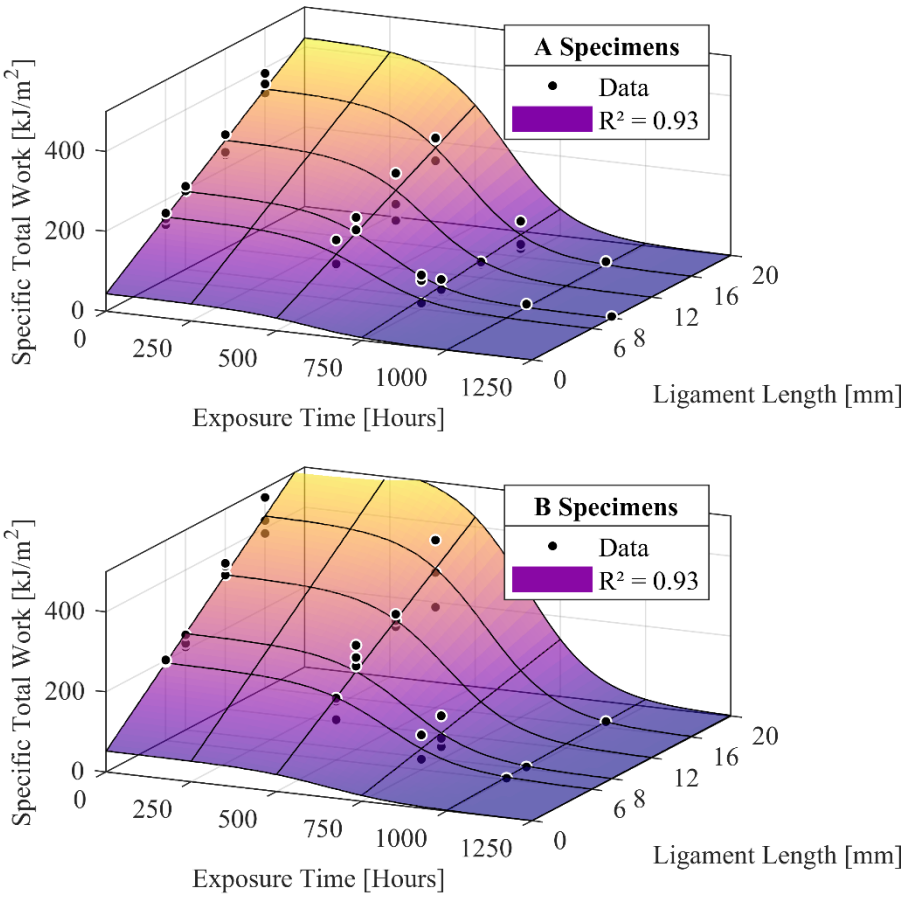

Figure 5.19: Total work of fracture versus exposure time with surface regression for (a) A specimens and (b) B specimens

Table 5.3: Regression results for essential work of fracture surface model

Predictor Variable	**Samples**	$w_{e,i}$ [kJ/m²]	$\beta w_{p,i}$ [kJ/m]	k [hrs^{-1}]	t_c [hrs]	R²
Exposure Time	A	44	19	0.010	589	0.93
Normalized Time	A	70	17	0.007	577	0.78
Exposure Time	B	52	24	0.010	648	0.93
Normalized Time	B	68	26	0.003	568	0.70

Chapter 6: Conclusion

6.1 Summary of Methods

In this study, the effect of degradation on mechanical properties was examined for HDPE exposed to a chlorinated water environment. To accomplish this, material specimens were created with varying crystallinities and levels of exposure. Test specimens were prepared from these samples and tested mechanically to determine their tensile and fracture properties. Chemical tests were also performed on the material samples to determine their morphological characteristics.

Material creation began by extruding HDPE into a thin film from which material samples were cut. Sample thicknesses ranged between 0.037 and 0.109 mm, with a mean thickness value of 0.063 mm. These samples were then split into two series, designated "A" and "B" samples. B samples were heat-treated in an oven to increase their crystallinity while A samples were used as-extruded. Finally, varying levels of degradation were produced by exposing the material samples in a chlorinated waterbath with an oxidation reduction potential (ORP) of 825 mV for up to 1250 hours.

Mechanical test specimens were prepared from each of these materials (e.g. each combination of A or B sample and hours-of-exposure) to examine tensile and fracture characteristics. Tensile testing was performed on ASTM D1708 microtensile specimens for four different strain rates. The resulting engineering stress-strain curves provided yielding and break data for each specimen. Fracture properties were determined by applying the essential work of fracture (EWF) method to obtain the essential work of

fracture and plastic work factor for each material. Data for the EWF method were obtained from notched test specimens with ligament lengths between 6 and 16 mm.

Morphological characteristics examined for each of the materials included crystallinity and molecular weight. Crystallinity was measured with differential scanning calorimetry (DSC), with each specimen prepared by combining material from multiple matching material samples. This provided an aggregate crystallinity for each of the material types rather than crystallinity for each specific sample. Molecular weight was measured by performing gel permeation chromatography (GPC) testing on specimens prepared from individual material samples which allowed measures to be correlated to specific mechanical test specimens.

6.2 Findings and Observations

The proposed mechanism for HPDE degradation begins with oxidation reactions which lead to chain scission within amorphous regions of the polymer and subsequent migration of the shortened chains into crystalline regions. This impacts the mechanical properties of the material by leading to embrittlement due to fewer tie chains and less chain entanglement within amorphous regions. This study has shown the effectiveness of the methodology for degrading HDPE samples in a chlorinated water bath, as well as examined resulting losses in mechanical properties and changes in morphology. As specimen exposure time has increased, decreases have been recorded for tensile strain at break values, essential work of fracture values, and molecular weight measurements. Mass percent crystallinity has conversely shown an increase in values with increased exposure times.

The reliability of the waterbath and the selection of appropriate material sample thicknesses have been identified as critical to the effectiveness of the degradation method. The waterbath is expected to perform consistently over extended lengths of time; in this study, material samples required exposures up to 1250 hours or approximately 52 days. Appropriate sample thicknesses are also crucial to achieving degradation due to the slow diffusion of the free radicals required to initiate the degradation reactions. For thick samples, reactions begin at the surface of the material, but deeper portions of the material remain untouched. The material thickness, waterbath conditions, and range of exposure times used in this study have proven effective by producing degradation measured by both molecular weight and crystallinity changes.

For the lower crystallinity A samples used in this study, molecular weight values decreased to 79% and 49% of their original values after 250 and 500 hours of exposure respectively. After 1250 hours, molecular weight decreased to 24% of its original value. The decrease in molecular weight demonstrates shortened polymer molecules due to chain scission events. The largest decrease in molecular weight values occurred between 250 hours and 500 hours of exposure. This delay in degradation is due to time required for the depletion of antioxidants within the HDPE blend. A similar delay was also noted for the higher crystallinity B samples, for which molecular weight values decreased to 69% and 46% of their values after 500 and 750 hours of exposure respectively. Molecular weight decreased to 32% of its original value after 1250 hours of exposure for B samples. After the maximum decrease in molecular weight, values continued to decrease at slower rates for both A and B samples demonstrating fewer chains available for chain scission due to migration from amorphous to crystalline regions. This migration is evidenced by

changes in mass percent crystallinity values, which increased at a relatively constant rate as the materials were exposed, with similar increases of 13% and 14% over unexposed samples for 1250-hour A and B samples respectively.

Tensile test results demonstrate successful degradation and transition to brittle behavior through decreases in the values for tensile test break points for exposed specimens. As specimen exposure time increased, tensile test strain at break values decreased. After 750 hours exposure, strain at break values for A and B specimens decreased to 14% and 3% of the values measured for unexposed specimens tested at the same strain rates. At 1250 hours of exposure, most specimens were too brittle to successfully test as they would fracture before any load could be applied. As specimen strain at break values decreased, engineering stress at break values approximately followed the engineering stress-strain curve of unexposed samples (see Appendix B).

Following the essential work of fracture method, both the essential and plastic work terms approached values of zero for specimens exposed for 1000 hours and above, indicating that the material had transitioned to brittle behavior. The specific total work of fracture dropped off sharply between 500 and 750 hours of exposure for both A and B samples, corresponding with this embrittlement. This also corresponded with the largest drop measured in molecular weight, supporting the hypothesis that mechanical embrittlement is related to chain scission events.

Application of a sigmoidal model to relate the specific total work to molecular weight showed promising results, with R^2 values of 0.96 and 0.95 for A specimens with 8 mm and 16 mm ligament lengths, respectively. An initial plateau was also observed in these models, where specific total work values remained high before dropping after a

threshold molecular weight value. It is proposed that this is due to the initial presence of shorter chains within the amorphous region (i.e. available for chain scission) which do not contribute significantly to the mechanical strength of the material. For longer exposure times, these short chains will migrate into the crystalline regions leaving only the longer entangled chains (which contribute to the mechanical strength) in the amorphous region for chain scissions.

6.3 Recommendations and Future Work

A further model was applied to the double edge notch tensile (DENT) data to fit the specific total work to a surface determined by both ligament lengths (a linear relationship, per the essential work of fracture method) and exposure time (using a sigmoidal relationship). This model also showed promising results with data for A and B samples both producing R^2 values of 0.93. The fit coefficient t_c in this model represents the inflection point for the sigmoidal shape and the time when total work values can be expected to be 50% of their original value. Values of approximately 590 hours and 650 hours were found for A and B specimens, respectively. The longer time for B specimens corresponds with slower degradation due to their higher crystallinity (i.e. B specimens contained less amorphous region for diffusion and chain scission).

A chief advantage of this new surface model is the ability to select predictor variables, including measures of morphology, to determine when the material will undergo a brittle transition. Sigmoidal fits have been demonstrated for exposure time, thickness-normalized exposure time, and molecular weight. While the essential work method may only be applied to 'like' materials (e.g. 500-hour A specimens only), the

surface fit may be applied with continuous predictor values such as molecular weight (which may vary between 500-hour specimens). This is especially advantageous in that it allows the mechanical properties to be predicted based on morphological measures, which can be used to correlate lab results to expected field results.

This study has shown that expedited degradation may be completed in a lab environment using a waterbath apparatus. The speed of this degradation may vary depending on experimental parameters such as the thickness of material samples or the bath ORP and temperature. While brittle transitions have been observed between 500 and 750 hours in this study, it is expected that timescales will vary as experimental setups vary. Exposure time also does not directly relate to field results, where materials will be thicker and are likely to see much slower oxidation. Due to the increased speed of degradation in the waterbath, however, the lab environment becomes practical for determining the dependence of the material's brittle transition on its morphology. By applying the surface model, threshold molecular weight values may be determined to predict the onset of embrittlement. By determining the timescales for morphological changes in field applications, this lab-determined threshold may then be applied to predict expected lifetimes.

While molecular weight has been demonstrated to be a useful predictor for the transition to brittle mechanical behavior, other morphological measures exist which deserve future consideration. Comparing the t_c values demonstrates that the higher mass percent crystallinity of B samples corresponds with slower degradation. Similarly, both A and B samples experienced a steady rise in crystallinity as exposure proceeded. This crystallinity was partially enhanced by the elevated temperatures within the bath;

materials in field applications will likely be exposed to different temperatures and the rate of crystallization will likely differ. The HPDE used in this study was also very linear in structure. Materials with crosslinked or branched chains would also show a different rate of crystallization; entanglement between the more complex chains would also likely result in a different rate of mechanical degradation. Models incorporating measures of crystallinity or chain structure would be useful in a more general prediction model for the onset of embrittlement.

Future work may also include examining the effects of variance in molecular weight measurements. GPC data for unexposed A and B samples provided mean molecular weights of 233 and 215 kg/mol with standard deviations of 30 and 34 kg/mol, respectively. Some of this spread may be attributed to the study methodology including the efficacy of the waterbath and the number and thickness of samples. Variance is also expected due to the GPC measurements themselves. An understanding should be developed as to this expected level of measurement variance and the implications on the accuracy of molecular weight embrittlement thresholds when predicting material lifetime. If a large standard deviation for the GPC measurements is inevitable, then a lower accuracy should be expected for the predicted threshold. This would result in the use of a lower percentage drop of molecular weight to maintain a conservative estimate of embrittlement onset.

To improve estimates for the onset of brittle behavior, material sample exposure times should be carefully selected. In the present study, samples exposed for 1000 and 1250 hours provided very little mechanical data due to being very brittle. Exposure times which would provide the most useful data would be those during and leading up to the

narrow window when embrittlement occurs (500-750 hours in this study). Data within this window have shown a wide variance; increasing the number of samples in this window would serve to decrease the standard deviations of results obtained. Data preceding this window would be provide more resolution to determine the shape of the sigmoidal relationships at the onset of embrittlement as well as allow a more accurate determination of the time when embrittlement begins.

Improvements to the study methodology during material creation and waterbath exposure may also result in improved measurement uniformity. When extruding samples, consistent material thickness should be maintained as closely as possible. The essential work of fracture (EWF) method is intended to be applied to specimens of uniform thickness and relies on testing under plain stress conditions; improved uniformity of specimen thickness should increase the accuracy of EWF results and (because it is an extension of the EWF method) results obtained from the surface fit model. Uniformity of waterbath exposure may be increased by ensuring that conditions are consistent throughout the bath environment. Temperature gradients may develop in the bath and specimen positioning may result in exposure to varying concentrations of chlorine. Although the impacts may be small (chlorine is able to diffuse throughout the waterbath much more quickly than into the plastic samples), any improvements in environmental consistency should result in more uniform exposed samples. Efforts should be made to ensure that waterbath flow enables proper mixing within the bath and that specimens are positioned to avoid ‘dead zones’ with little to no flow.

Future work on the waterbath may also enable further improvements to reliability. Minimizing sources of electrical ‘noise’ in the recorded measurements would improve

data collection and help to minimize false alarms when the control software sees an apparent ‘spike’ in the data. Currently, bath parameters are available for remote viewing via emails sent every 20 minutes containing snapshots of the current conditions. A more useful approach which could be investigated would be to export a continuous set of data to an online service such as google drive; this would aid in troubleshooting any bath problems by providing a full log of bath data. Finally, implementing a proper PID control to vary the volume of chlorine solution added to the bath would serve to level out the current oscillations seen in the chlorine concentration, which are due to the solution currently being added in discrete volumes. Improvements to the controller code would only make a minor difference, however, due to the differences between diffusion rates throughout the bath and into the samples.

Bibliography

[1] Gill, T. S., Knapp, R. J., Bradley, S. W., and Bradley, W. L., 1998, "Long Term Durability of Crosslinked Polyethylene Tubing Used in Chlorinated Hot Water Systems," ANTEC 1998 Plastics: Plastics on My Mind, **3**, pp. 1–5.

[2] Callister, W. D., and Rethwisch, D. G., 2009, *Materials Science and Engineering: An Introduction*, John Wiley and Sons.

[3] Dongyuan, L., Lianshui, Z., Yaqi, W., and Wenxiu, C., 1987, "The Effect of Radiation Cross-Linking on the Mechanical Properties of Polyethylene Sheets," International Journal of Radiation Applications and Instrumentation, **29**(3), pp. 175–177.

[4] Kida, T., Oku, T., Hiejima, Y., and Nitta, K.-H., 2015, "Deformation Mechanism of High-Density Polyethylene Probed by in Situ Raman Spectroscopy," Polymer, **58**, pp. 88–95.

[5] Michaeli, W., and Glißmann, M., 2000, "Investigation and Measurement of the True Stress/Strain Behaviour of Semi-crystalline Thermoplastics," Macromolecular Materials and Engineering, **284**–**285**(1), pp. 19–24.

[6] Nitta, K. H., 1999, "A Molecular Theory of Stress-Strain Relationship of Spherulitic Materials," Computational and Theoretical Polymer Science, **9**(1), pp. 19–26.

[7] Kida, T., Hiejima, Y., and Nitta, K. H., 2016, "Molecular Orientation Behavior of Isotactic Polypropylene under Uniaxial Stretching by Rheo-Raman Spectroscopy," Express Polymer Letters, **10**(8), pp. 701–709.

[8] Mikdam, A., Colin, X., Minard, G., Billon, N., and Maurin, R., 2017, "A Kinetic Model for Predicting the Oxidative Degradation of Additive Free Polyethylene in Bleach Desinfected Water," Polymer Degradation and Stability, **146**(Supplement

C), pp. 78–94.

[9] Web, C. R. on the, “Degradation of Polymers” [Online]. Available: http://polymerdatabase.com/polymer chemistry/Thermal Degradation.html. [Accessed: 11-Dec-2019].

[10] Hsuan, Y. G., and Koerner, R. M., 1998, “Antioxidant Depletion Lifetime in High Density Polyethylene Geomembranes,” Journal of Geotechnical and Geoenvironmental Engineering, **124**(6), pp. 532–541.

[11] Andrady, A. L., Pegram, J. E., and Tropsha, Y., 1993, “Changes in Carbonyl Index and Average Molecular Weight on Embrittlement of Enhanced-Photodegradable Polyethylenes,” Journal of environmental polymer degradation, **1**(3), pp. 171–179.

[12] Castillo Montes, J., Cadoux, D., Creus, J., Touzain, S., Gaudichet-Maurin, E., and Correc, O., 2012, “Ageing of Polyethylene at Raised Temperature in Contact with Chlorinated Sanitary Hot Water. Part I – Chemical Aspects,” Polymer Degradation and Stability, **97**(2), pp. 149–157.

[13] Choi, B.-H., Zhou, Z., Chudnovsky, A., Stivala, S. S., Sehanobish, K., and Bosnyak, C. P., 2005, “Fracture Initiation Associated with Chemical Degradation: Observation and Modeling,” International Journal of Solids and Structures, **42**(2), pp. 681–695.

[14] Colin, X., Audouin, L., Verdu, J., Rozental-Evesque, M., Rabaud, B., Martin, F., and Bourgine, F., 2009, “Aging of Polyethylene Pipes Transporting Drinking Water Disinfected by Chlorine Dioxide. I. Chemical Aspects,” Polymer Engineering & Science, **49**(7), pp. 1429–1437.

[15] Colin, X., Audouin, L., Verdu, J., Rozental-Evesque, M., Rabaud, B., Martin, F., and Bourgine, F., 2009, “Aging of Polyethylene Pipes Transporting Drinking Water Disinfected by Chlorine Dioxide. Part II—Lifetime Prediction,” Polymer Engineering & Science, **49**(8), pp. 1642–1652.

[16] Deveci, S., Antony, N., and Eryigit, B., 2018, “Effect of Carbon Black Distribution on the Properties of Polyethylene Pipes - Part 1: Degradation of Post Yield Mechanical Properties and Fracture Surface Analyses,” Polymer Degradation and Stability, **148**, pp. 75–85.

[17] Fayolle, B., Richaud, E., Colin, X., and Verdu, J., 2008, “Review: Degradation-Induced Embrittlement in Semi-Crystalline Polymers Having Their Amorphous Phase in Rubbery State,” Journal of Materials Science, **43**(22), pp. 6999–7012.

[18] Fayolle, B., Colin, X., Audouin, L., and Verdu, J., 2007, “Mechanism of Degradation Induced Embrittlement in Polyethylene,” Polymer Degradation and Stability, **92**(2), pp. 231–238.

[19] Formela, K., Wołosiak, M., Klein, M., and Wang, S., 2016, “Characterization of Volatile Compounds, Structural, Thermal and Physico-Mechanical Properties of Cross-Linked Polyethylene Foams Degraded Thermo-Mechanically at Variable Times,” Polymer Degradation and Stability, **134**, pp. 383–393.

[20] François-Heude, A., Richaud, E., Desnoux, E., and Colin, X., 2015, “A General Kinetic Model for the Photothermal Oxidation of Polypropylene,” Journal of Photochemistry and Photobiology A: Chemistry, **296**, pp. 48–65.

[21] Ge, H., Singh, G., and Mantell, S. C., 2012, “Fracture Behavior of Degraded Polyethylene Thin Films for Solar Thermal Applications,” *Energy Procedia*, pp. 783–792.

[22] Gulmine, J. V., and Akcelrud, L., 2006, “Correlations between Structure and Accelerated Artificial Ageing of XLPE,” European Polymer Journal, **42**(3), pp. 553–562.

[23] Hinsken, H., Moss, S., Pauquet, J.-R., and Zweifel, H., 1991, “Degradation of Polyolefins during Melt Processing,” Polymer Degradation and Stability, **34**(1–3), pp. 279–293.

[24] Langlois, V., Audouin, L., Courtois, P., and Verdu, J., 1993, “Change of Mechanical Properties of Crosslinked Polyethylene during Its Thermo-oxidative Aging,” Die Angewandte Makromolekulare Chemie, **208**(1), pp. 47–64.

[25] Matsumoto, S., 1983, “Behavior of Antioxidant in Polyethylene,” Journal of polymer science. Part A-1, Polymer chemistry, **21**(2), pp. 557–564.

[26] Mitroka, S. M., Smiley, T. D., Tanko, J. M., and Dietrich, A. M., 2013, “Reaction Mechanism for Oxidation and Degradation of High Density Polyethylene in Chlorinated Water,” Polymer Degradation and Stability, **98**(7), pp. 1369–1377.

[27] Yu, W., Reitberger, T., Hjertberg, T., Oderkerk, J., Costa, F. R., and Gedde, U. W., 2012, “Antioxidant Consumption in Squalane and Polyethylene Exposed to Chlorinated Aqueous Media,” Polymer Degradation and Stability, **97**(11), pp. 2370–2377.

[28] Yu, W., Azhdar, B., Andersson, D., Reitberger, T., Hassinen, J., Hjertberg, T., and Gedde, U. W., 2011, “Deterioration of Polyethylene Pipes Exposed to Water Containing Chlorine Dioxide,” Polymer Degradation and Stability, **96**(5), pp. 790–797.

[29] Kettle, A. J., Albrett, A. M., Chapman, A. L., Dickerhof, N., Forbes, L. V., Khalilova, I., and Turner, R., 2014, “Measuring Chlorine Bleach in Biology and Medicine,” Biochimica et Biophysica Acta - General Subjects, **1840**(2), pp. 781–793.

[30] ASTM Standard D1708-13, 2013, “Standard Test Method for Tensile Properties of Plastics by Use of Microtensile Specimens,” ASTM International, West Conshohocken, PA.

[31] ASTM Standard D882-12, 2012, “Standard Test Method for Tensile Properties of Thin Plastic Sheeting,” ASTM International, West Conshohocken, PA.

[32] ASTM Standard D638-14, 2014, “Standard Test Method for Tensile Properties of

Plastics," ASTM International, West Conshohocken, PA.

[33] Blaber, J., Adair, B., and Antoniou, A., 2015, "Ncorr: Open-Source 2D Digital Image Correlation Matlab Software," Experimental Mechanics, **55**(6), pp. 1105–1122.

[34] Clutton, E., 2001, "Essential Work of Fracture," European Structural Integrity Society, **28**(C), pp. 177–195.

[35] Mai, Y. W., and Cotterell, B., 1984, "The Essential Work of Fracture for Tearing of Ductile Metals," International Journal of Fracture, **24**(3), pp. 229–236.

[36] Bárány, T., Czigány, T., and Karger-Kocsis, J., 2010, "Application of the Essential Work of Fracture (EWF) Concept for Polymers, Related Blends and Composites: A Review," Progress in Polymer Science, **35**(10), pp. 1257–1287.

[37] Hill, R., 1952, "On Discontinuous Plastic States, with Special Reference to Localized Necking in Thin Sheets," Journal of the Mechanics and Physics of Solids, **1**(1), pp. 19–30.

[38] Crank, J., 1975, *The Mathematics of Diffusion*, Oxford Univ. Press, London.

[39] Schrauwen, B. A. G., Janssen, R. P. M., Govaert, L. E., and Meijer, H. E. H., 2004, "Intrinsic Deformation Behavior of Semicrystalline Polymers," Macromolecules, **37**(16), pp. 6069–6078.

[40] Kurelec, L., Teeuwen, M., Schoffeleers, H., and Deblieck, R., 2005, "Strain Hardening Modulus as a Measure of Environmental Stress Crack Resistance of High Density Polyethylene," Polymer, **46**(17), pp. 6369–6379.

[41] Kang, J., Yuan, S., Hong, Y.-L., Chen, W., Kamimura, A., Otsubo, A., and Miyoshi, T., 2016, "Unfolding of Isotactic Polypropylene under Uniaxial Stretching," ACS Macro Letters, **5**(1), pp. 65–68.

[42] Wu, J., and Mai, Y., 1996, “The Essential Fracture Work Concept for Toughness Measurement of Ductile Polymers,” Polymer Engineering & Science, **36**(18), pp. 2275–2288.

[43] Oswald, H. J., and Turi, E., 1965, “The Deterioration of Polypropylene by Oxidative Degradation,” Polymer Engineering & Science, **5**(3), pp. 152–158.

[44] Kagiya, T., Nishimoto, S., Watanabe, Y., and Kato, M., 1985, “Importance of the Amorphous Fraction of Polypropylene in the Resistance to Radiation-Induced Oxidative Degradation,” Polymer Degradation and Stability, **12**(3), pp. 261–275.

[45] Dong, Y. L., and Pan, B., 2017, “A Review of Speckle Pattern Fabrication and Assessment for Digital Image Correlation,” Experimental Mechanics, **57**(8), pp. 1161–1181.

Appendix A: Overview of Ncorr Algorithms

The essential goal of digital image correlation (DIC) is to locate points on a specimen as they move through a series of images. Once located, the positions of these points are compared to an initial reference image and their displacements are calculated. By following multiple points, these displacements can be used to calculate strain values. Ncorr has been utilized for this study, which contains algorithms for computing displacement fields for a series of images. A simple overview of the methods used by this code is provided here.

To locate a point from the initial image in subsequent images, a small region surrounding that point in the image will be compared to regions in the following images; these regions are known as subsets. Figure A.1 shows three example subsets taken from two images of a tensile test specimen: one from a reference image at the start of the test and two from a 'current' image taken during the test. For this example, the DIC algorithms must then determine which of the 'current' subsets are the best match to the reference to determine how far the original material point has displaced.

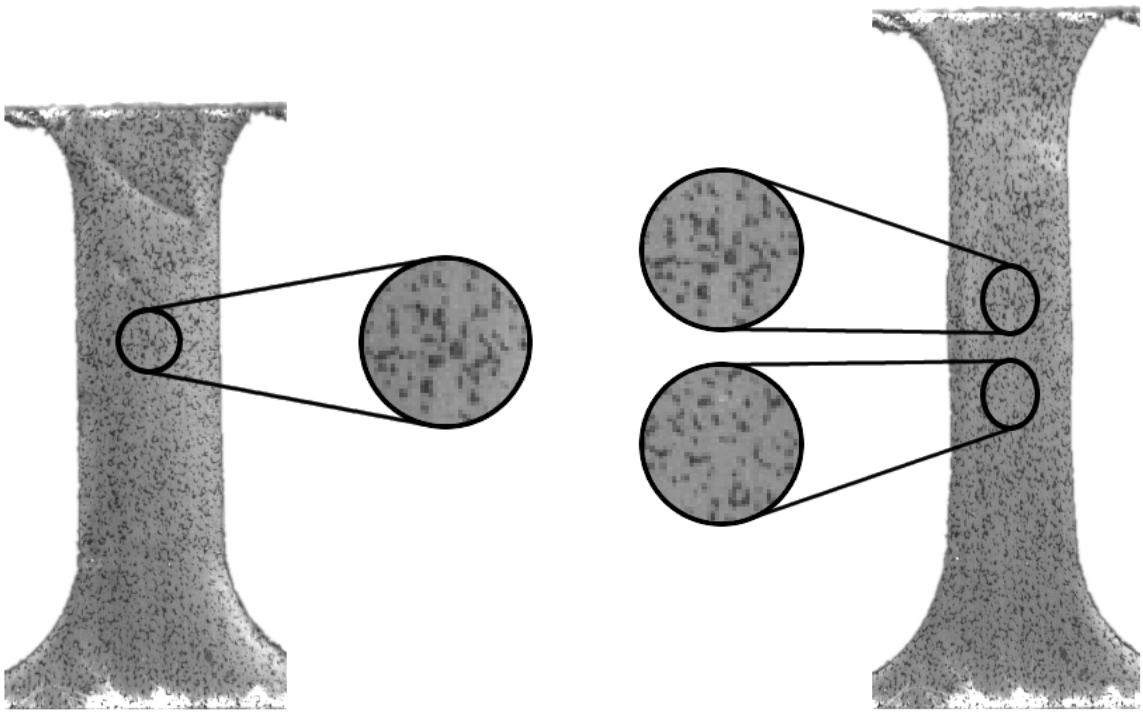

(a) (b)

Figure A.1: Two DIC images from a tensile test showing (a) one subset from the reference image, and (b) two subsets from a current image

This matching process is illustrated with the simple subsets shown in Figure A.2 in which a reference subset $f(i,j)$ is compared to the two potential subsets $g_a(i,j)$ and $g_b(i,j)$. The numbers shown in the figure for each subset represent grayscale values for individual pixels, while the indices i and j refer to the pixel's location. A cost function may then be applied to the subsets, and an extremum is sought. For this example, the minimum will be found for a simplified cost function C as:

$$C = \sum_{(i,j)\in S} |f(i,j) - g(i,j)| \quad \textbf{(A.1)}$$

Where the region S represents the extents of the subset. The subsets at the right of Figure A.2 show the image differences for each example, with summation results given below. The lower value of the cost function for the example in (a) demonstrates that g_a is a

better match for the reference than g_b. This can also be seen by viewing the image differences directly, where larger differences are seen for the example in (b). For an actual DIC analysis, this procedure would then be repeated across the entire image to find the location of the best match to the reference subset.

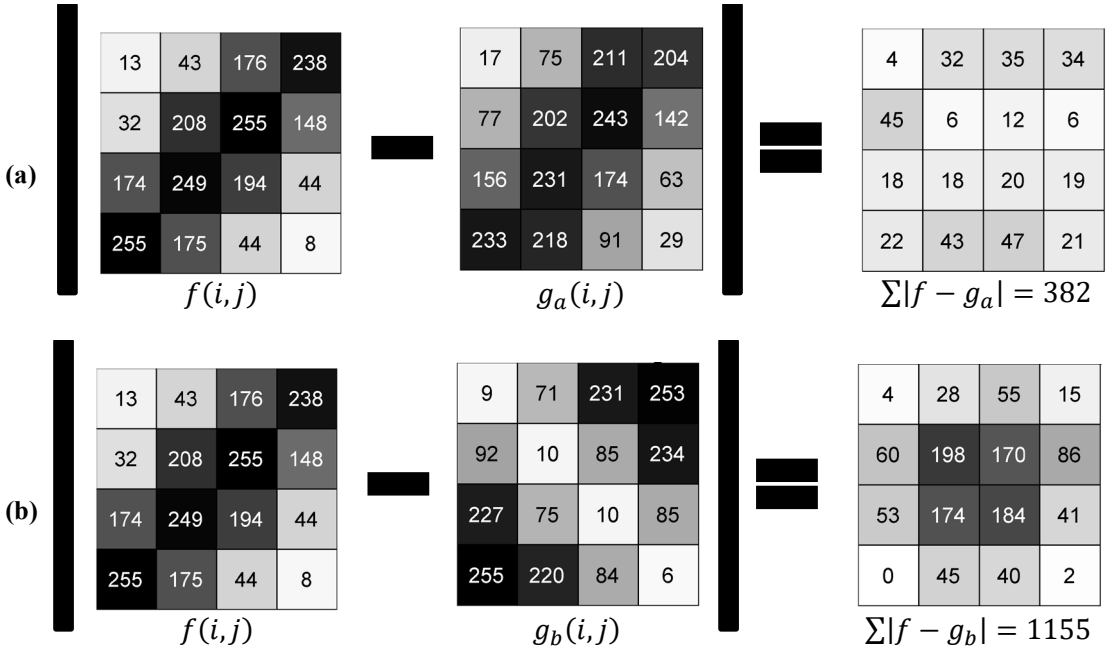

Figure A.2: Application of a simple cost function comparing the reference subset f to (a) the well matched current subset g_a and (b) the poorly matched subset g_b.

Although sufficient for demonstrating DIC concepts, the equation given in A.1 lacks robustness. Ncorr utilizes a normalized cross correlation (NCC) criterion and a normalized least squares (NLS) criterion as cost functions, similarly seeking the extremum for each. Their implementation allows the criterion to be invariant to shifts and scaling in grayscale values. Another challenge when comparing subsets is that their shape is likely to change throughout a test due to deformation of the sample. This can be seen in Figure A.1, where the initially circular subset should be compared to elliptical regions as

the test progresses. The algorithms utilized by Ncorr allow for not only subset displacement (u and v), but also deformation ($\partial u/\partial x$, $\partial u/\partial y$, $\partial v/\partial x$, and $\partial v/\partial y$).

Ncorr solves for these six transformation variables as an optimization problem and uses the inverse compositional Gauss-Newton (IC-GN) method. A solution must be found locating every subset within every analysis image. To reduce this computational load, Ncorr first makes an initial guess for each subset using only translations before seeking an optimized solution in all six variables as depicted in Figure A.3. Also depicted in the figure are the differing approaches used for the first (seed) point versus the remaining subsets.

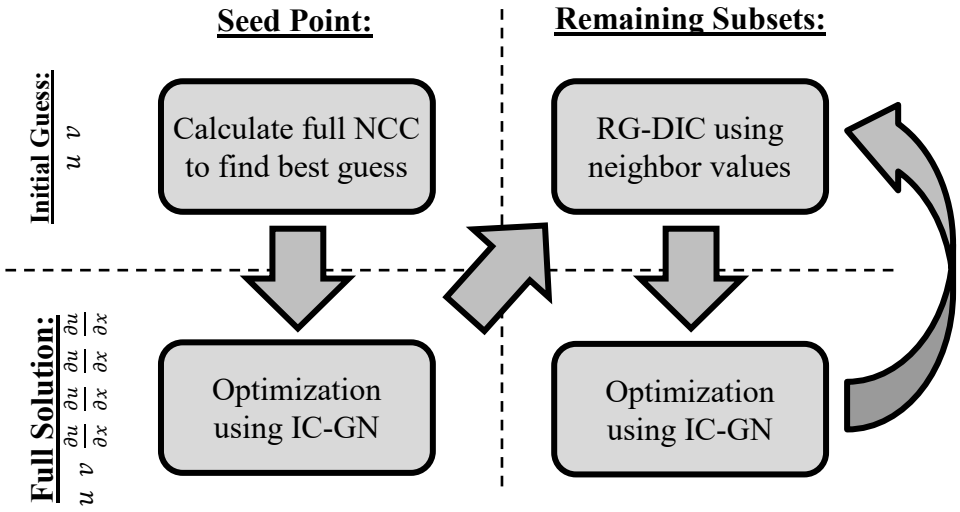

Figure A.3: Schematic of the solution steps

At the onset of the analysis, the user is prompted to select a seed point. The first step in the DIC analysis for each image is then to locate the subset surrounding this seed point. This location is determined in each image by calculating the NCC cost function at every pixel and selecting the best match. Although this step is computationally intensive,

it yields the seed point's displacements with pixel accuracy. This serves as an excellent initial guess for the for the IC-GN optimization routine, which is then used to achieve even greater accuracy for the seed point's displacements.

Once the seed point displacements are calculated in every image, Ncorr locates the remaining subsets using the Reliability Guided (RG-DIC) method. This method uses the calculated displacements for each subset to determine initial guesses for its neighbors based on the assumption that the displacement field is relatively smooth. These initial guesses are then used by the IC-GN method to calculate accurate displacement values. The displacement field solutions are expanded by picking the subset with the best NLS values at each step; this helps to prevent the poorest from being used as initial guesses. Additionally, the use of neighboring values saves computational resources when compared with the seed point's method, which required calculation of the NCC at every pixel.

Although this procedure works well for most general analyses, it cannot yield reliable results when initial guesses are poor. One situation which results in poor guesses, which is relevant to the current study, is when analyzing images with very high deformation. Recall from Figure A.3 that the seed point must first be located in every image by comparison with the original seed subset, and that this initial guess considers only the displacement of the subset without deformation. If the current image is highly deformed, the pixel-to-pixel cost function will yield poor results. As an example, had an undeformed circle been used in figure X1 (b) instead of an ellipse, the resulting subset would not have appeared to match the reference.

Finally, strain values can be calculated from the displacement results of the DIC analysis. Because strain results are very sensitive to any errors in the deformation data, ncorr does not directly output the displacement gradient results ($\partial u/\partial x$, $\partial u/\partial y$, $\partial v/\partial x$, and $\partial v/\partial y$) from the IC-GN method. Instead, ncorr provides an option to calculate strains from displacements within region which effectively "smooths" the results. This option is available for both Lagrangian and Eularian strains. For all other strains variations (engineering strain, different regions, etc.) values may be calculated from displacement fields using MATLAB.

A.1 Ncorr Parameters

When running ncorr, there are many parameters which may be set to control the algorithms. In this section, parameters will be discussed which appeared to have the largest impact on this study's results. Definitions for each parameter will be accompanied by considerations for selecting an appropriate setting and recommended settings as applied to this study.

A.1.1 Subset Radius

The first major parameter, which affects the ability of the ncorr algorithms to locate points, is the radius of the subsets. As discussed previously, a subset is the region of an image surrounding a point in the DIC analysis and points are located by comparing region in different images. Ncorr uses circular subsets with radii defined in pixels by the user. Figure A.4 demonstrates three subsets for the same material point using radii of 10, 20, and 50 pixels.

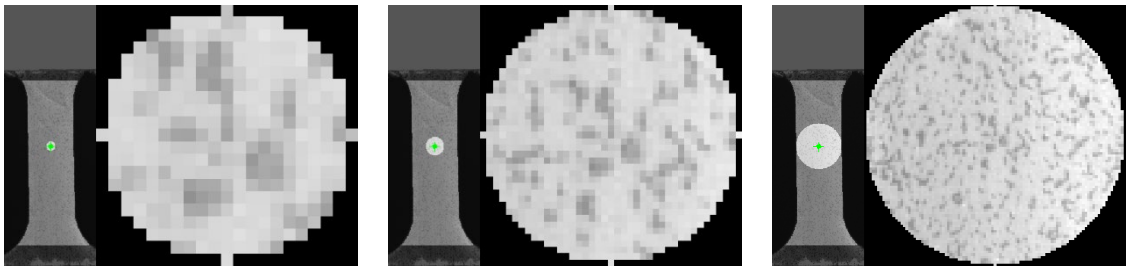

(a) (b) (c)

Figure A.4: Example subsets with radii of (a) 10 pixels, (b) 20 pixels, and (c) 50 pixels

Appropriate sizing of subset radii is largely dependent on the patterning and imaging of samples, but some important characteristics may be noted. First, the subset radius will determine how many pixels will be used to compare regions as seen in Figure A.4; this also determines how much of the random pattern will be 'visible' to the calculations. If the subset is too small, it may not contain enough of the pattern to appear unique and the algorithm may locate an incorrect match. Conversely, very large subsets contain so much data that they are difficult to match, especially when deforming due to strain. A second consideration is that large subsets can also have a smoothing effect on the displacement results, so a general goal is to use the smallest subset radius possible without causing the displacement data to become noisy.

Due to the reliance on these other imaging characteristics, subset radius values are largely determined by trial and error for a given test setup. A set of data may be analyzed with ncorr using different subset radii to determine what values allow the algorithms to reliably find solutions and to yield reasonable displacement data. For the testing procedure outlined in this study, a subset radius of 20 pixels (shown in Figure A.4 b) was determined to solve most data sets reliably to 60% strain.

A.1.2 Subset Spacing

Alongside the subset radius parameter, ncorr includes an option to adjust the spacing of subsets to help decrease the computational load of the analysis. This setting measures the space between pixels in the reference image which will have their displacements calculated; these subsets will be spaced out in a grid arrangement as shown in Figure A.5. In this figure, pixels are highlighted in regions b, c, and d corresponding to subset spacings of 14, 4, and 2 pixels respectively. A 15-pixel grid has been overlaid on the specimen and each region to aid in comparing these spacing values.

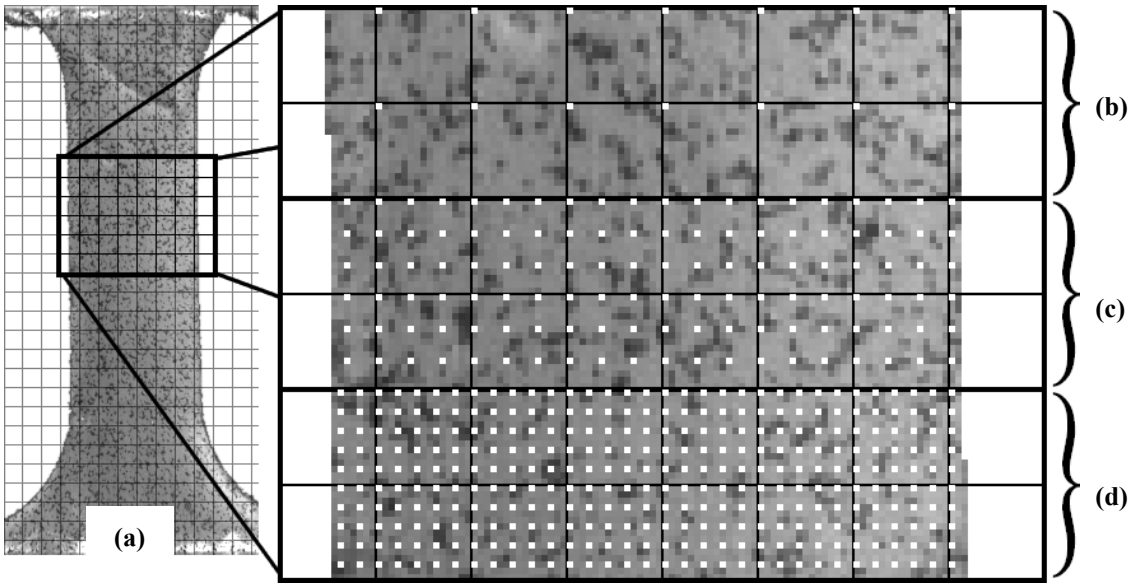

Figure A.5: Example subset positions for the specimen in (a) for spacing values of (b) 14 pixels, (c) 4 pixels, and (d) 2 pixels.

When selecting a subset spacing, the computational load and the continuity of the expected strain field should be considered. Although a subset spacing of zero – which yields results for every pixel of the reference image – is ideal, this can result in very time-consuming analysis for high resolution images. Increasing the spacing value will quickly decrease the number of displacements to be calculated, decreasing both analysis time and

density of results. Table XXXX Demonstrates this with the fraction and percent of calculations listed for several values of subset spacing. The second consideration for the spacing value stems from the RG-DIC method, which requires reasonable initial guesses from neighboring subsets. If subsets are spaced too widely or if there are discontinuities in the displacement field (such as crack growth), poor initial guesses may yield invalid results from the IC-GN optimization algorithm. Unless the invalid points are the last to be calculated, it is likely they will also be used as initial guesses, propagating the invalid results.

Table A.1: Subset spacing values and resulting computational requirements

Spacing Setting [pixels]:	**0**	**1**	**2**	**3**	**4**	**14**
Fraction of pixels calculated	$1/1$	$1/4$	$1/9$	$1/16$	$1/25$	$1/225$
Percent of pixels calculated	100%	25%	11%	6.3%	4.0%	0.4%

In the absence of displacement field discontinuities, appropriate subset spacing values should primarily seek a balance between the time taken for analysis and the resolution of the results. In the current study, two image spacing values have been utilized which help to illustrate this compromise. First, a spacing of four has been used for the initial analysis of a single test specimen from 0-60% strain. To capture this high level of deformation, an excess of 500 images were collected and analyzed. As shown in Table A.1, a spacing value of four will result in displacement calculations for only 4% of the pixels in the reference image. Due to the high resolution of the images in this study, this resulted in values spaced approximately 0.25mm apart. For the remaining DIC analysis in this study, only the linear portion of the stress strain curve was required. Specimen deformation was only calculated up to 6% strain, requiring far fewer images. A

spacing value of two was found to provide results in a comparable amount of time despite an increase in results density with values spaced approximately 0.15mm apart. These same two spacing values can be compared by observing Figure A.5 c and d, which show the same spacing values of 4 and 2, respectively.

A.1.3 Step Analysis

To aid in high strain analysis, ncorr can use a 'stepped' analysis method. Using this method, ncorr will locate seed points in each current image until the cost function shows a poor match. At this point, the most recent current image will be used as a reference for matching the following images. Seed point propagation continues until the cost function again yields poor results, at which point the reference image is updated and the cycle continues. The calculated displacements of these references must be summed with the displacements for each image, which can result in an accumulation of error. Since this method is only necessary for large deformations, however, this accumulation should remain relatively small.

When electing to use stepped analysis, ncorr provides options for how to determine when the reference image will be updated and how to determine seed points at each update. The reference image may either be updated when the seed point matching algorithm shows a poor match (termed "seed propagation") or when a user defined step increment is reached (termed "leap frog"). New seed points will be required each time the reference image is updated. The user may choose to let ncorr determine the new location of the seed points based on the new reference image ("automatic propagation") or to be prompted for a new seed point at each update.

In the present study, stepped analysis was required due to the large strains analyzed. The “seed propagation” and “automatic propagation” options were selected to allow ncorr to determine the reference updates and seed points automatically. To aid in this, it was useful to select the initial seed point in an area which would undergo necking and high strain. This caused the reference updates to occur frequently enough that good matches could still be found for the high strain region.

A.1.4 Strain Radius

As discussed previously, ncorr provides the capability of calculating Lagrangian and Eularian strains from the DIC displacement field. This is done by fitting a plane through a region of displacement points. This region is once again circular and defined by a radius. Unlike the subset radius, which was defined in pixels, the strain radius is defined by the number of subsets contained in the region. The result is that the values for both the subset spacing and the strain radius determine the true size of the region used to define the strain values. This is demonstrated in Figure A.6 where similarly sized strain regions are shown for the same subset spacing values from Figure A.5. To achieve this, regions b, c, and d in the figure would respectively require strain radii of 1, 3, and 5.

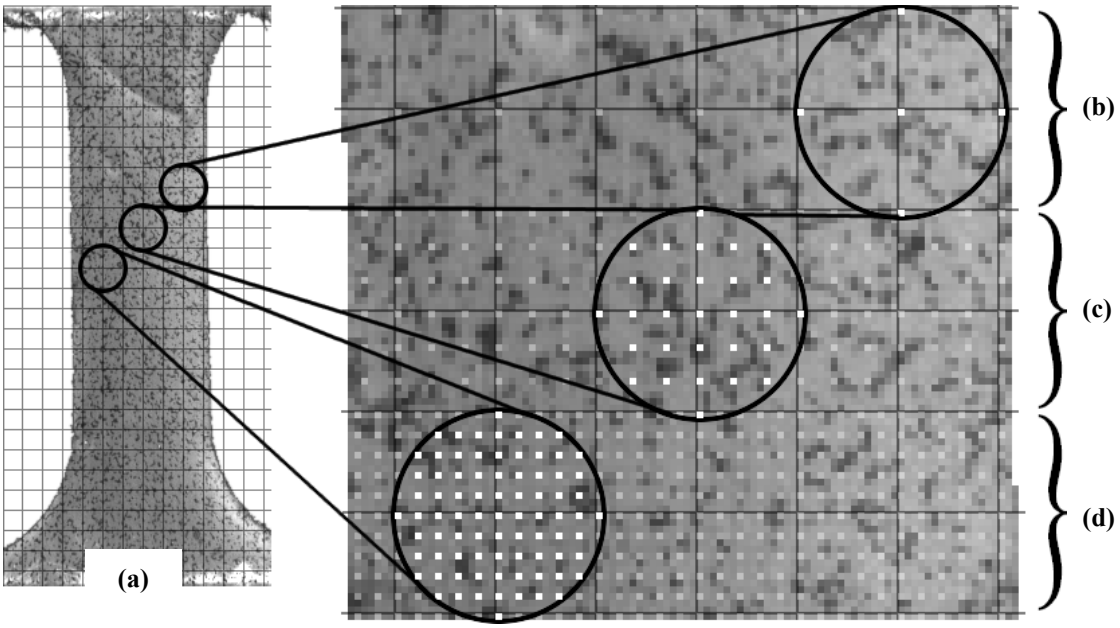

Figure A.6: Similarly sized strain regions for (a) an example specimen with radii settings of (b) 1, (c) 3, and (d) 5

As with selecting the subset radius, the goal when selecting a strain radius is to use the smallest value without excessive noise in the resulting data. Because the strain values are essentially a derivative of the displacement data, they are very susceptible to noise in the DIC displacement results and require careful consideration. Large radii will have a smoothing effect on the strain data which will minimize noise at the expense of seeing smaller localized trends.

An appropriate strain radius will seek to balance the smoothness of the strain data (large radii) with the localized resolution (smaller radii). To aid in visualizing the effects of this strain radius, ncorr provides a 3D plot of displacement data around an example strain region. It is recommended to view this plot for a region of high strain to determine what strain radius will be a good fit for an application. In the present study, a strain radius of 4 subsets was used for the preliminary 0-60% strain analysis and a radius of 6 was

used for the 0-6% analyses. This resulted in the regions for strain calculation being sized with radii of approximately 1.00mm and 0.90mm respectively.

A.2 Data Acquisition Considerations for DIC

The quality of results obtained from DIC is primarily dependent on the quality of the images collected. To optimize these images, careful consideration must be given to the patterning of specimens and the design of the image acquisition system. A critical challenge arises in that these aspects are both highly dependent on the geometry and test method being imaged. A further challenge is that many desired qualities of the patterns, images, and test rig are inter-related.

One illustration of how the DIC system is dependent on the specifics of a test is shown in Figure A.7. For a given test, the required spatial resolution of DIC displacement results will be determined by the expected strain gradients. To achieve this results resolution, the subsets must be of appropriate size and spacing with respect to the physical specimen, which in turn provides a basis for the sizing of the speckle pattern to be applied. This guides the determination of methods for applying the pattern. Finally, the images captured must have enough resolution to capture the speckles, which constrains the camera, lens, and layout of equipment.

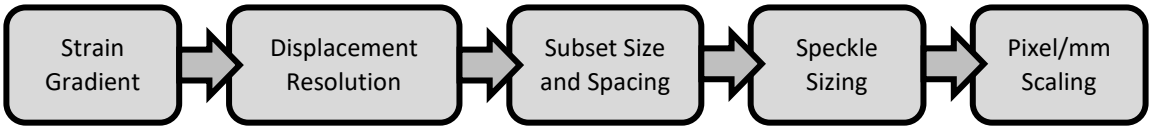

Figure A.7: Example DIC parameter dependence on test setup

The second challenge in designing the acquisition system is that there are many parameters to be determined and most of them will affect others. Figure A.8 gives an

overview with many of the key parameters shown to help illustrate this. Consider the image resolution as an example; the image size in pixels can easily be found from the maximum specimen size and the desired image scale. This will help to determine a suitable camera, lens, and layout. Because this image size acts only as a minimum, the camera selected will likely be capable of higher resolution. This leaves multiple options. A larger sample could be imaged if practical for the experiment. More pixels could be captured to allow a higher result resolution, but this would require smaller subsets (more computational time) and smaller speckles (the pattern methodology could change). The excess pixels could also be left uncaptured, which could allow faster framerates (most machine vision cameras have a "windowed" mode for this purpose), or simply omitted from the analysis (wasting camera capability). With so many inter-dependencies, it is important to test both the speckle patterns and the acquisition setups together to ensure that the selected parameters will produce reliable results from the DIC algorithms.

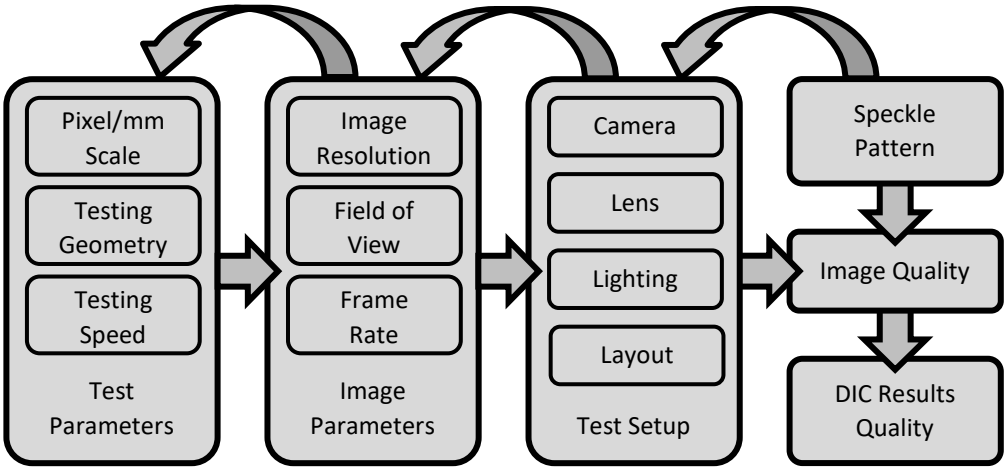

Figure A.8: Interdependence of DIC parameters

A.2.1 DIC Pattern Considerations

One of the most critical aspects of obtaining useful image data for DIC is the speckle pattern which is applied to the specimens. As discussed previously, the sizing of the speckles in the pattern are related to both the image resolution and the resolution of displacement results to be obtained. Additionally, the following pattern characteristics are necessary for reliable DIC data: high contrast, randomness, isotropy, and stability [45]. These qualities are required by the algorithms used in DIC regardless of the methods used for applying speckles, which vary by application (including spray painting, ink stamping, and even drawing marks by hand). In the present study, patterns were created by hand stamping ink onto specimens using a foam pad, as shown in Figure A.9.

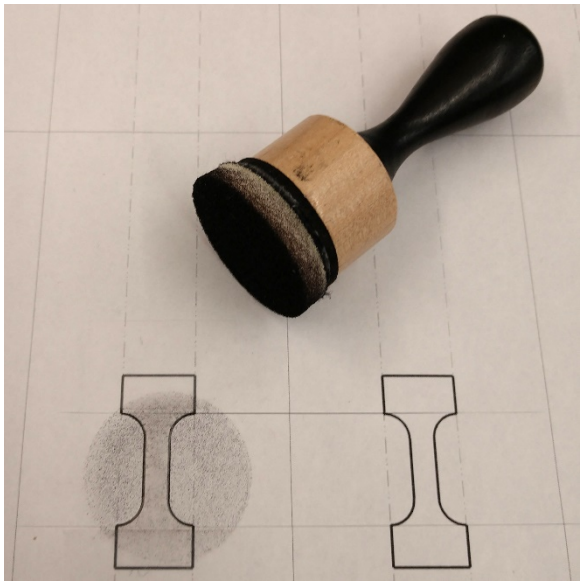

Figure A.9: Specimen inking tool

In properly image each speckle in the pattern, it is recommended that they be between 3-5 pixels in size on the captured images [45]. Speckles smaller than this may not cleanly line up with the image pixels and will likely show an ‘aliased’ effect which is

more difficult for the DIC algorithms to pick up. If the speckle pattern is too large in the image, subset sizing will need to be increased (ideal subset sizing is related to speckle size) and increased computational time will be required due to the increase in number of pixels compared for each subset. It is also recommended that the spacing between adjacent speckles should be about equal to the size of the speckles themselves. DIC algorithms can handle some variation in size, which is to be expected from many application methods. Speckle sizing can be easily observed by viewing captured images in any software which will allow the image to be scaled large enough to view individual pixels.

For the DIC cost functions to be most effective in comparing subset pixels, it is desired to have a large difference between the grayscale values of the speckles and the background; i.e., a high level of contrast is sought in the image. Although the image contrast will primarily be a result of the speckle pattern, it may also be affected by the camera settings (exposure and gain) and the lighting. A quick method of observing the high and low values is to view the image in software where pixel intensity values are reported by cursor location; some commercial DIC software has this functionality built in. A more comprehensive method, as used in this study, is to examine the grayscale histogram for the speckled region using image editing software. Figure A.10 shows two examples of this method, applied to images representing 0% and 60% engineering strain (based on grip separation) for the same specimen. The pixel areas counted for each histogram, which are highlighted, were the regions of interest (ROI) as initially specified for the undeformed image and as calculated by the DIC algorithm for the 60% image.

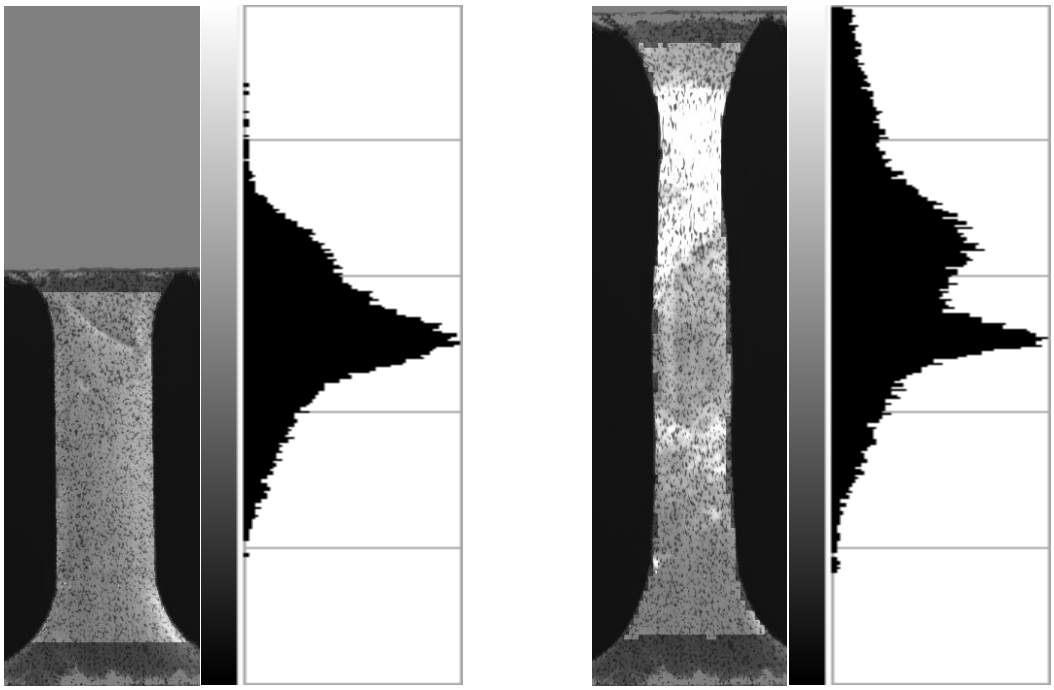

(a) (b)

Figure A.10: Specimen images with ROI highlighted and histograms for intensities within ROI at 0% and 60% strain (engineering strain, by jaw separation)

The next two qualities required for the speckle pattern are randomness and isotropy. The requirement for randomness in the pattern stems from the matching algorithms used by DIC, where a unique match is desired for each subset. If directionality is present in the pattern, subset matching will be less accurate along any directions the pattern is oriented. This can be seen in the example shown in Figure A.11, which shows an extremely directional pattern. Matching a subset in the horizontal direction will be accurate due to the randomness of the pattern but will not yield acceptable results in the vertical direction because a unique match is not possible. In the present study, patterns resulting from potential speckling methods were observed to subjectively determine if they met these qualities. The hand-stamping method utilized appeared to meet these goals and captured images were able to be processed by ncorr.

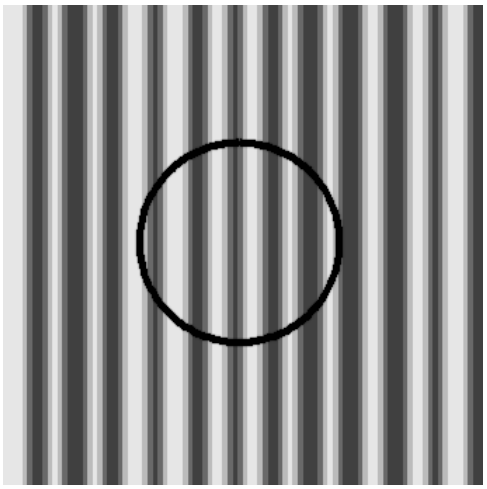

Figure A.11: Example of a problematically directional speckle pattern

The final necessary quality for a speckle pattern is stability, or the ability for the pattern to adhere to the specimen. This can be tricky, as the pattern must also deform with the specimen while still being recognizable to the DIC algorithms; drastic changes in shape or grayscale intensity could make subset matching inaccurate or impossible. Additionally, this must be accomplished without affecting the properties for the test. As an example, spray painted speckles work well for many tests because the very thin layer of paint will not have an appreciable effect on the response of the material. These thin layers of paint would not have been acceptable in the present study, however, where the paint thickness would not have been negligible compared to the thin polymer films being analyzed. Stamped ink patterns avoided this issue but presented a further challenge at high strains where the ink would become lighter as it stretched. This was compounded by the material itself, which would become lighter and more opaque under strain. The changes in both the speckles and material background can be seen in Figure A.10 above.

As shown in that figure, this challenge was mitigated by using the image histograms to ensure that contrast ratios remained acceptable at the highest strains to be tested.

A.2.2 Camera Setup Considerations

There are several pieces of equipment which must work together to collect images for DIC analysis. An appropriate camera for the test is of paramount importance. It must also be accompanied by a quality lens which will in turn direct the layout of the equipment. Finally, the lighting system for imaging is important, as it is one of the largest factors in ensuring high contrast and minimizing data noise.

Camera selection is mostly dictated by the qualities required of the captured images. Machine vision cameras are generally preferred as they have capabilities useful for controlled data acquisition; e.g. most have software development kits (SDKs) allowing custom control software to be developed and can be activated by trigger signals to control their timing. Because the DIC algorithms only compare grayscale intensities, black and white cameras are preferred. Color cameras construct image from a mosaic of single-colored pixels leading to unnecessary compromises. One of the most important aspects of selecting a camera is the sensor it contains; the size of this sensor and its resolution will determine important parameters such as the FOV and how large the pixels are (bigger sensor pixels collect light faster). The speed of the camera in frames per second (FPS) should also be considered if fast tests are expected. The actual frame rate for a test, however, will be reliant on the lighting and camera settings. For the present study, a FLIR Chameleon3 monochrome camera with a Sony IMX264 sensor was used; key specifications for the camera can be found in Table A.2.

Table A.2: DIC camera specifications for current study

Camera	FLIR Chameleon3 5.0MP Mono USB3
Sensor	Sony IMX264
Sensor size	2/3”
Chroma	Monochrome
Resolution	2448x2048 pixels
Maximum Frame Rate	35 FPS
Shutter	Global
Bit-depth	12-bit

The next considerations when building an imaging system are the lens and the layout of equipment. A high-quality lens should be used, with special attention to its resolution focal length. Lens resolutions can be measured according to the smallest details they can resolve (using line pairs per mm). Ultimately, however, lenses are generally selected to meet or exceed the resolution capabilities of the camera’s sensor. The focal length is a measure of the magnification power of the lens and, together with the camera’s sensor size, determines the angular field of view for the setup. This angle and the size of the specimen to be imaged will determine the required working distance between the specimen and the camera setup. The equipment layout must rigidly maintain the working distance throughout the test. If there is any motion in the camera, it will later show up as rigid body motion in the DIC results. For this study, a TECHSPEC® C Series 25 mm fixed focal length lens from Edmund Optics was used; specifications for this lens are shown in Table A.3. The camera and lens were mounted on a tripod located behind the load frame as seen in Figure A.12. The use of a tripod provided flexibility for camera positioning, while its location allowed access to the specimens and avoided disturbances to the camera.

Table A.3: DIC lens specifications for current study

Brand	Edmund Optics
Family	TECHSPEC® C Series
Focal Length	25mm, fixed
Aperture Range	f/1.4 - f/17
Maximum Camera Sensor Format	2/3”
Field of View for 2/3" Sensor	19.8°
Working Distance	100 - ∞

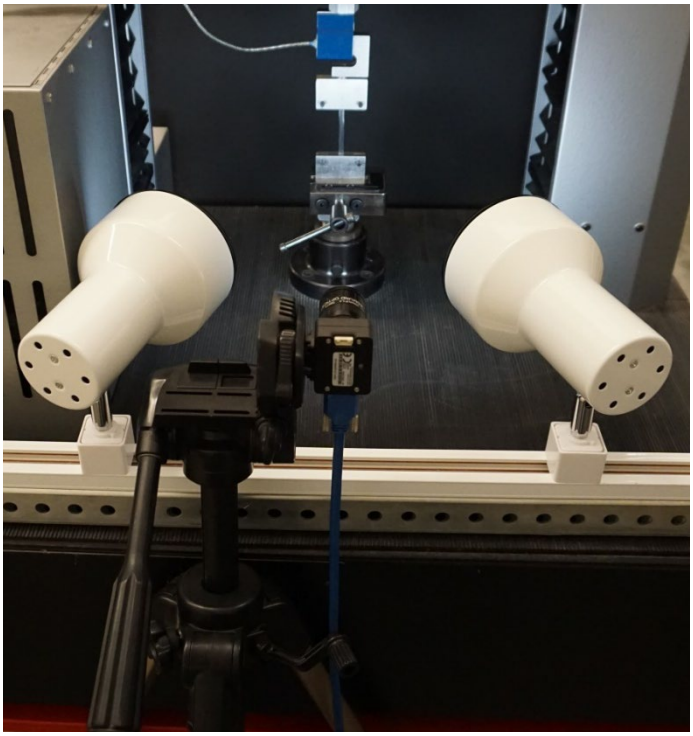

Figure A.12: DIC equipment layout

Perhaps the most important consideration when building an imaging system is lighting. The lighting must work with the speckle pattern to produce even and adequate contrast in the images, and work well with the camera settings to produce images without excess noise. Where imaging speed is a consideration, adequate lighting must be provided so the camera may be set to a fast exposure time to allow the frame rates required. To achieve these imaging qualities, the lighting must be uniform, diffuse, and of

an appropriate intensity. Reflections and highlights must be avoided because they will create local inconsistencies in the speckle pattern; speckling methods are preferred which produce matte or non-reflective surfaces. Two pairs of lights were used for the present study. The first pair of lights were placed behind the camera (not shown in Figure A.12) and used 45W CFL bulbs illuminating the specimen through diffusion umbrellas. To supplement this, two 85W LED bulbs were also added to the setup, aimed so they would reflect light off the front side of the same umbrellas. This setup resulted in enough light intensity for the higher strain rate tests (which required higher FPS), but still maintained reasonably diffuse lighting.

A major challenge in setting up the imaging system for the present series of tests was the specimen material itself, which would reflect light and change in appearance over the course of testing. Material reflections necessitated the use of very diffuse lighting and careful positioning of the light sources. This situation was aggravated by the tendency of the thin material to curl before loading, which lead to highlights. Specimens were semi-transparent white prior to testing and became opaque white as the material underwent strain as can be seen in Figure A.10. A black backdrop was used when imaging specimens. This made specimen edges easy to identify but lead to the material appearing darker in early images due to its transparency. When the material became opaque in later images, it appeared much lighter; this was accompanied by the speckle in stretching and appearing lighter as well. Imaging setups ultimately needed to produce acceptable levels of contrast throughout this range, which was influenced primarily by the camera settings (exposure and gain) and the lighting (intensity and layout). Image intensity histograms were utilized as discussed earlier to evaluate and improve contrast results.

Appendix B: Tensile Test Breakpoint Data

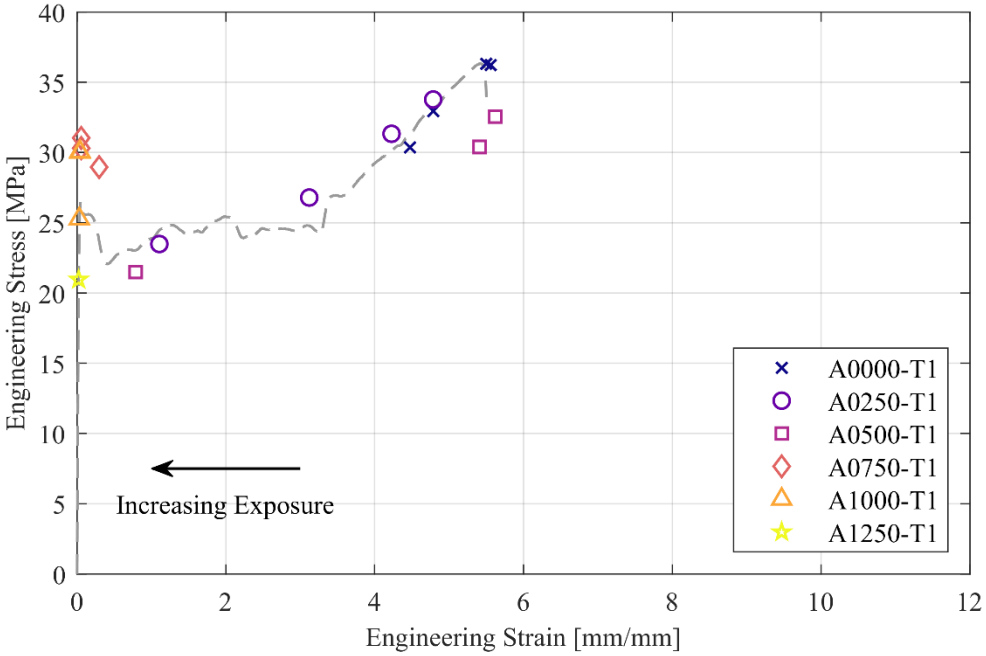

Figure B.1: Break points for A specimen tensile tests at 1E-1 sec^{-1} strain rate (method one)

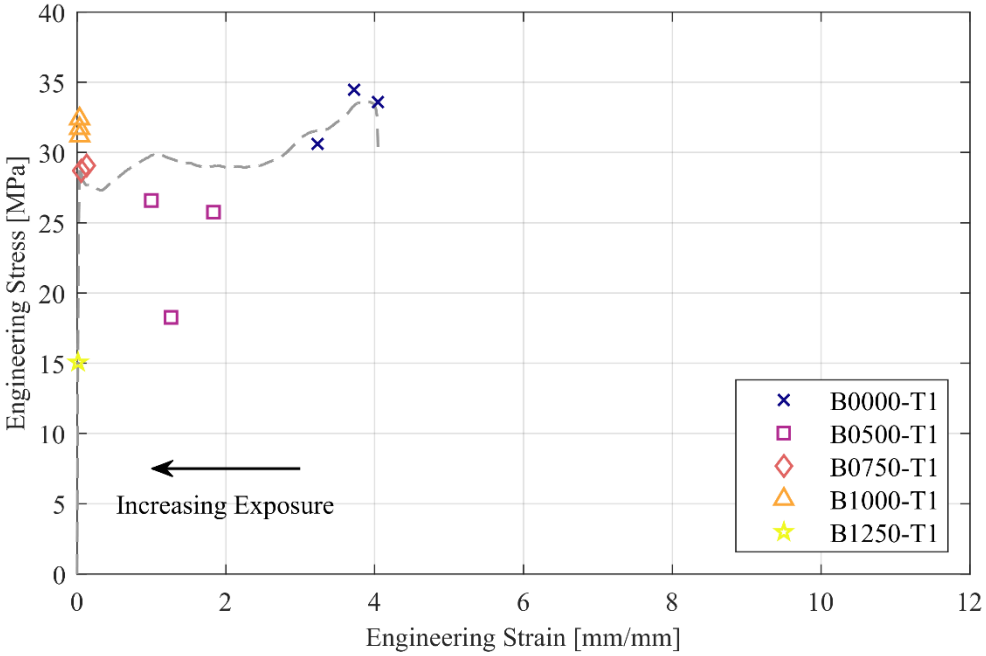

Figure B.2: Break points for B specimen tensile tests at 1E-1 sec^{-1} strain rate (method one)

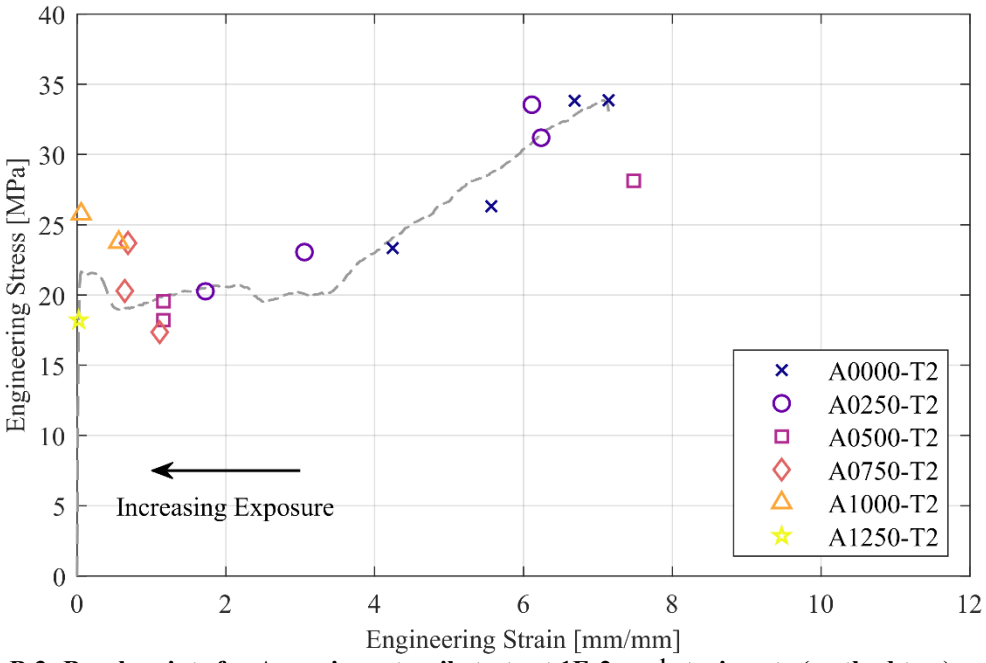

Figure B.3: Break points for A specimen tensile tests at 1E-2 sec^{-1} strain rate (method two)

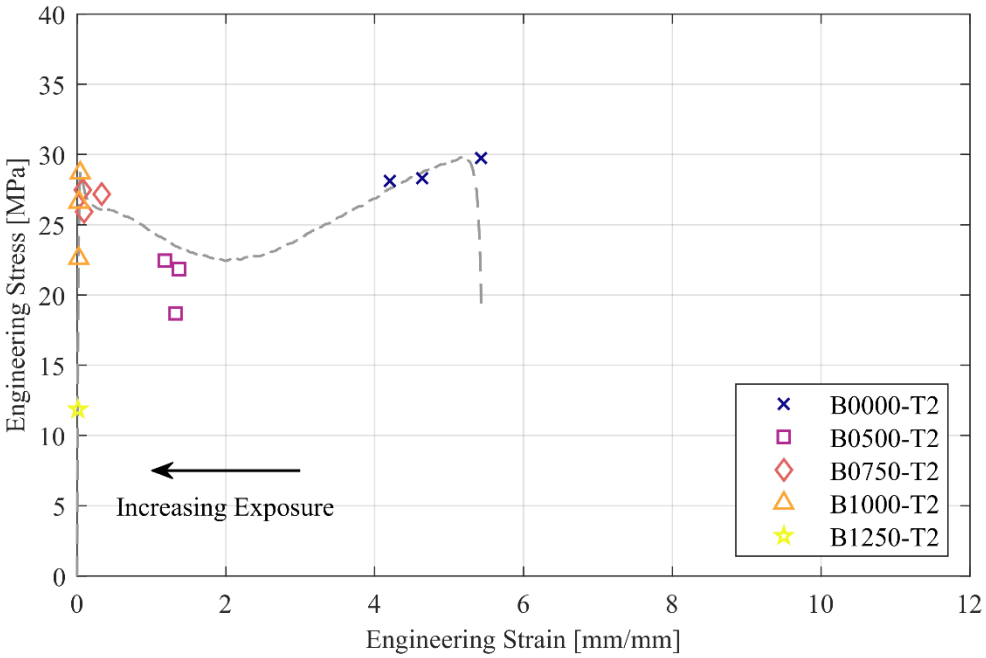

Figure B.4: Break points for B specimen tensile tests at 1E-2 sec^{-1} strain rate (method two)

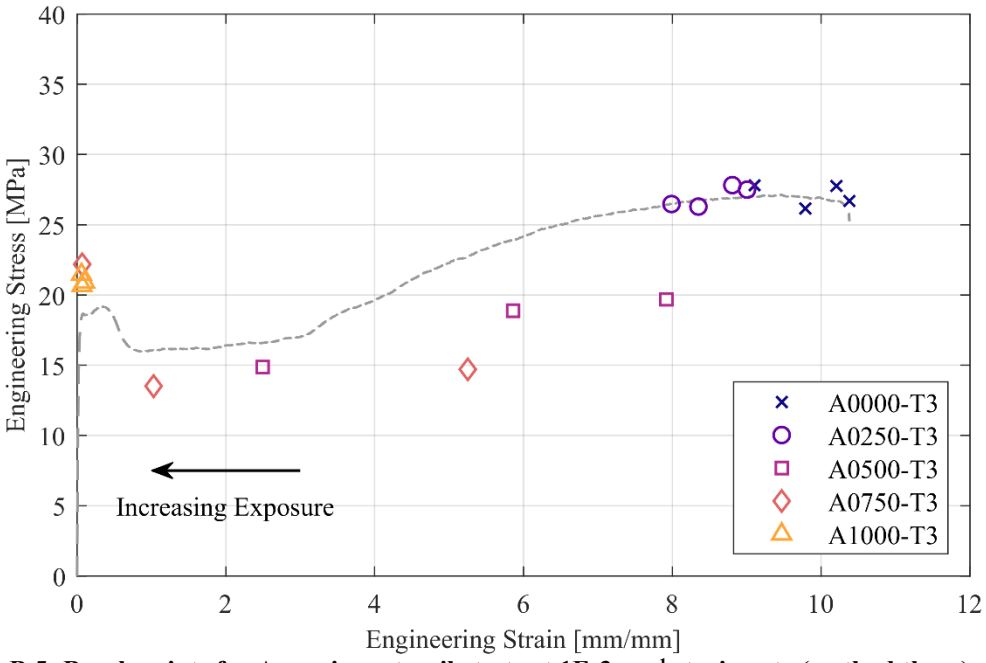

Figure B.5: Break points for A specimen tensile tests at 1E-3 sec^{-1} strain rate (method three)

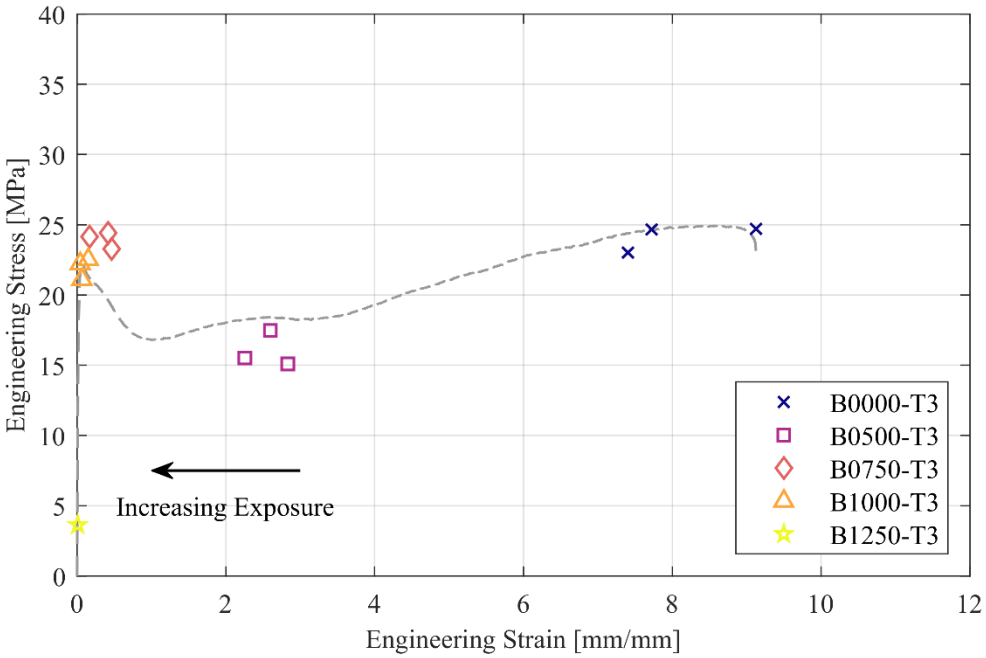

Figure B.6: Break points for B specimen tensile tests at 1E-3 sec^{-1} strain rate (method three)

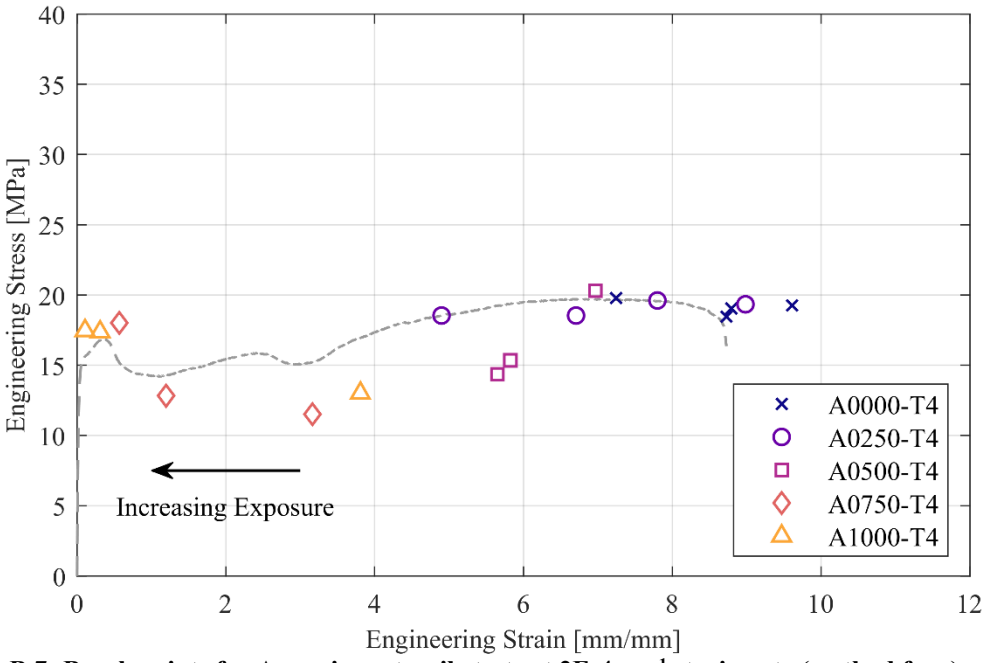

Figure B.7: Break points for A specimen tensile tests at 2E-4 sec^{-1} strain rate (method four)

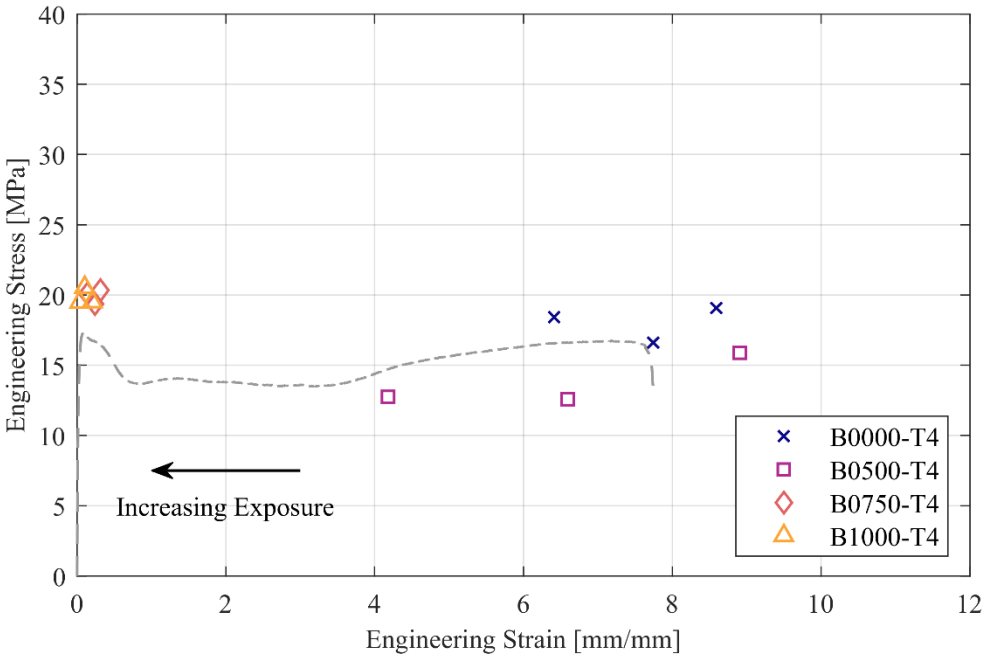

Figure B.8: Break points for B specimen tensile tests at 2E-4 sec^{-1} strain rate (method four)

Appendix C: Essential Work of Fracture Reports

Test reports are presented in the following sections for the DENT specimens and subsequent essential work analyses in this study. The results presented and reporting format follow recommendations in *Essential Work of Fracture* [34]. Table C.1 presents the DENT testing conditions, which were consistent for all specimens. Sections C.1 and C.2 of this appendix contain reports for A specimens and B specimens, respectively, with sub-sections for specimens at each level of exposure.

Table C.1: Essential work of fracture testing conditions for all DENT specimens

Specimen width	30	mm
Mean DENT specimen thickness	0.062	mm
Test speed (crosshead velocity)	10	mm/min
Test temperature	20	°C
Specimen Orientation	0°	(machine direction)
Maximum ligament length	16	mm
Minimum ligament length	6	mm

C.1 Results for A Specimens

Table C.2 lists testing conditions for tensile tests used to derive the theoretical DENT maximum stress ($1.15\sigma_y$) and stress values for the stress criteria applied in this study. The resulting $1.15\sigma_y$ value is provided as a reference only and is plotted only for the unexposed samples in Figure C.2. DENT specimen data were considered invalid for EWF analysis if test maximum stress values were below 60% of the maximum stress from unexposed specimens. This cutoff value ($0.60\sigma_{m,0}$) is plotted for each exposure level in the corresponding maximum stress versus ligament length figure.

Table C.2: Tensile test conditions and EWF stress criterion for A specimens

Tensile specimen geometry	ASTM D1708
Mean D1708 specimen thickness	0.065 mm
Tensile test speed	12.5 mm/min
Mean tensile yield stress, σ_y	22.2 MPa
Theoretical DENT max stress ($1.15\sigma_y$)	25.5 MPa
Mean max stress (unexposed), $\sigma_{m,0}$	23.8 MPa
Max stress cutoff ($0.60\sigma_{m,0}$)	14.3 MPa

Table C.3 summarizes regression results for each exposure level. Slope (βw_p) and intercept (w_e) values are included, as well as 95% confidence intervals and R^2 values. Resulting regression lines and confidence intervals are plotted for each exposure level in the corresponding specific work versus ligament length figures.

Table C.3: Essential work results for A specimens, by exposure time

Exposure [hr]	**0**	**500**	**750**	**1000**	**1250**
Valid EWF specimens	12	12	12	3	1
Mean max stress, σ_m [MPa]	23.8	25.5	23.6	19.3	15.9
Essential work of fracture, w_e [kJ/m²]	30.8	41.2	39.7	8.52	*
w_e ± 95% confidence interval	± 40.6	± 75.8	± 51.4	± 4.14	*
Plastic work factor, βw_p [MJ/m³]	20.0	12.7	0.09	0.24	*
βw_p ± 95% confidence interval	± 3.63	± 6.78	± 4.73	± 0.30	*
Regression R^2	0.94	0.64	0.00	0.99	*

*Denotes too few specimens to perform regression

C.1.1 Unexposed A Specimens

Figure C.1 shows load-displacement plots for each unexposed A specimen. A second axis is also provided to allow comparison between exposure levels. Table C.4 lists EWF data for all unexposed A specimens.

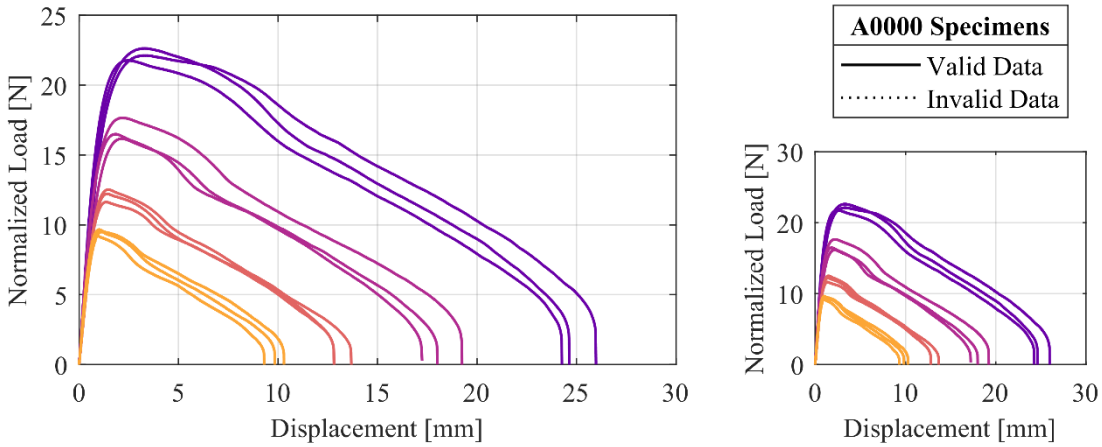

Figure C.1: Load-displacement curves for unexposed A specimens

Table C.4: Essential work of fracture data for unexposed A specimens

Thick-ness [mm]	Ligament Length [mm]	Peak Load [N]	Max Stress [MPa]	Failure Energy [mJ]	Specific Work [kJ/m²]	Invalid Data
0.052	6	8.1	26.09	52.1	166.92	
0.060	6	9.2	25.66	54.6	152.93	
0.066	6	9.8	24.92	54.4	138.01	
0.057	8	10.7	23.57	86.2	190.69	
0.061	8	12.3	25.36	100.7	208.08	
0.056	8	11.1	24.74	87.9	196.15	
0.073	12	19.6	22.26	206.0	234.33	
0.072	12	18.8	21.82	207.5	241.05	
0.061	12	17.5	23.82	209.5	285.05	
0.052	16	18.5	22.39	318.3	386.23	
0.055	16	19.5	22.04	297.7	336.73	
0.063	16	23.2	22.91	364.2	359.90	

Figure C.2 shows the EWF stress cutoff and maximum stress values for each specimen. Specific work values are shown with final regression results in Figure C.3.

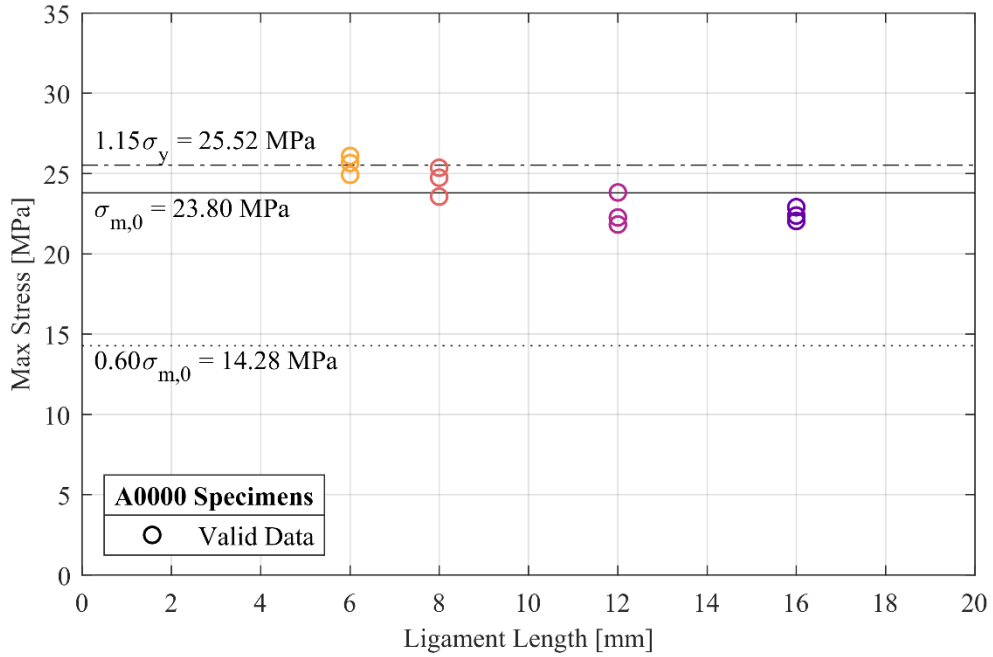

Figure C.2: Maximum stress versus ligament length for unexposed A specimens

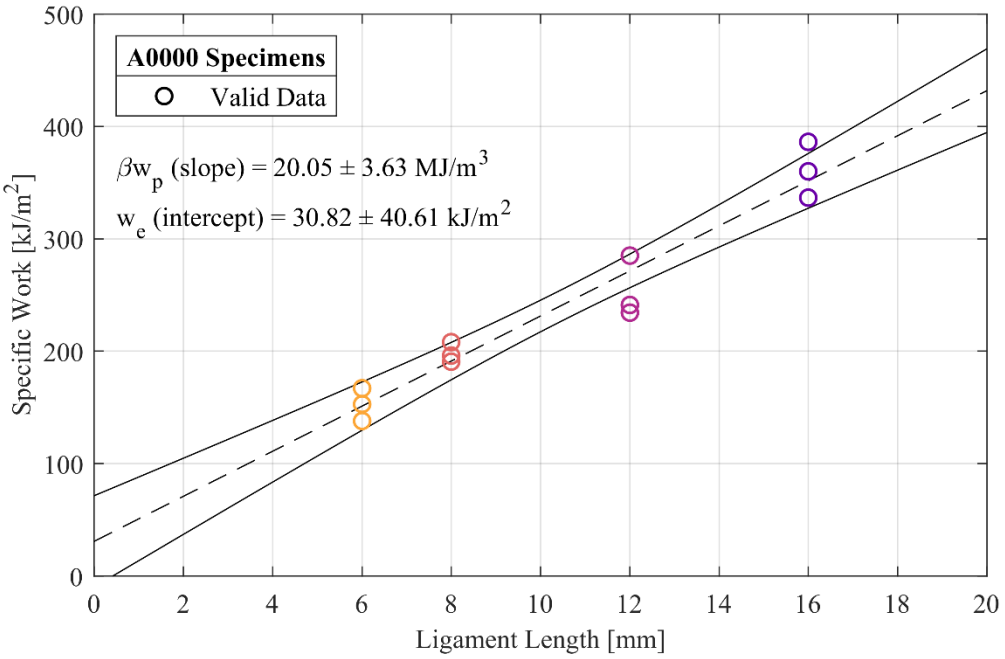

Figure C.3: Essential work of fracture regression results for unexposed A specimens

C.1.2 500-hour A Specimens

Figure C.4 shows load-displacement plots for each 500-hour A specimen. A second axis is also provided to allow comparison between exposure levels. Table C.5 lists EWF data for all 500-hour A specimens.

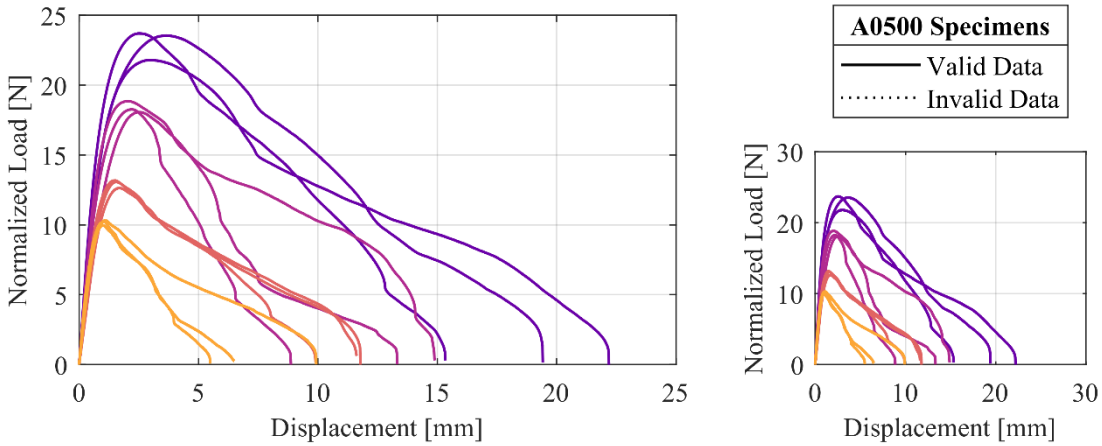

Figure C.4: Load-displacement curves for 500-hour A specimens

Table C.5: Essential work of fracture data for 500-hour A specimens

Thick-ness [mm]	Ligament Length [mm]	Peak Load [N]	Max Stress [MPa]	Failure Energy [mJ]	Specific Work [kJ/m²]	Invalid Data
0.051	6	8.2	26.90	27.1	88.43	
0.051	6	8.5	27.68	25.5	83.34	
0.042	6	7.0	27.82	37.2	148.41	
0.060	8	12.8	26.69	85.9	178.99	
0.057	8	11.7	25.58	67.3	147.55	
0.060	8	12.8	26.45	85.2	176.68	
0.039	12	11.4	24.38	74.8	159.73	
0.063	12	18.6	24.65	89.5	118.81	
0.066	12	20.0	25.45	186.4	237.15	
0.061	16	21.4	22.06	264.3	273.00	
0.074	16	28.2	23.83	320.3	270.49	
0.072	16	27.5	23.99	248.2	216.22	

Figure C.5 shows the EWF stress cutoff and maximum stress values for each specimen. Specific work values are shown with final regression results in Figure C.6.

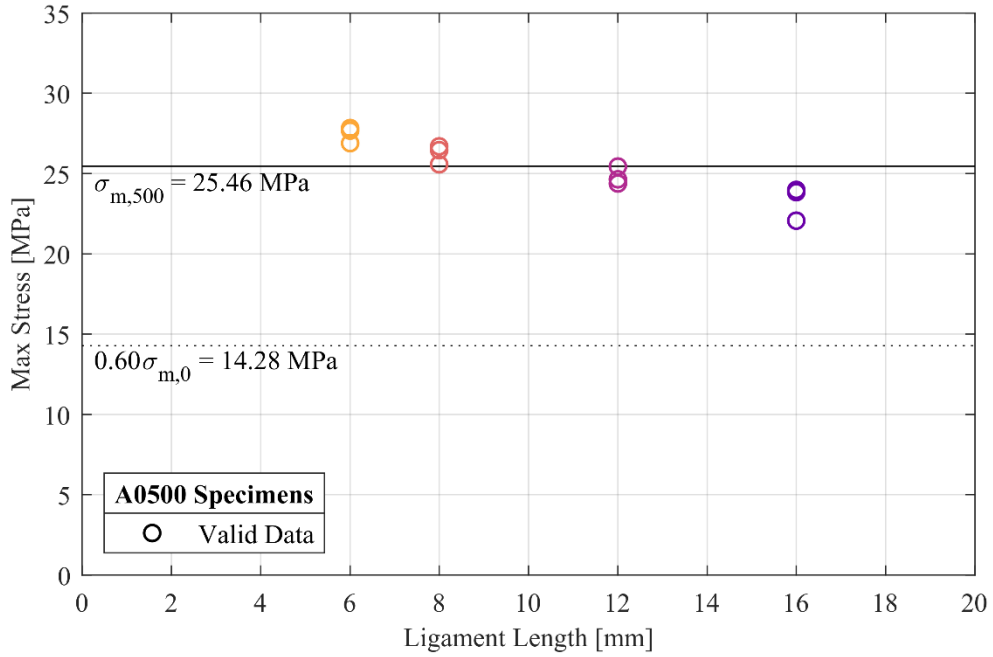

Figure C.5: Maximum stress versus ligament length for 500-hour A specimens

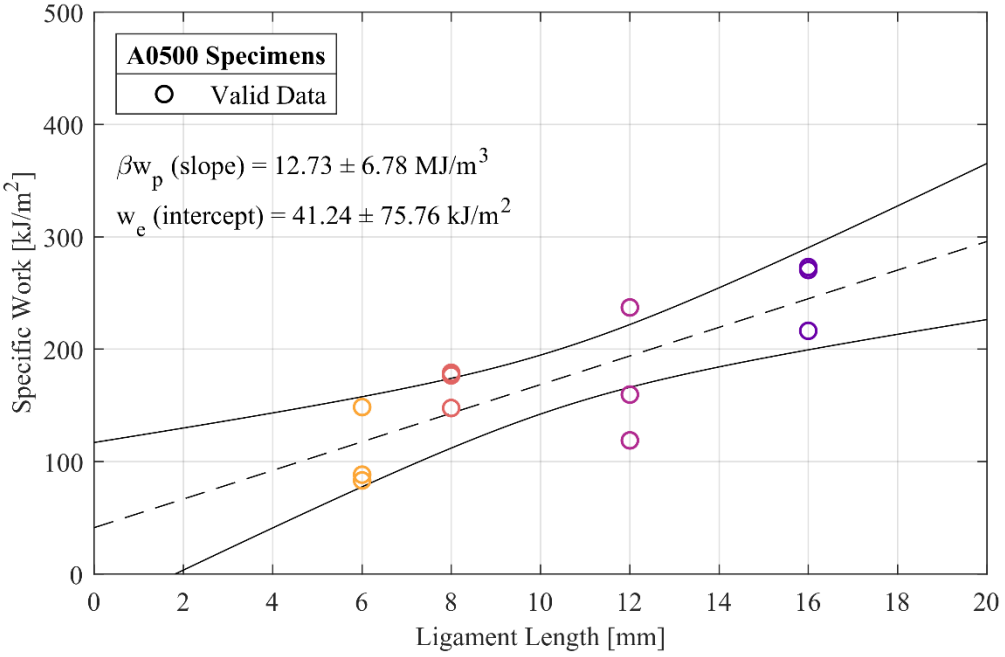

Figure C.6: Essential work of fracture regression results for 500-hour A specimens

C.1.3 750-hour A Specimens

Figure C.7 shows load-displacement plots for each 750-hour A specimen. A second axis is also provided to allow comparison between exposure levels. Table C.6 lists EWF data for all 750-hour A specimens.

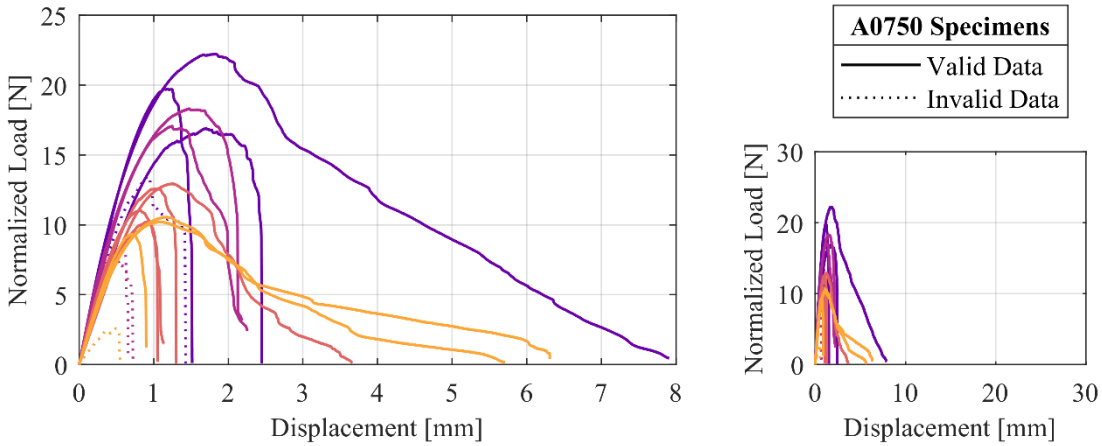

Figure C.7: Load-displacement curves for 750-hour A specimens

Table C.6: Essential work of fracture data for 750-hour A specimens

Thick-ness [mm]	Ligament Length [mm]	Peak Load [N]	Max Stress [MPa]	Failure Energy [mJ]	Specific Work [kJ/m²]	Invalid Data
0.077	6	13.1	28.48	32.9	71.50	
0.037	6	1.6	6.98	0.5	2.44	stress
0.059	6	8.8	25.18	5.2	14.91	
0.058	6	9.5	27.54	29.4	85.12	
0.058	8	11.8	25.47	10.6	22.77	
0.051	8	8.4	20.67	5.9	14.68	
0.060	8	10.7	22.33	8.2	17.00	
0.051	8	10.6	26.18	19.5	47.98	
0.048	12	6.0	10.36	2.7	4.74	stress
0.050	12	6.8	11.19	2.8	4.66	stress
0.062	12	18.4	24.70	29.4	39.49	
0.057	12	15.7	23.02	23.1	33.89	
0.057	16	15.7	17.09	28.5	31.11	
0.062	16	19.7	19.96	20.0	20.23	
0.046	16	9.9	13.60	9.5	13.09	stress
0.068	16	24.4	22.49	96.4	88.92	

Figure C.8 shows the EWF stress cutoff and maximum stress values for each specimen. Specific work values are shown with final regression results in Figure C.9.

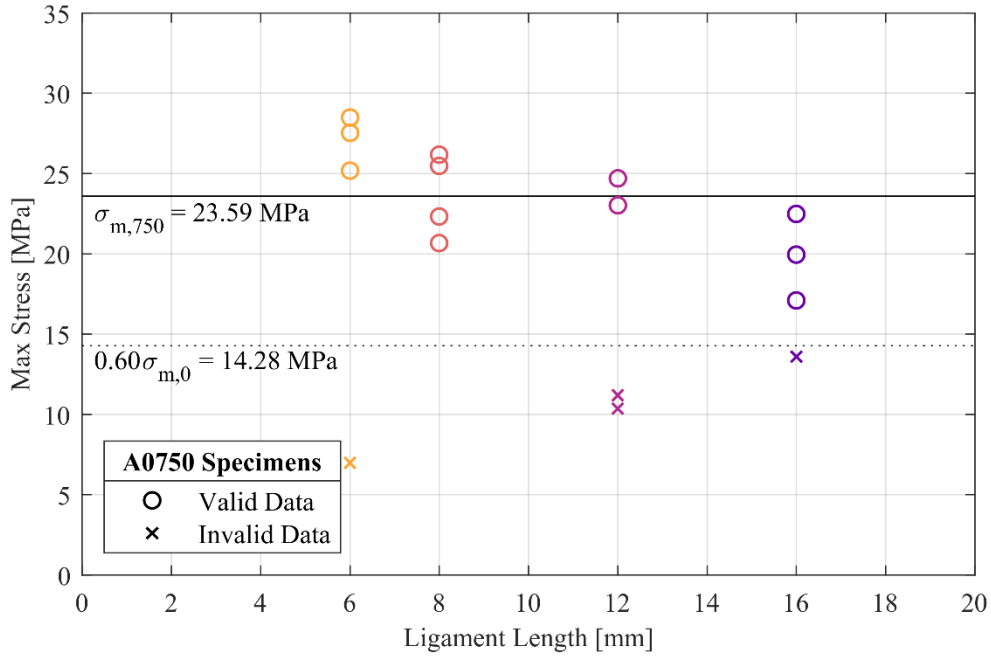

Figure C.8: Maximum stress versus ligament length for 750-hour A specimens

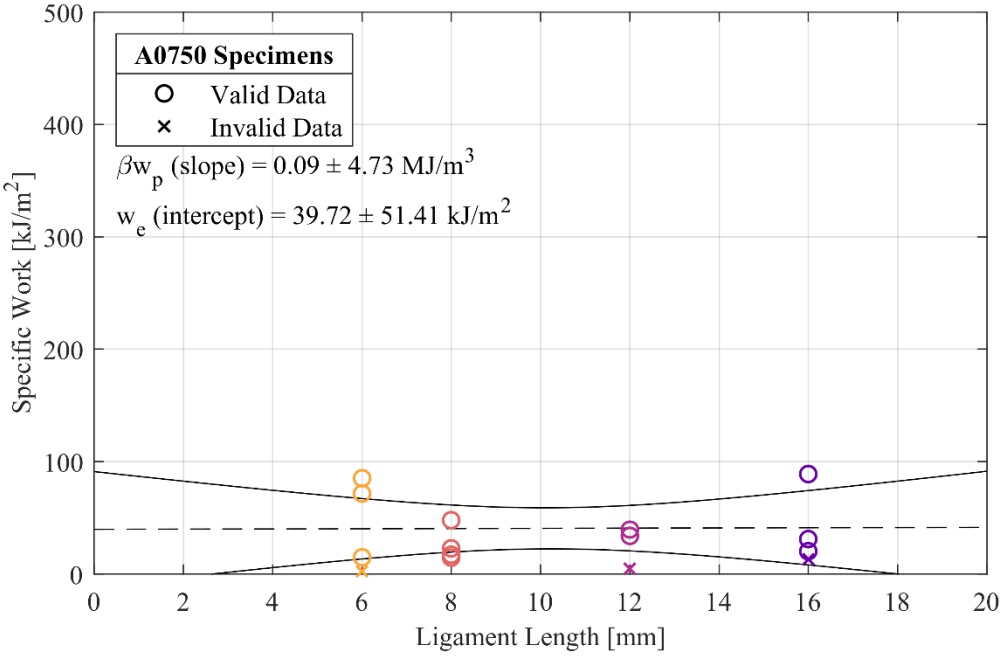

Figure C.9: Essential work of fracture regression results for 750-hour A specimens

C.1.4 1000-hour A Specimens

Figure C.10 shows load-displacement plots for each 1000-hour A specimen. A second axis is also provided to allow comparison between exposure levels. Table C.7 lists EWF data for all 1000-hour A specimens.

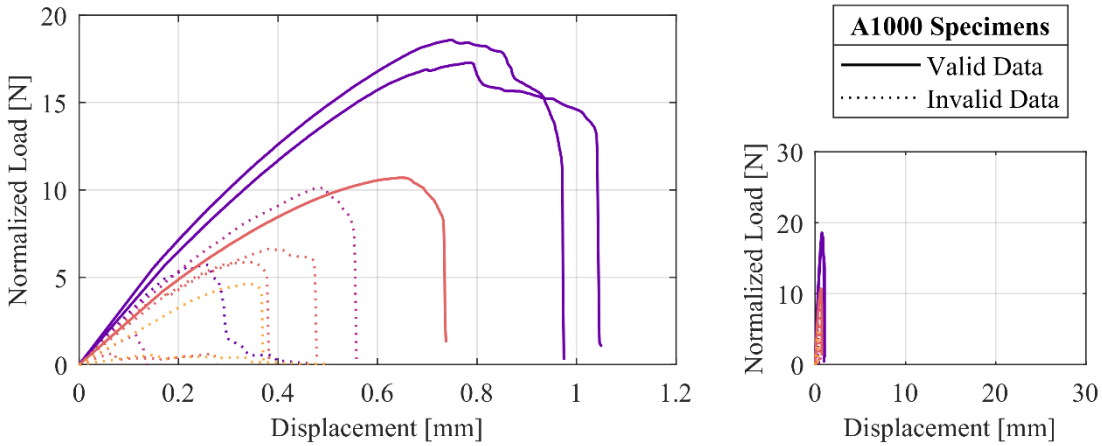

Figure C.10: Load-displacement curves for 1000-hour A specimens

Table C.7: Essential work of fracture data for 1000-hour A specimens

Thick-ness [mm]	Ligament Length [mm]	Peak Load [N]	Max Stress [MPa]	Failure Energy [mJ]	Specific Work [kJ/m²]	Invalid Data
0.062	6	0.5	1.46	0.1	0.38	stress
0.054	6	4.0	12.47	0.9	2.77	stress
0.059	8	0.6	1.34	0.1	0.22	stress
0.061	8	6.6	13.46	2.1	4.21	stress
0.068	8	6.5	11.93	1.6	2.95	stress
0.064	8	11.1	21.65	5.4	10.44	
0.056	12	1.6	2.33	0.1	0.17	stress
0.060	12	9.8	13.64	3.4	4.73	stress
0.063	16	5.8	5.78	1.2	1.18	stress
0.070	16	21.2	18.82	13.8	12.25	
0.066	16	18.3	17.48	13.1	12.46	

Figure C.11 shows the EWF stress cutoff and maximum stress values for each specimen. Specific work values are shown with final regression results in Figure C.12.

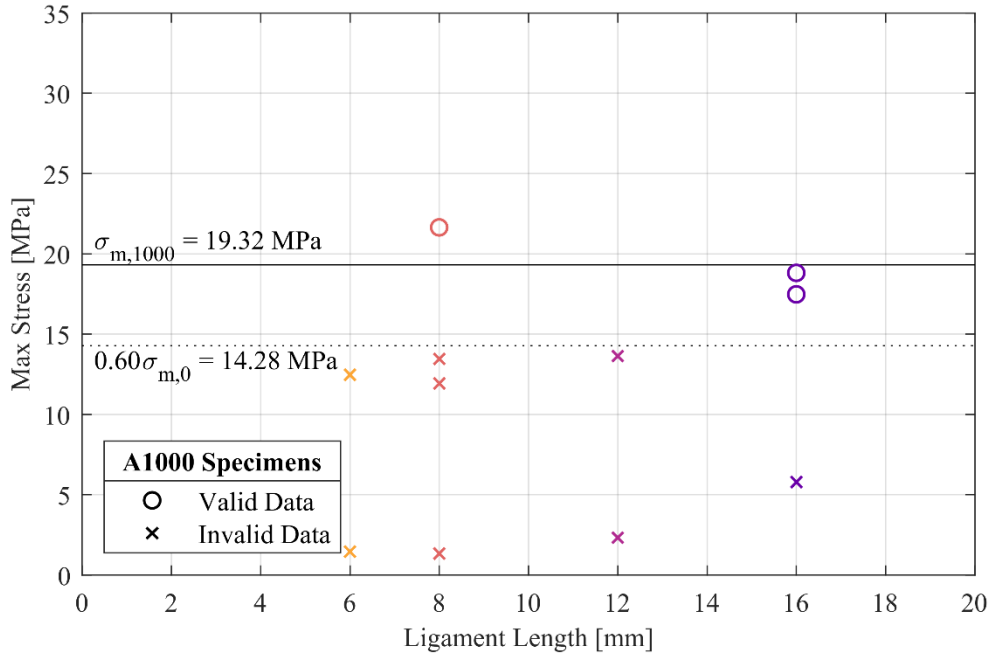

Figure C.11: Maximum stress versus ligament length for 1000-hour A specimens

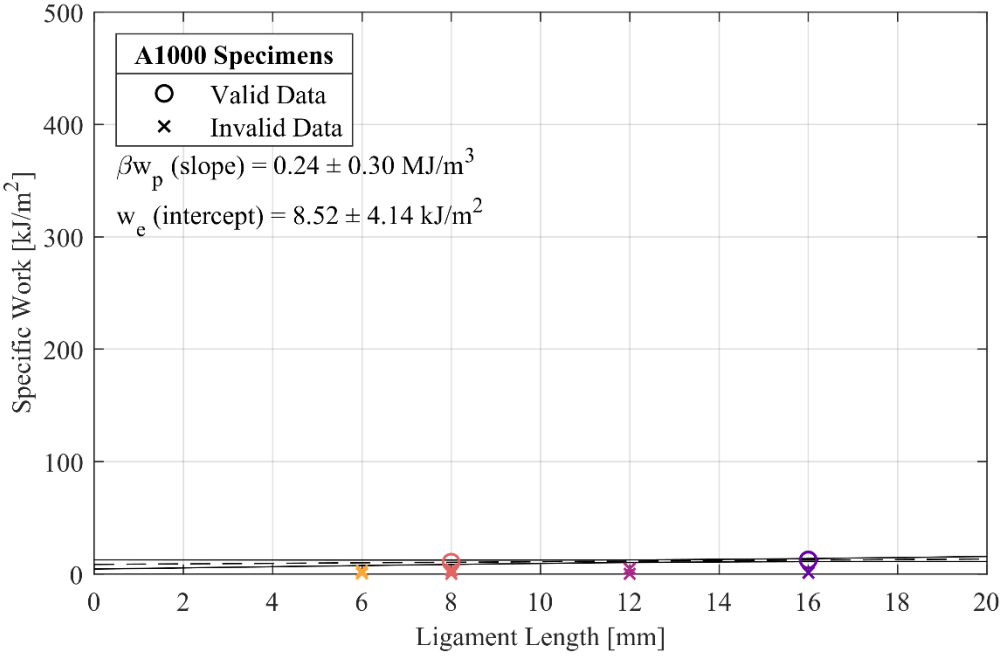

Figure C.12: Essential work of fracture regression results for 1000-hour A specimens

C.1.5 1250-hour A Specimens

Figure C.13 shows load-displacement plots for each 1250-hour A specimen. A second axis is also provided to allow comparison between exposure levels. Table C.8 lists EWF data for all 1250-hour A specimens.

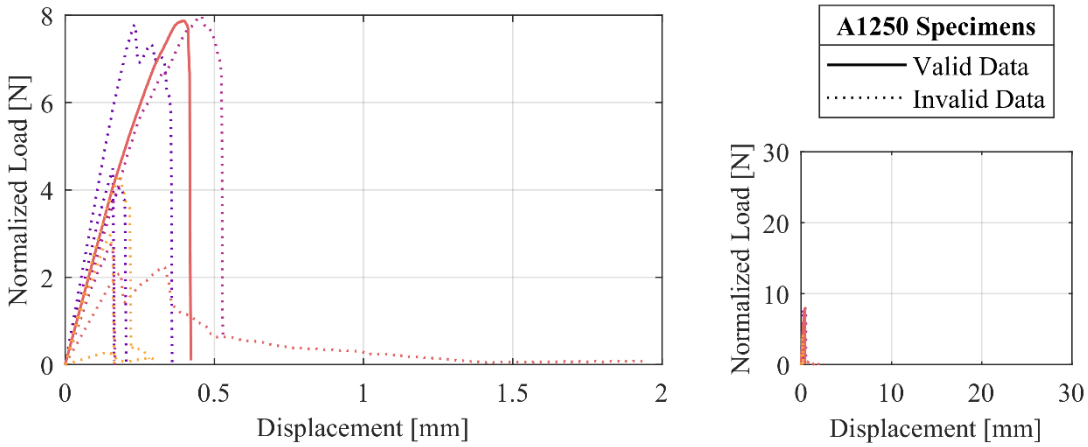

Figure C.13: Load-displacement curves for 1250-hour A specimens

Table C.8: Essential work of fracture data for 1250-hour A specimens

Thick-ness [mm]	Ligament Length [mm]	Peak Load [N]	Max Stress [MPa]	Failure Energy [mJ]	Specific Work [kJ/m²]	Invalid Data
0.062	6	4.4	11.74	0.6	1.58	stress
0.066	6	0.3	0.74	0.0	0.11	stress
0.071	6	3.4	7.99	0.3	0.73	stress
0.067	8	8.6	15.92	2.2	4.03	
0.084	8	3.0	4.54	1.4	2.02	stress
0.075	12	9.7	10.76	3.3	3.60	stress
0.061	12	2.7	3.71	0.3	0.35	stress
0.086	16	10.9	7.87	2.6	1.86	stress
0.052	16	3.8	4.55	0.3	0.39	stress
0.059	16	3.9	4.11	0.5	0.48	stress

Figure C.14 shows the EWF stress cutoff and maximum stress values for each specimen. Specific work values are shown with final regression results in Figure C.15.

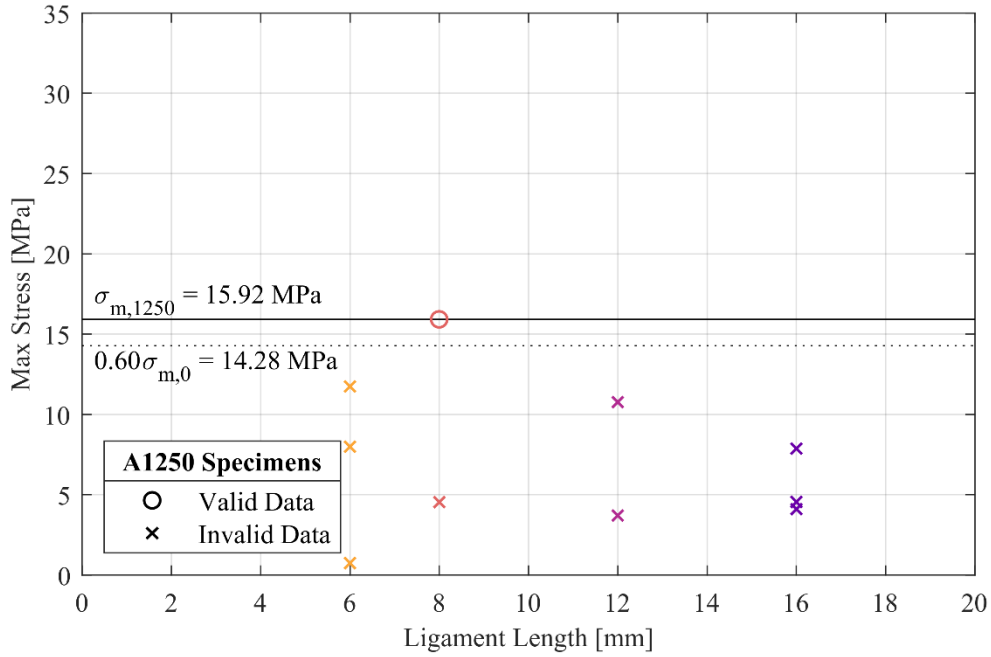

Figure C.14: Maximum stress versus ligament length for 1250-hour A specimens

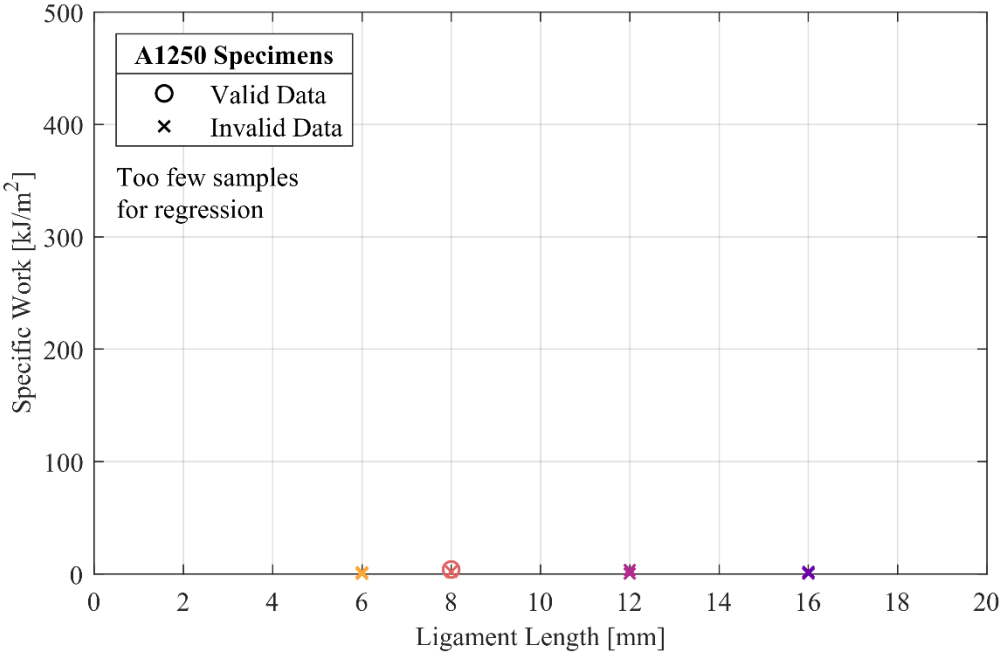

Figure C.15: Essential work of fracture regression results for 1250-hour A specimens

C.2 Results for B Specimens

Table C.9 lists testing conditions for tensile tests used to derive the theoretical DENT maximum stress ($1.15\sigma_y$) and stress values for the stress criteria applied in this study. The resulting $1.15\sigma_y$ value is provided as a reference only and is plotted only for the unexposed samples in Figure C.17. DENT specimen data were considered invalid for EWF analysis if test maximum stress values were below 60% of the maximum stress from unexposed specimens. This cutoff value ($0.60\sigma_{m,0}$) is plotted for each exposure level in the corresponding maximum stress versus ligament length figure.

Table C.9: Tensile test conditions and EWF stress criterion for B specimens

Tensile specimen geometry	ASTM D1708
Mean D1708 specimen thickness	0.065 mm
Tensile test speed	12.5 mm/min
Mean tensile yield stress, σ_y	28.3 MPa
Theoretical DENT max stress ($1.15\sigma_y$)	32.5 MPa
Mean max stress (unexposed), $\sigma_{m,0}$	28.3 MPa
Max stress cutoff ($0.60\sigma_{m,0}$)	17.0 MPa

Table C.10 summarizes regression results for each exposure level. Slope (βw_p) and intercept (w_e) values are included, as well as 95% confidence intervals and R^2 values. Resulting regression lines and confidence intervals are plotted for each exposure level in the corresponding specific work versus ligament length figures.

Table C.10: Essential work results for B specimens, by exposure time

Exposure [hr]	**0**	**500**	**750**	**1000**	**1250**
Valid EWF specimens	12	12	5	3	0
Mean max stress, σ_m [MPa]	28.3	29.4	30.8	18.2	N/A
Essential work of fracture, w_e [kJ/m²]	42.3	53.5	34.0	-3.16	*
w_e ± 95% confidence interval	± 50.1	± 91.2	± 433	± 4.22	*
Plastic work factor, βw_p [MJ/m³]	24.5	18.1	3.76	1.08	*
βw_p ± 95% confidence interval	± 4.49	± 8.16	± 59.6	± 0.39	*
Regression R^2	0.94	0.71	0.01	1.00	*

*Denotes too few specimens to perform regression

C.2.1 Unexposed B Specimens

Figure C.16 shows load-displacement plots for each unexposed B specimen. A second axis is also provided to allow comparison between exposure levels. Table C.11 lists EWF data for all unexposed B specimens.

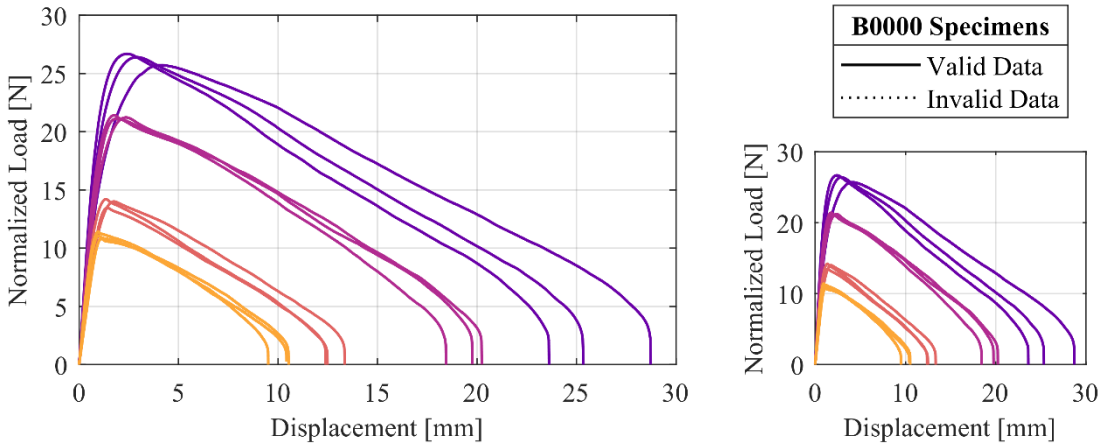

Figure C.16: Load-displacement curves for unexposed B specimens

Table C.11: Essential work of fracture data for unexposed B specimens

Thick-ness [mm]	Ligament Length [mm]	Peak Load [N]	Max Stress [MPa]	Failure Energy [mJ]	Specific Work [kJ/m²]	Invalid Data
0.056	6	9.8	29.24	67.6	201.09	
0.060	6	11.0	30.79	68.4	190.93	
0.060	6	10.8	29.88	71.3	197.18	
0.069	8	15.9	28.75	119.9	216.41	
0.061	8	13.9	28.35	116.5	237.85	
0.068	8	14.7	27.26	112.1	207.59	
0.065	12	22.5	28.89	260.5	335.22	
0.058	12	19.8	28.65	246.5	357.20	
0.056	12	19.1	28.51	243.7	364.30	
0.058	16	24.0	26.02	440.5	476.70	
0.067	16	28.8	26.73	450.7	418.88	
0.061	16	26.4	27.01	377.2	386.44	

Figure C.17 shows the EWF stress cutoff and maximum stress values for each specimen. Specific work values are shown with final regression results in Figure C.18.

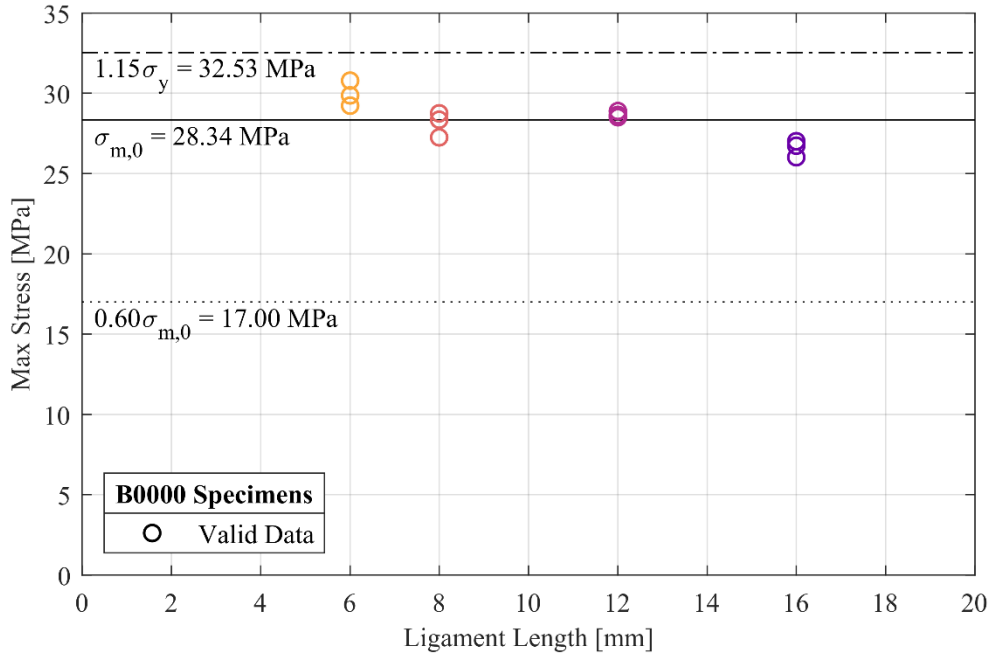

Figure C.17: Maximum stress versus ligament length for unexposed B specimens

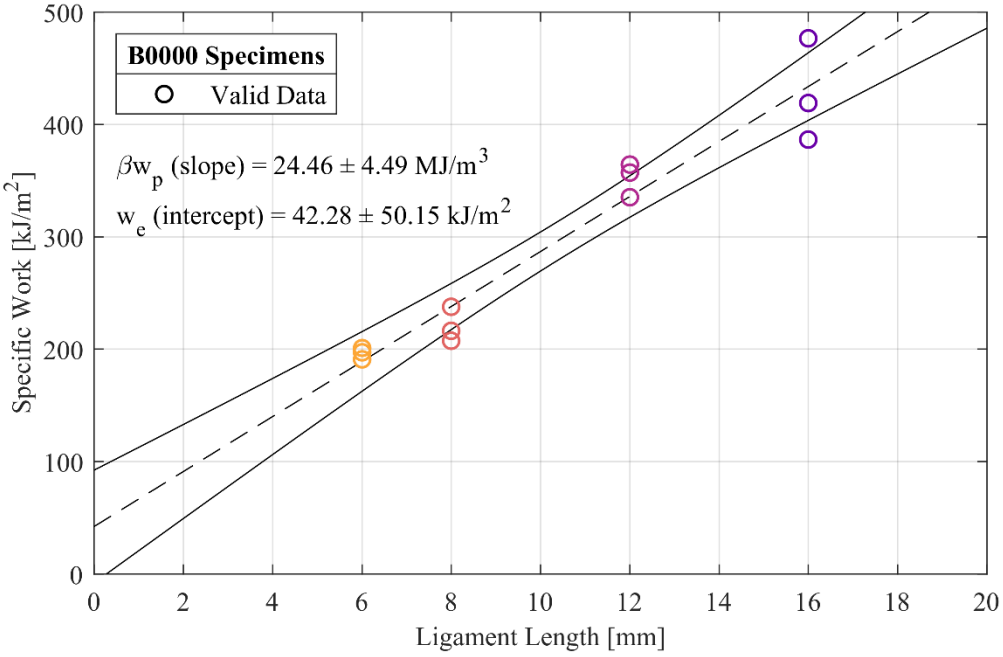

Figure C.18: Essential work of fracture regression results for unexposed B specimens

C.2.2 500-hour B Specimens

Figure C.19 shows load-displacement plots for each 500-hour B specimen. A second axis is also provided to allow comparison between exposure levels. Table C.12 lists EWF data for all 500-hour B specimens.

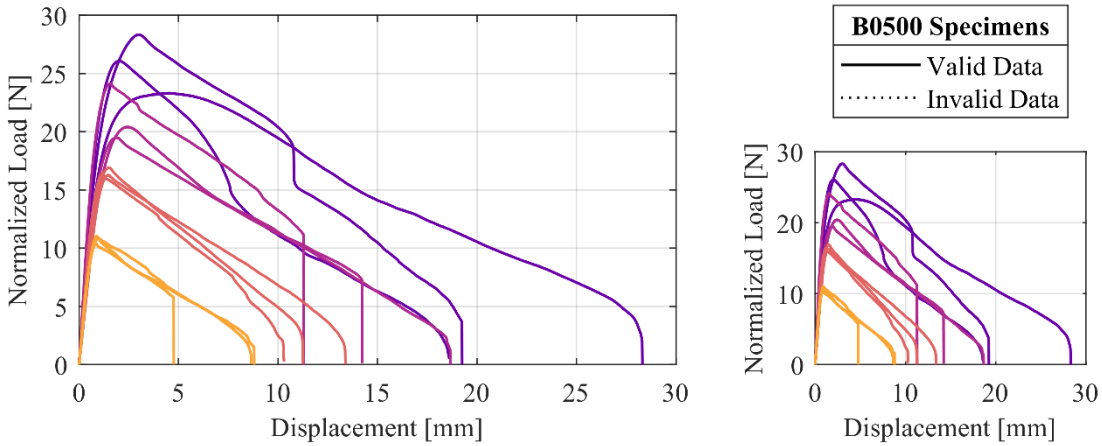

Figure C.19: Load-displacement curves for 500-hour B specimens

Table C.12: Essential work of fracture data for 500-hour B specimens

Thick-ness [mm]	Ligament Length [mm]	Peak Load [N]	Max Stress [MPa]	Failure Energy [mJ]	Specific Work [kJ/m²]	Invalid Data
0.065	6	11.4	29.28	57.4	147.23	
0.046	6	7.7	28.13	27.5	100.81	
0.062	6	11.0	29.77	57.3	154.55	
0.077	8	20.6	33.28	128.7	208.19	
0.073	8	19.2	32.94	151.8	260.79	
0.085	8	23.3	34.25	156.3	229.91	
0.057	12	18.8	27.54	195.5	285.80	
0.063	12	20.0	26.30	193.5	254.95	
0.059	12	23.1	32.55	191.8	269.75	
0.056	16	21.1	23.59	375.3	418.85	
0.060	16	25.1	26.39	239.1	251.13	
0.082	16	37.7	28.66	444.4	337.66	

Figure C.20 shows the EWF stress cutoff and maximum stress values for each specimen. Specific work values are shown with final regression results in Figure C.21.

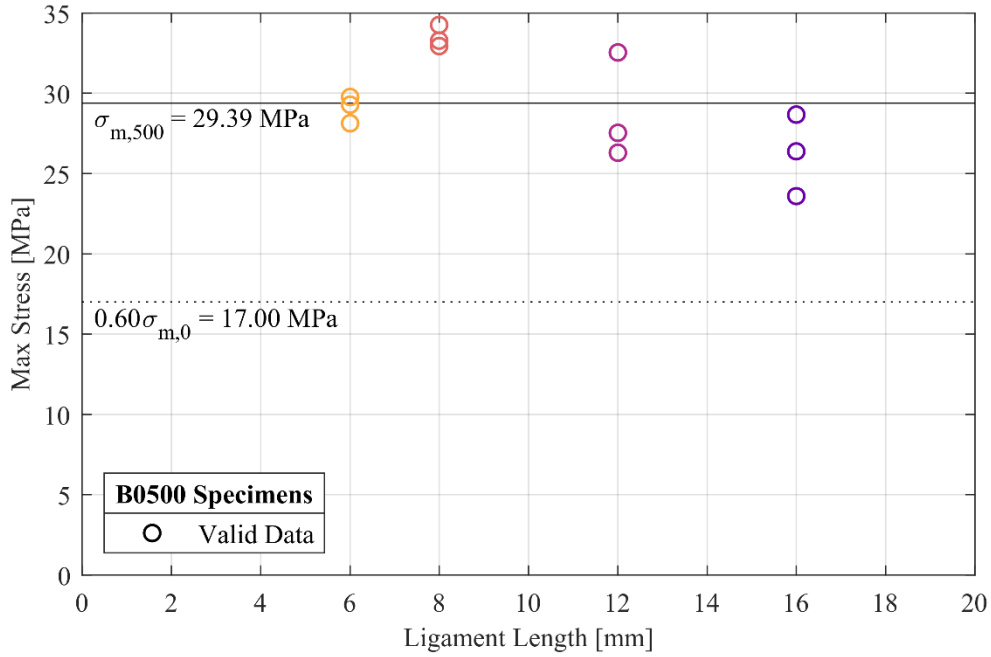

Figure C.20: Maximum stress versus ligament length for 500-hour B specimens

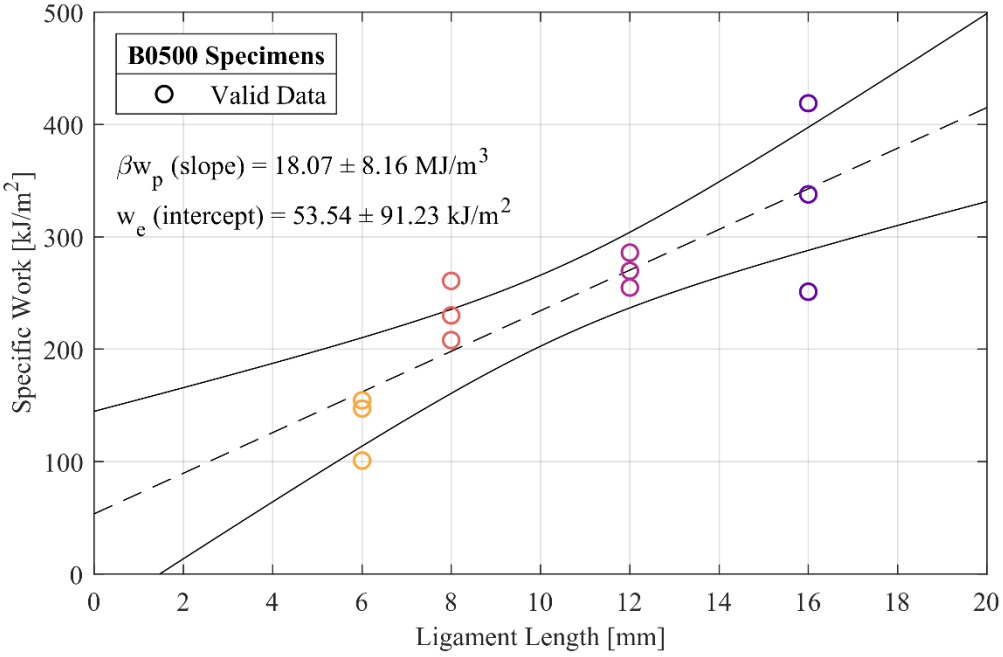

Figure C.21: Essential work of fracture regression results for 500-hour B specimens

C.2.3 750-hour B Specimens

Figure C.22 shows load-displacement plots for each 750-hour B specimen. A second axis is also provided to allow comparison between exposure levels. Table C.13 lists EWF data for all 750-hour B specimens.

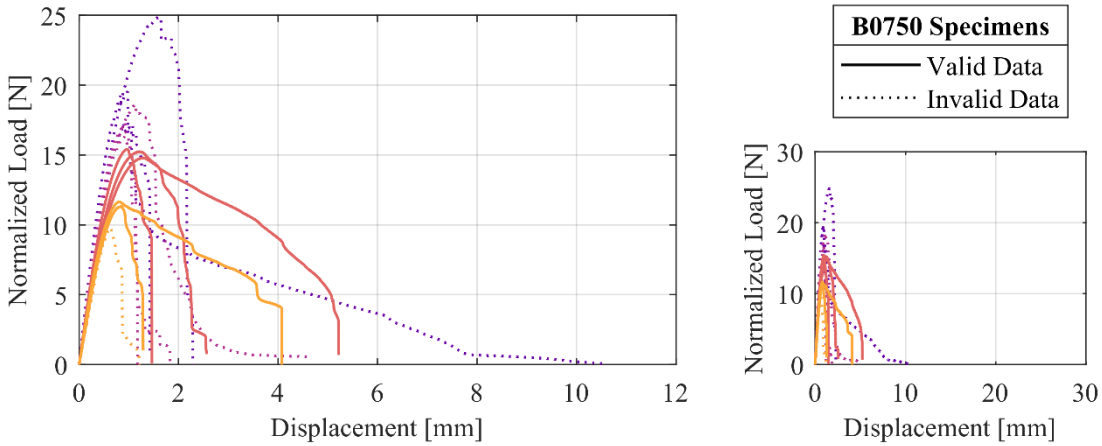

Figure C.22: Load-displacement curves for 750-hour B specimens

Table C.13: Essential work of fracture data for 750-hour B specimens

Thick-ness [mm]	Ligament Length [mm]	Peak Load [N]	Max Stress [MPa]	Failure Energy [mJ]	Specific Work [kJ/m²]	Invalid Data
0.062	6	11.3	30.53	9.7	26.30	
0.058	6	10.9	31.43	30.1	86.94	
0.060	6	9.5	26.44	5.8	16.13	yield
0.065	8	16.2	31.21	16.3	31.42	
0.064	8	15.4	29.94	55.9	108.79	
0.075	8	18.4	30.84	31.1	52.24	
0.065	12	19.7	25.11	29.6	37.85	yield
0.061	12	16.0	22.00	13.8	18.87	yield
0.065	12	18.0	23.30	14.0	18.14	yield
0.056	16	15.6	17.48	15.4	17.29	yield
0.064	16	25.7	25.14	39.7	38.82	yield
0.065	16	20.5	19.76	53.9	52.00	yield

Figure C.23 shows the EWF stress cutoff and maximum stress values for each specimen. Specific work values are shown with final regression results in Figure C.24.

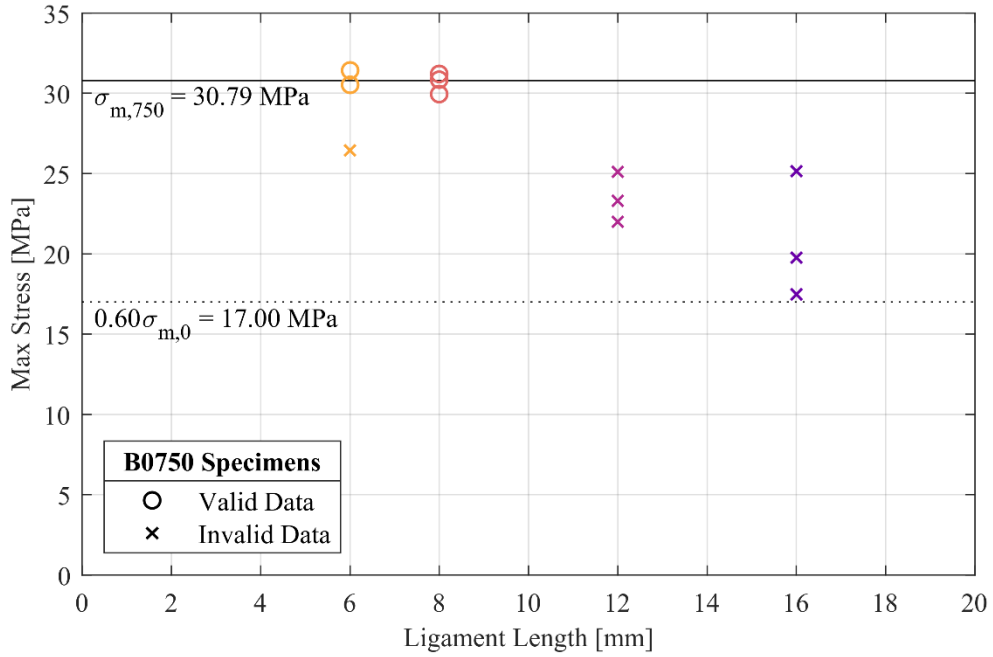

Figure C.23: Maximum stress versus ligament length for 750-hour B specimens

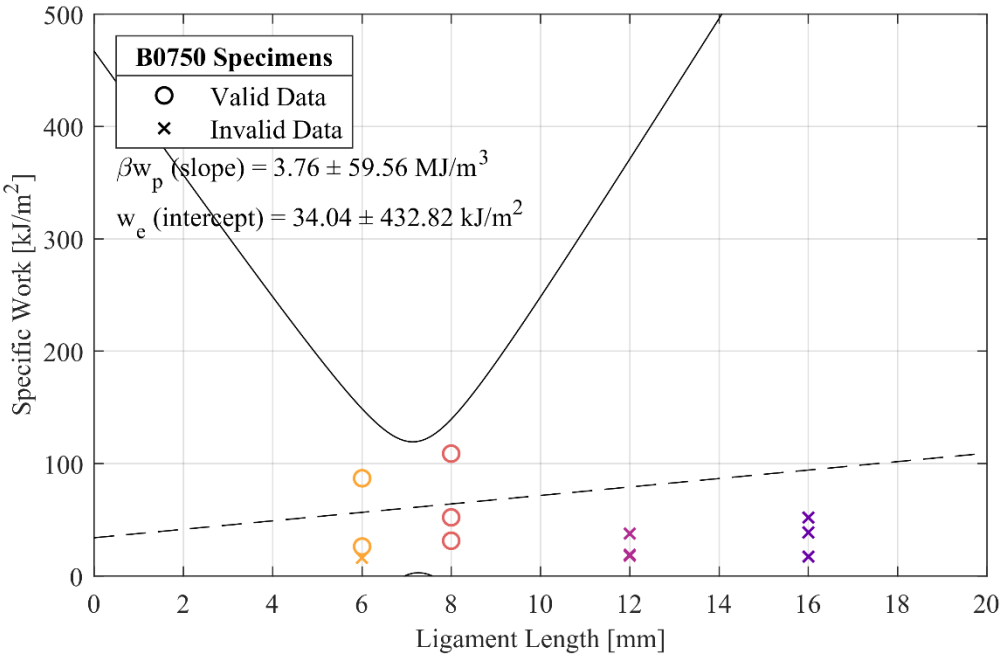

Figure C.24: Essential work of fracture regression results for 750-hour B specimens

C.2.4 1000-hour B Specimens

Figure C.25 shows load-displacement plots for each 1000-hour B specimen. A second axis is also provided to allow comparison between exposure levels. Table C.14 lists EWF data for all 1000-hour B specimens.

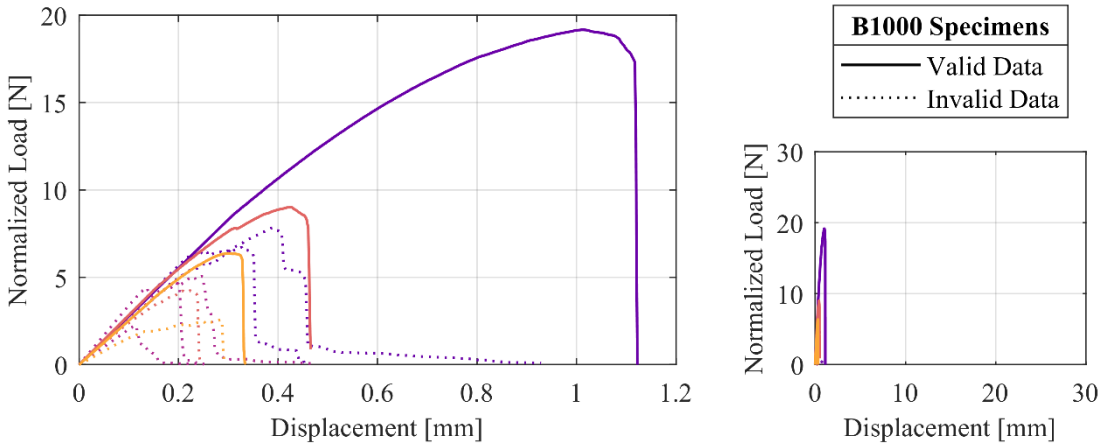

Figure C.25: Load-displacement curves for 1000-hour B specimens

Table C.14: Essential work of fracture data for 1000-hour B specimens

Thick-ness [mm]	Ligament Length [mm]	Peak Load [N]	Max Stress [MPa]	Failure Energy [mJ]	Specific Work [kJ/m²]	Invalid Data
0.059	6	6.1	17.18	1.2	3.44	
0.062	6	2.6	6.94	0.5	1.30	stress
0.059	8	4.0	8.57	0.6	1.25	stress
0.069	8	10.0	18.23	2.9	5.27	
0.052	12	3.9	6.29	0.5	0.72	stress
0.058	12	4.8	6.82	0.9	1.28	stress
0.053	12	1.9	3.04	0.2	0.25	stress
0.087	16	27.0	19.40	19.6	14.09	
0.064	16	8.1	7.93	2.4	2.38	stress
0.078	16	8.5	6.80	2.1	1.66	stress

Figure C.26 shows the EWF stress cutoff and maximum stress values for each specimen. Specific work values are shown with final regression results in Figure C.27.

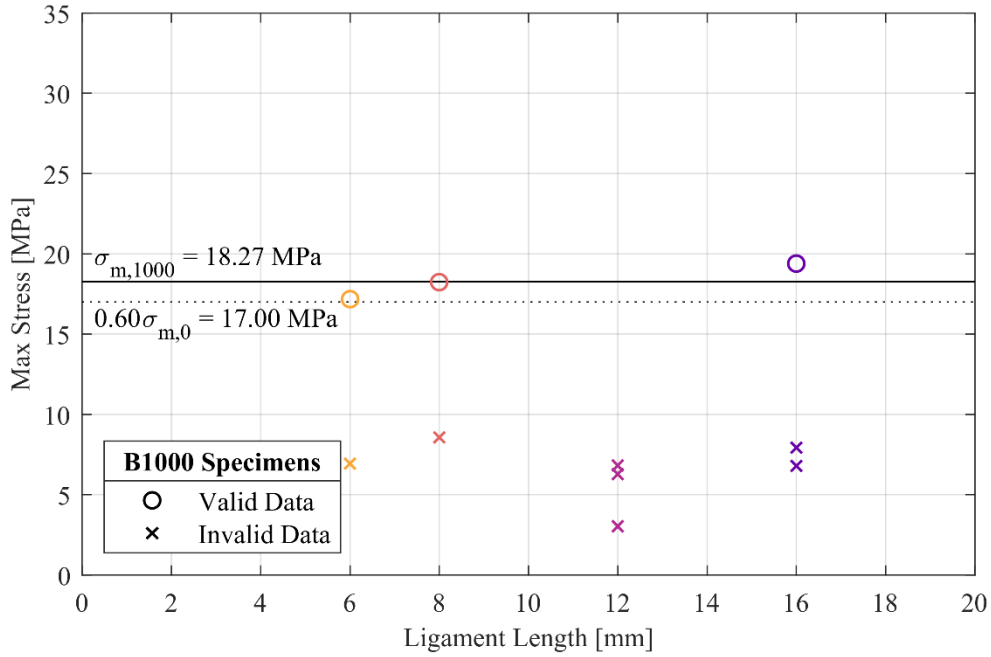

Figure C.26: Maximum stress versus ligament length for 1000-hour B specimens

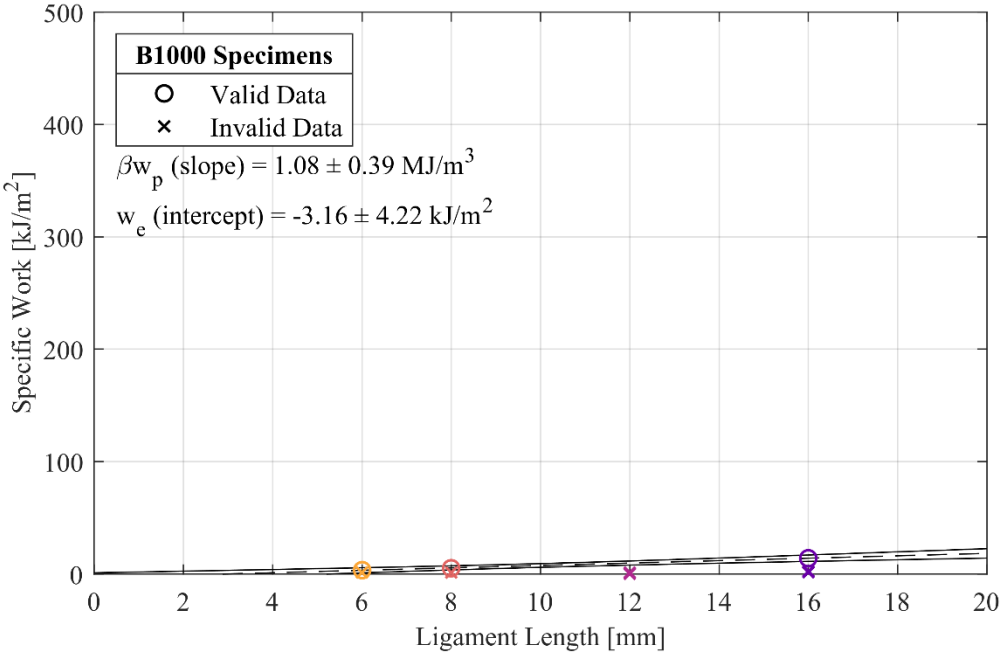

Figure C.27: Essential work of fracture regression results for 1000-hour B specimens

C.2.5 1250-hour B Specimens

Figure C.28 shows load-displacement plots for each 1250-hour B specimen. A second axis is also provided to allow comparison between exposure levels. Table C.15 lists EWF data for all 1250-hour B specimens.

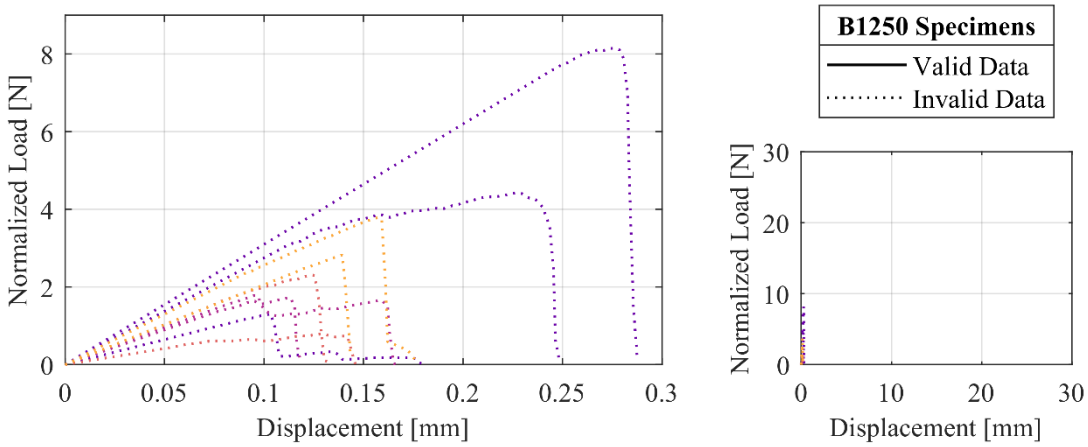

Figure C.28: Load-displacement curves for 1250-hour B specimens

Table C.15: Essential work of fracture data for 1250-hour B specimens

Thick-ness [mm]	Ligament Length [mm]	Peak Load [N]	Max Stress [MPa]	Failure Energy [mJ]	Specific Work [kJ/m²]	Invalid Data
0.060	6	2.7	7.63	0.2	0.56	stress
0.059	6	3.6	10.21	0.3	0.90	stress
0.056	8	0.7	1.60	0.1	0.14	stress
0.058	8	2.2	4.67	0.2	0.33	stress
0.057	12	1.6	2.32	0.1	0.16	stress
0.068	12	2.0	2.40	0.2	0.25	stress
0.053	16	1.1	1.33	0.1	0.09	stress
0.067	16	8.8	8.25	1.3	1.26	stress
0.083	16	5.9	4.48	0.9	0.70	stress

Figure C.29 shows the EWF stress cutoff and maximum stress values for each specimen. Specific work values are shown with final regression results in Figure C.30.

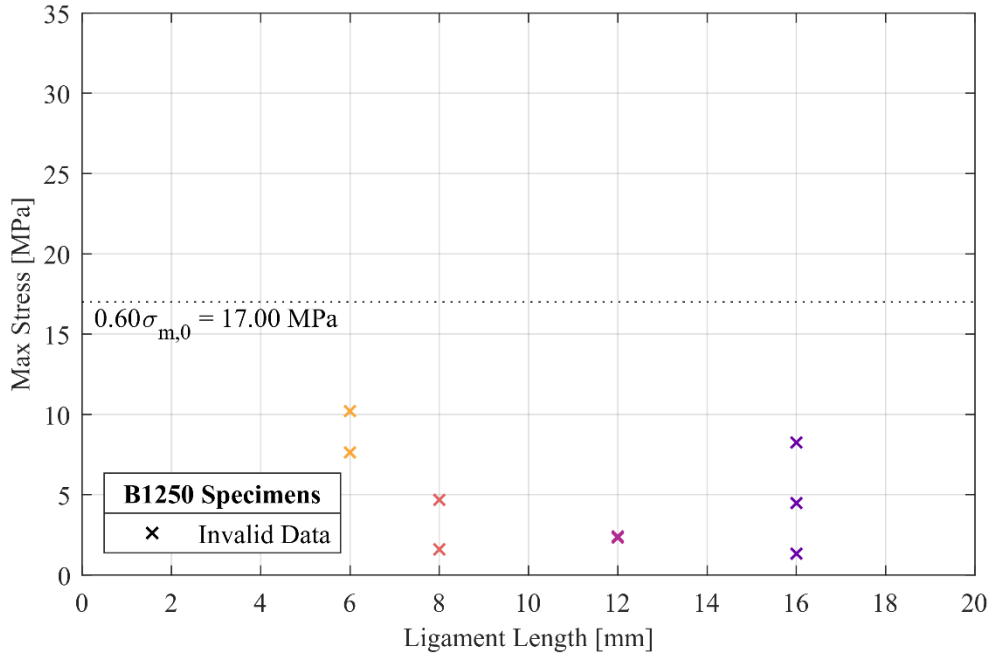

Figure C.29: Maximum stress versus ligament length for 1250-hour B specimens

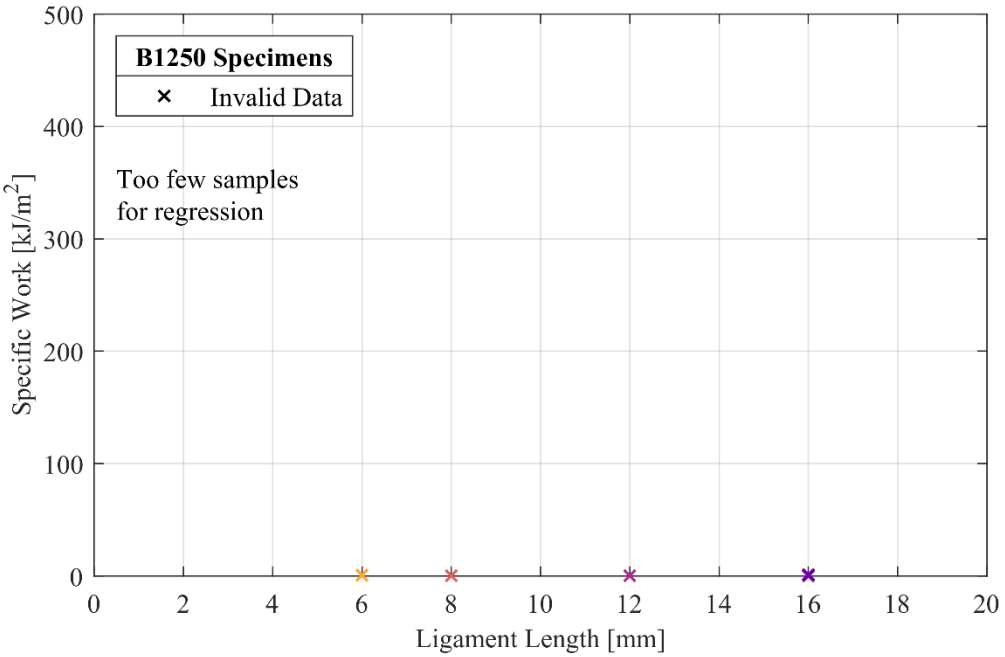

Figure C.30: Essential work of fracture regression results for 1250-hour B specimens

C.3 Essential work of fracture surface regression comparison

Surface regressions were calculated from the same DENT data and validity criteria (yielding and maximum stress) as the standard EWF method described in previous sections of this appendix. Figure 5.19 demonstrates the resulting surface, with parameters listed in Table 5.3. In the following sections, plots compare the outcomes of the surface fit for exposure time to those from the standard EWF method. Each plot represents a cross-section of the surface fit taken at a constant exposure time along with the associated 95% confidence intervals. Two plots are presented in each section, representing results from A specimen and B specimen data.

C.3.1 Unexposed Results

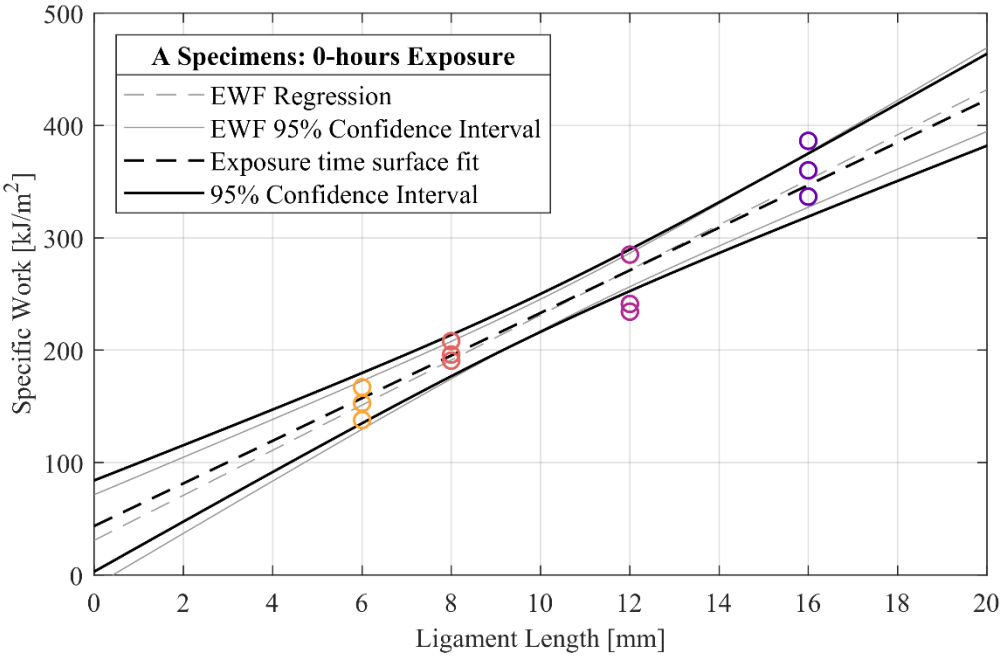

Figure C.31: Exposure time surface regression comparison for unexposed A specimens

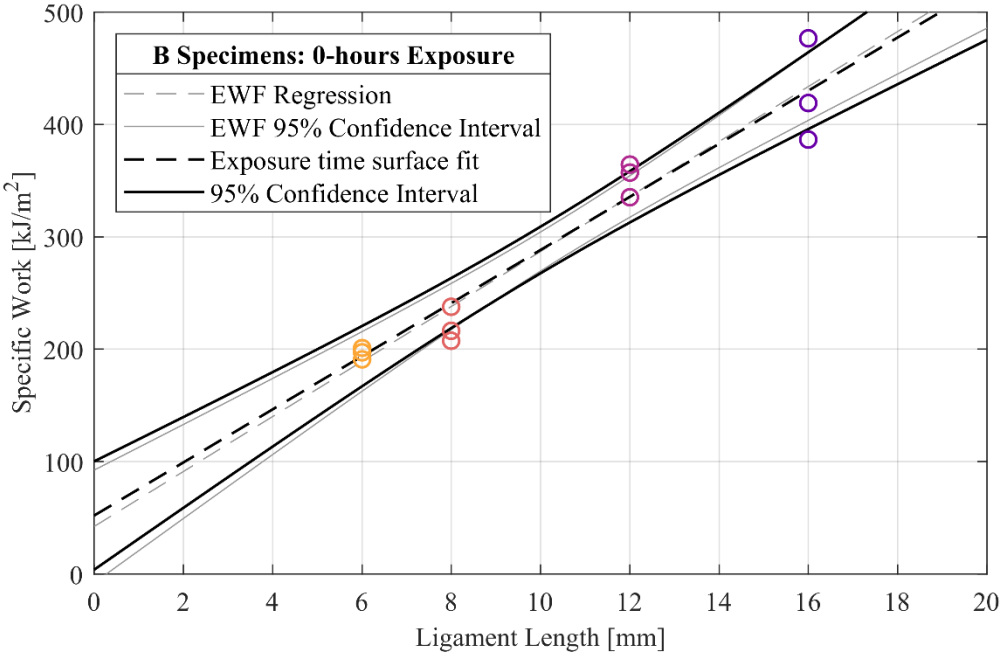

Figure C.32: Exposure time surface regression comparison for unexposed B specimens

C.3.2 250-hour Results

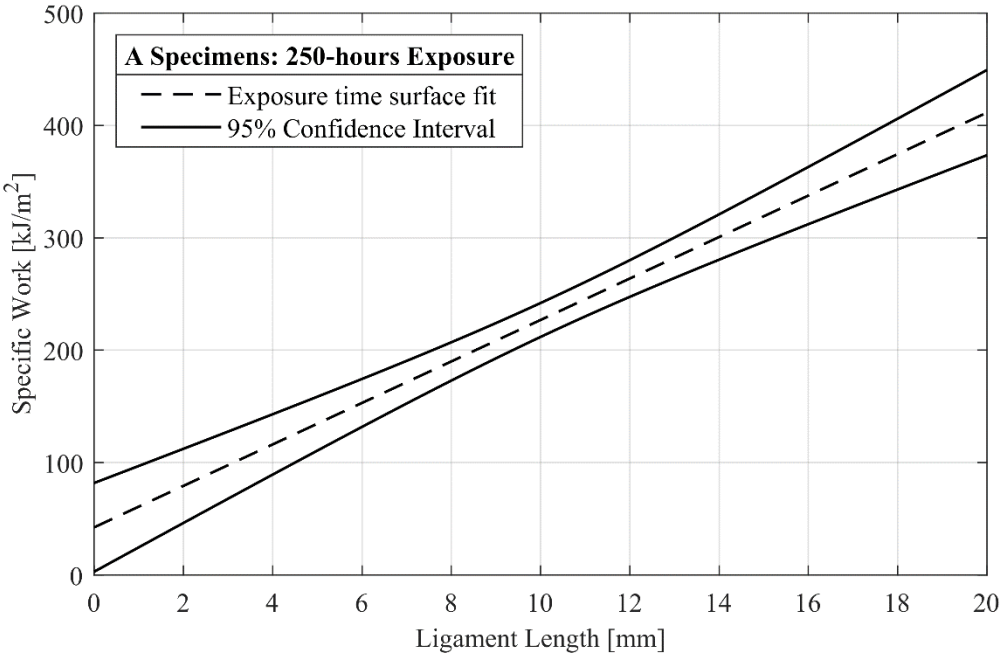

Figure C.33: Exposure time surface regression comparison for 250-hour A specimens

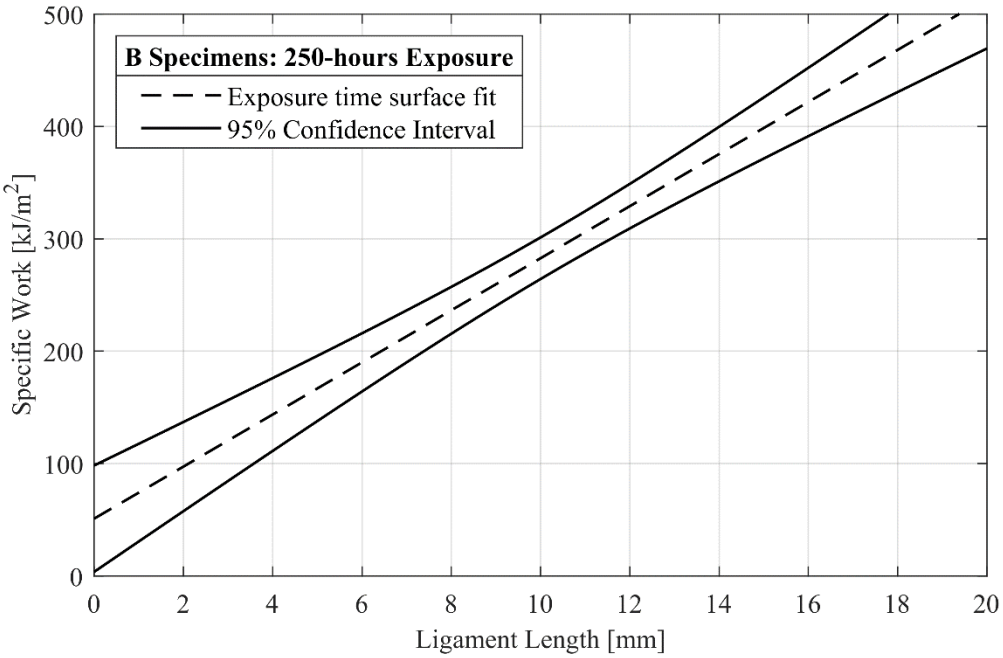

Figure C.34: Exposure time surface regression comparison for 250-hour B specimens

C.3.3 500-hour Results

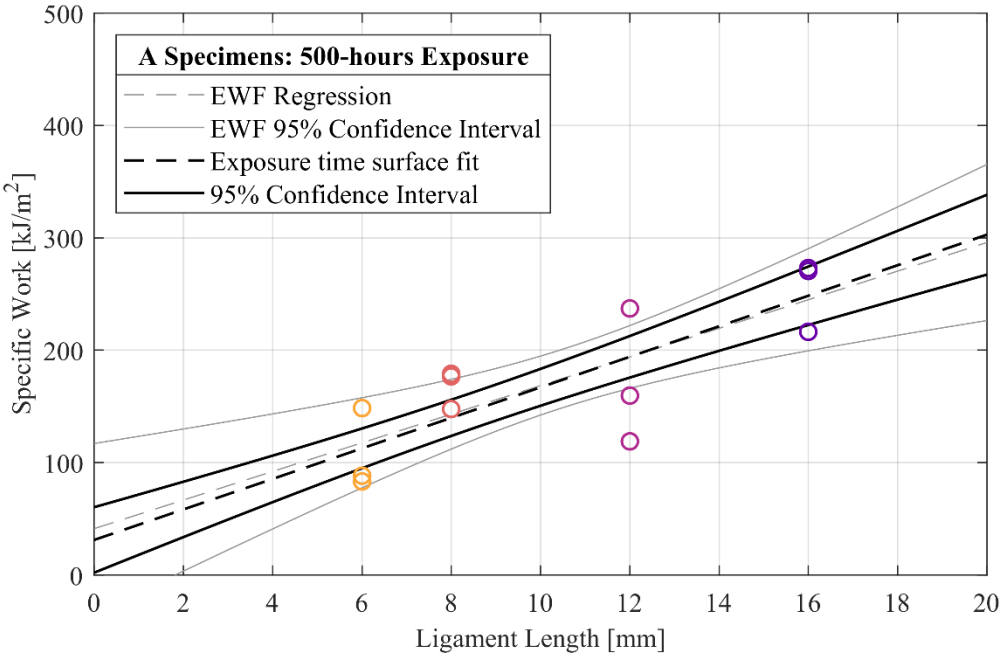

Figure C.35: Exposure time surface regression comparison for 500-hour A specimens

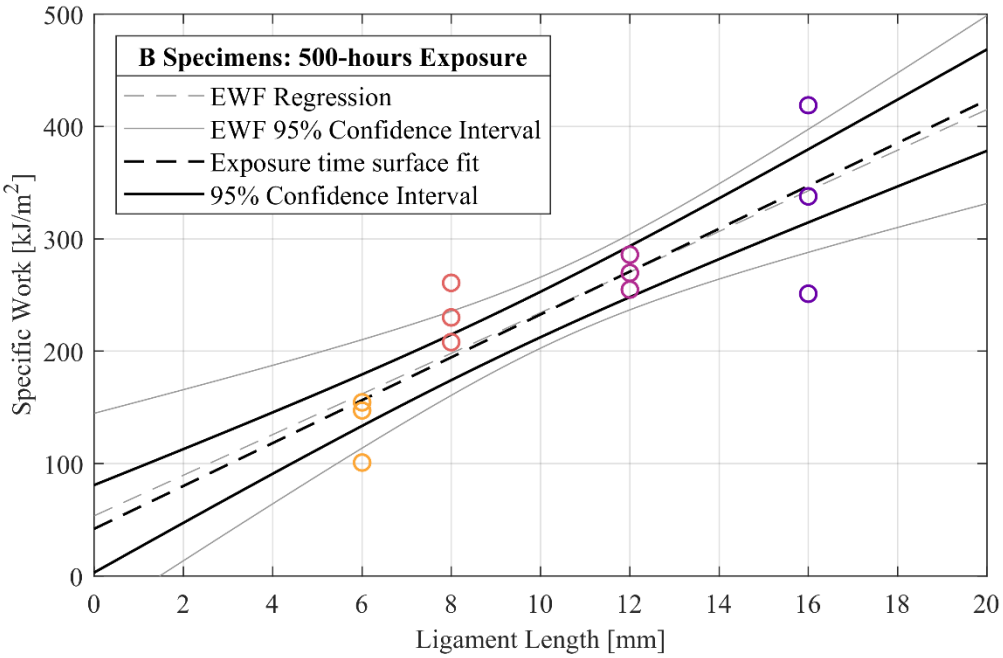

Figure C.36: Exposure time surface regression comparison for 500-hour B specimens

C.3.4 750-hour Results

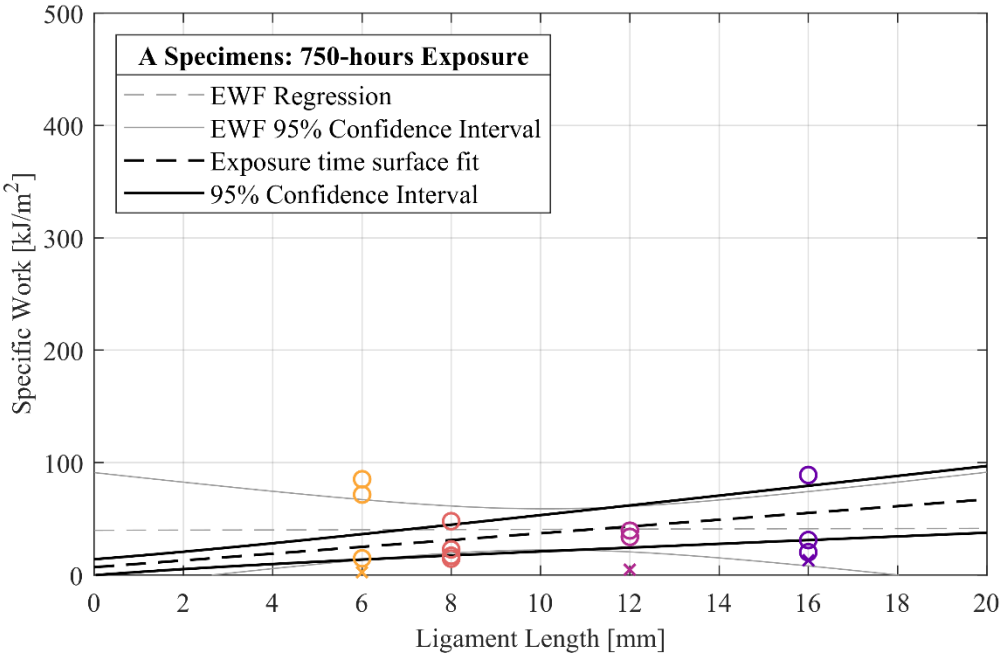

Figure C.37: Exposure time surface regression comparison for 750-hour A specimens

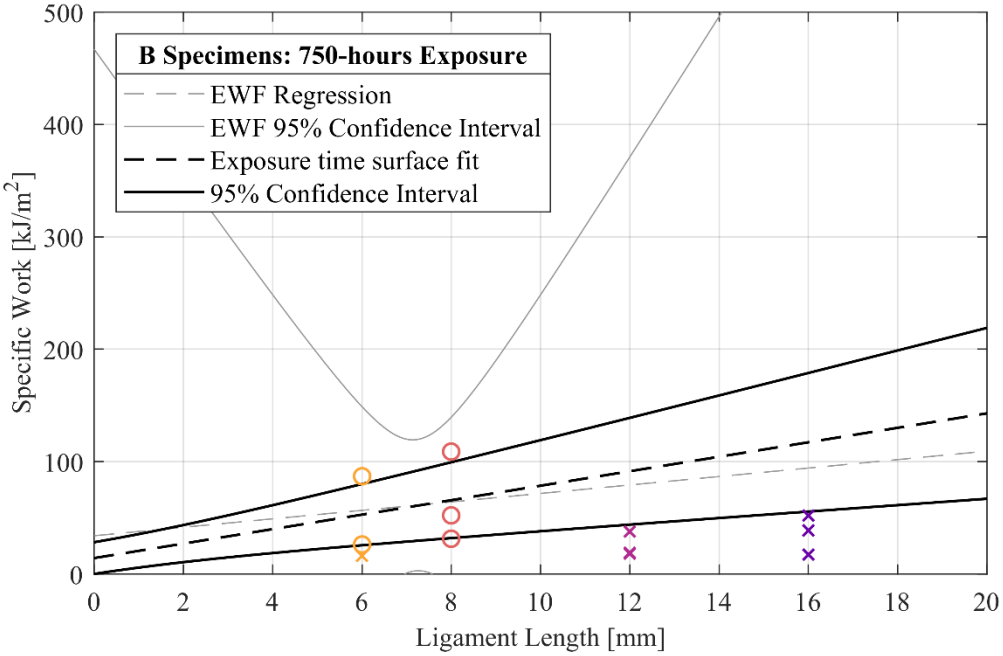

Figure C.38: Exposure time surface regression comparison for 750-hour B specimens

C.3.5 1000-hour Results

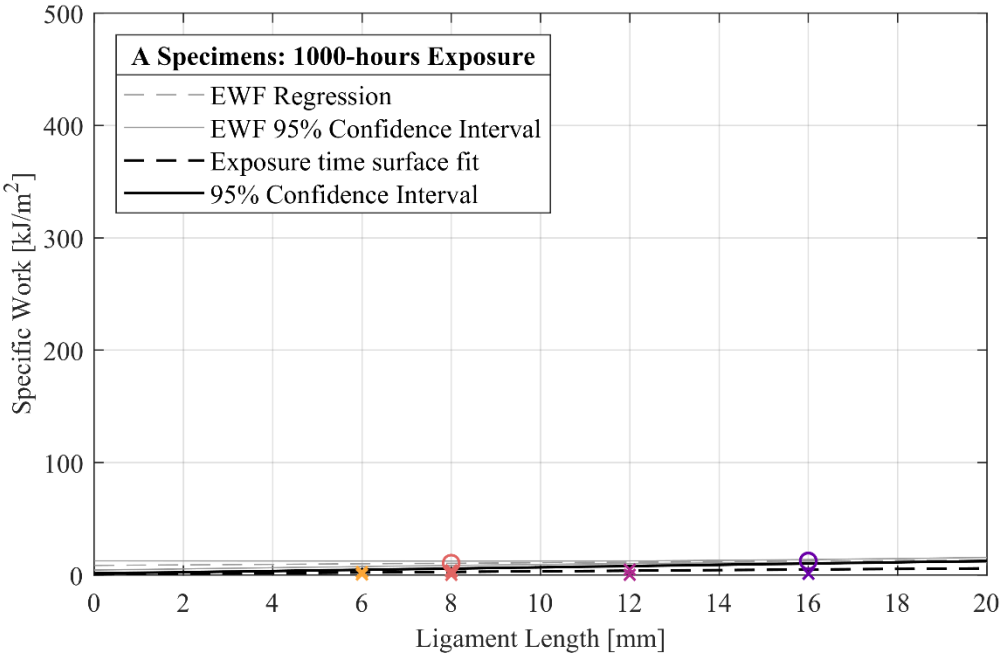

Figure C.39: Exposure time surface regression comparison for 1000-hour A specimens

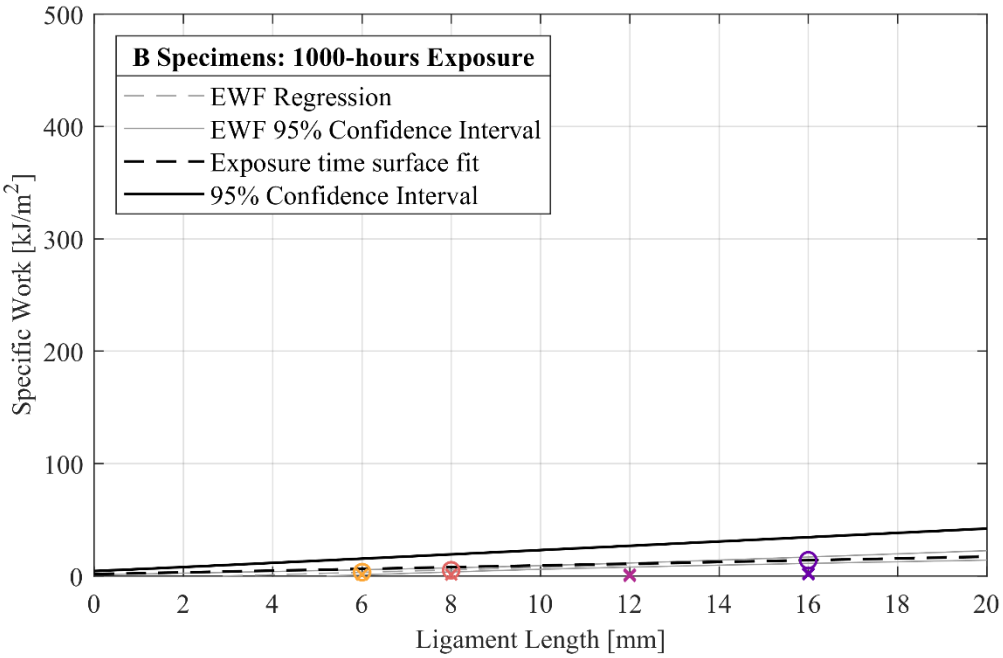

Figure C.40: Exposure time surface regression comparison for 1000-hour B specimens